University of Alberta

Bond Anchorage of Straight and Hooked Reinforcing Bars

by

Armin Erfanian

©

A thesis submitted to the Faculty of Graduate Studies and Research
in partial fulfillment of the requirements for the degree of

Doctor of Philosophy

in

Structural Engineering

Department of Civil and Environmental Engineering

Edmonton, Alberta
Fall 2007

Library and Archives Canada

Published Heritage Branch

395 Wellington Street
Ottawa ON K1A 0N4
Canada

Bibliothèque et Archives Canada

Direction du Patrimoine de l'édition

395, rue Wellington
Ottawa ON K1A 0N4
Canada

Your file Votre référence
ISBN: 978-0-494-32952-8
Our file Notre référence
ISBN: 978-0-494-32952-8

NOTICE:
The author has granted a non-exclusive license allowing Library and Archives Canada to reproduce, publish, archive, preserve, conserve, communicate to the public by telecommunication or on the Internet, loan, distribute and sell theses worldwide, for commercial or non-commercial purposes, in microform, paper, electronic and/or any other formats.

The author retains copyright ownership and moral rights in this thesis. Neither the thesis nor substantial extracts from it may be printed or otherwise reproduced without the author's permission.

AVIS:
L'auteur a accordé une licence non exclusive permettant à la Bibliothèque et Archives Canada de reproduire, publier, archiver, sauvegarder, conserver, transmettre au public par télécommunication ou par l'Internet, prêter, distribuer et vendre des thèses partout dans le monde, à des fins commerciales ou autres, sur support microforme, papier, électronique et/ou autres formats.

L'auteur conserve la propriété du droit d'auteur et des droits moraux qui protège cette thèse. Ni la thèse ni des extraits substantiels de celle-ci ne doivent être imprimés ou autrement reproduits sans son autorisation.

In compliance with the Canadian Privacy Act some supporting forms may have been removed from this thesis.

While these forms may be included in the document page count, their removal does not represent any loss of content from the thesis.

Conformément à la loi canadienne sur la protection de la vie privée, quelques formulaires secondaires ont été enlevés de cette thèse.

Bien que ces formulaires aient inclus dans la pagination, il n'y aura aucun contenu manquant.

Canada

To My Family

Abstract

This work focuses on the bond behavior of large diameter bars with hooks embedded in short reinforced concrete joints. The research has three parts. First an experimental work with a reinforced concrete specimen has been conducted. In the next step a finite element analysis was carried out. In order to perform an accurate analysis a bond-slip model was proposed. To accelerate the analysis the proposed model was automated. Good agreement was found between the results from the proposed approach and the literature test results. A parametric study of a series of reinforced concrete models with hooked bars was carried out and the results were used for a comparison with CSA-A23.3 code provisions for hook development. Recommendations for improvement in design have been presented. Finally, conclusions and suggestions for future research have been presented.

As for experimental work a reinforced concrete joint under closing moments was tested. Load was applied using MTS-6000 machine with displacement control type of loading.

Finite element analysis was carried out using explicit quasi static analysis with three dimensional elements for concrete and steel. A bond-slip model was developed to define the interaction at the steel-concrete interface.The proposed bond model accounts for strength of concrete, bar diameter, concrete cover and level of confinement. Verification is done using previous researchers' test results

and finite element analyses. The proposed model renders results close to the ones in literature.

A series of reinforced concrete models with large bars hooked into them were studied to determine the effects of bend radius and tail length. Comparison with CSA-A23.3 provisions shows whether or not they are conservative.

Acknowledgement

This project was funded by the Natural Sciences and Engineering Research Council of Canada and by the Canadian Cement Association.

The author wishes to express appreciation to Professor A. E. Elwi for continued supervision and guidance throughout the project. Dr. Scott Alexander helped establish the initial direction of the project and provided advice and valuable comments.

Table of Contents

Chapter 1. Introduction.....1

1.1. Scope.....1
1.2. Objectives.....2
1.3. Methodology.....2
1.4. Outline of the Thesis.....3

Chapter 2. Literature Review.....8

2.1. Introduction.....8
2.2. Experimental Work by Past Researchers.....9
2.3. Analytical Work by Past Researchers.....11

Chapter 3. Experimental Work.....19

3.1. Introduction.....19
3.2. Specimen Design.....19
3.3. Test Setup.....20
3.3.1. Specimen Details and Instrumentation.....21
3.3.2. Results.....21

Chapter 4. Analysis and Bond Model Development.....34

4.1. Introduction.....34
4.2. Finite Element Mesh.....36
4.3. Analysis Procedure.....38
4.4. Modeling of Material Properties.....40
4.5. Modeling of Bond.....43
4.5.1. Unconfined Ultimate Bond Capacity.....43
4.5.2. Confined Bond Capacity.....44
4.5.3. Discussion to Summarize the Rationale of the Research.....47
4.5.4. Development/Test of the Model.....47
4.6. Comparison with Test.....50

Chapter 5. Interface Constitutive Model 66

5.1. Introduction.....66
5.2. Total Form of the Bond Stress-Slip Response.....66
5.3. Incremental Form of Automatic Procedure.....69
5.4. Algorithm and Flowchart Diagram.....70

Chapter 6. Verification of Constitutive Model.....75

6.1. Introduction.....75
6.2. Properties of the Models.....75

6.2.1. Untrauer et al. (1968).....75
6.2.2. Lormanometee (1974).....75
6.2.3. Minor et al.(1975).....76
6.2.4. Eligehausen et al. (1983).....76
6.3. Finite Element Mesh.....77
6.3.1. Untrauer et al. (1968) and Lormanometee (1974).....77
6.3.2. Eligehausen (1983).....78
6.3.3. Minor et al. (1975).....79
6.4. Material Properties.....79
6.5. Analysis Procedure and Results.....80
6.6. Conclusion.....81

Chapter 7. Parametric Study of the Anchorage of Hooked Bars.....105

7.1. Introduction.....105
7.2. Description of the Models.....105
7.3. Finite Element Mesh.....107
7.4. Analysis Procedure.....108
7.5. Material Properties.....109
7.6. Analysis Results.....109
7.7. Comparison with Code and Conclusions.....113

Chapter 8. Conclusion.....175

8.1. Summary.....175
8.2. Conclusions.....179
8.3. Suggestions for Future Researchers.....180

References.....181

List of Tables

Table (2.1) – Properties of Specimens.....14
Table (6.1) – Specimens Modeled in This Chapter.....83
Table (6.2) – Summary of Straight Length Tests and FE Models.....84
Table (6.3) – Hook Pullout Models.....85
Table (7.1) – Cases to be Studied.....117
Table (7.2) – Mesh Dimensions.....118
Table (7.3) – Slip at Different Bend Locations 119
Table (7.4) – Summary of Results and Conclusions.....120

List of Figures

Figure (1.1) – Corner Beam-Column Connection with Minimum Bend Radius....4
Figure (1.2) – Corner Beam-Column Connection with a Bend Radius Larger Than Minimum.....5
Figure (1.3) – Corner Beam-Column Connection Vertical Stirrups.....6
Figure (1.4) – Corner Beam-Column Connection with Horizontal Stirrups.....7
Figure (2.1) – Tension Stiffening 14
Figure (2.2) – Typical Bond Slip Relationship.....15
Figure (2.3) – Slab with Distributed Reinforcement in 2 Directions by Link et al. (1989).....15
Figure (2.4) – Schematic Drawing for Nilson's Test Setup.....16
Figure (2.5) – Schematic Drawing for Malvar's Test Setup.....17
Figure (2.6) – Schematic Drawing for Gambarova's Test Setup.....18
Figure (2.7) – Schematic Drawing for Marques et al. Test Setup.....18
Figure (2.8) – Spring Elements by Nilson (1968).....18A
Figure (2.9) – Bond Element by Lowes et al. (2004).....18A
Figure (3.1) - Strut and Tie Model.....23
Figure (3.2) – Hook Development Length.....23
Figure (3.3) – Test Specimen.....24
Figure (3.4) – Reinforcement.....25
Figure (3.5) – LVDT's.....26
Figure (3.6) – Loading of Specimen.....26
Figure (3.7) – Load-Displacement Diagram.....27
Figure (3.8) – Failed Specimen.....27
Figure (3.9) – Strain Gauges.....28
Figure (3.10) - Strain Gauges at the Beginning of the Bend and at the Face of the Joint.....28
Figure (3.11) – Strain at the Face of the Joint for SG1.....29
Figure (3.12) – Strain at the Face of the Joint for SG8.....29
Figure (3.13) – Strain at the Face of the Joint for SG9.....30

Figure (3.14) – Strain at the Face of the Joint for SG17.....30
Figure (3.15) – Average Strain at the Face of the Joint 31
Figure (3.16) – Strain at SG2.....31
Figure (3.17) – Strain at SG7.....32
Figure (3.18) – Strain at SG5.....32
Figure (3.19) – Strain at SG12.....33
Figure (3.20) – Average Strain at the Beginning of the Bend.....33
Figure (4.1) – Three and Two Dimensional Views of the Mesh.....51
Figure (4.2) – Real Bar Cross Section and Its Equivalent.....52
Figure (4.3) - Cartesian Connector Element in Local Coordinates.....52
Figure (4.4) – Uniaxial Compression Curve.....53
Figure (4.5) – Tension Softening.....53
Figure (4.6) – Comparison of the Present Bond Capacity with the Literature.....54
Figure (4.7) – Schematic Bond-Slip Curve.....54
Figure (4.8) – Bond Slip Model for 35MPa Un-tied Concrete.....55
Figure (4.9) – Bond Slip Model for 35MPa Tied Concrete.....55
Figure (4.10) – Node Numbering.....56
Figure (4.11) – Schematic Nodal Bond-Confinement and Bond-Slip Curves.....57
Figure (4.12) – Bond vs. Confinement for Node 103.....57
Figure (4.13) – Bond vs. Confinement for Node 104.....57
Figure (4.14) – Bond vs. Confinement for Node 105.....58
Figure (4.15) – Bond vs. Confinement for Node 106.....58
Figure (4.16) – Bond vs. Confinement for Node 107.....58
Figure (4.17) – Bond vs. Confinement for Node 128.....59
Figure (4.18) – Bond vs. Confinement for Node 129.....59
Figure (4.19) – Bond vs. Confinement for Node 130.....59
Figure (4.20) – Bond vs. Confinement for Node 131.....60
Figure (4.21) – Bond vs. Confinement for Node 132.....60
Figure (4.22) – Bond vs. Confinement for Node 183.....60
Figure (4.23) – Bond vs. Confinement for Node 184.....61

Figure (4.24) – Bond vs. Confinement for Node 185.....61
Figure (4.25) – Bond vs. Confinement for Node 186.....61
Figure (4.26) – Bond-Slip Relationship for Nodes 102-108.....62
Figure (4.27) – Bond-Slip Relationship for Nodes 109-128.....62
Figure (4.28) – Bond-Slip Relationship for Nodes 128-132.....63
Figure (4.29) – Bond-Slip Relationship for Nodes 177-186.....63
Figure (4.30) – Comparison of Input and Output curves.....64
Figure (4.31) – Load-Displacement Diagram.....64
Figure (4.32) – Stresses at the Beginning of the Bend.....65
Figure (4.33) – Stresses at the Face of the Joint.....65
Figure (5.1) - Schematic Bond Slip Models for No, Perfect and Partial Confinement.....73
Figure (5.2) - Global, Interface and Model Coordinate Systems.....73
Figure (5.3) - Flowchart for Automatic Bond Model.....74
Figure (6.1) - Schematic Drawing of Specimen Tested by Lormanometee (1974) and Untrauer et al (1968).....86
Figure (6.2) - Schematic Drawing of Specimen Tested by Minor et al. (1975) (Not to scale).....86
Figure (6.3) - Schematic Drawing of Specimen Tested by Eligehausen et al.(1983).....87
Figure (6.4) – FE mesh for Specimen of Chapter 3.....88
Figure (6.5) – FE mesh for 6 inch cube specimens from Untrauer and Lormanometee.....89
Figure (6.6) – FE mesh for Eligehausen's Specimens.....90
Figure (6.7) – FE mesh for Minor Specimens.....91
Figure (6.8) – Saenz Compression Curve for FE Model of Case 2.....92
Figure (6.9) – Tension Softening Curve for FE Model of Case 2.....92
Figure (6.10) – Saenz Compression Curve for FE Model of Case 3.....93
Figure (6.11) – Tension Softening Curve for FE Model of Case 3.....93
Figure (6.12) – Saenz Compression Curve for FE Model of Cases 4 and 10.....94
Figure (6.13) – Tension Softening Curve for FE Model of Cases 4 and 10.....94

Figure (6.14) – Saenz Compression Curve for FE Model of Cases 5 and 6.....95
Figure (6.15) – Tension Softening Curve for FE Model of Cases 5 and 6.....95
Figure (6.16) – Saenz Compression Curve for FE Model of Cases 7 and 8.....96
Figure (6.17) – Tension Softening Curve for FE Model of Cases 7 and 8.....96
Figure (6.18) – Saenz Compression Curve for FE Model of Case 9.....97
Figure (6.19) – Tension Softening Curve for FE Model of Case 9.....97
Figure (6.20) – Saenz Compression Curve for FE Model of Cases 11 and 12.....98
Figure (6.21) – Tension Softening Curve for FE Model of Cases 11 and 12.....98
Figure (6.22) – Saenz Compression Curve for FE Model of Case 13.....99
Figure (6.23) – Tension Softening Curve for FE Model of Case 13.....99
Figure (6.24) – Saenz Compression Curve for FE Model of Case 14.....100
Figure (6.25) – Tension Softening Curve for FE Model of Case 14.....100
Figure (6.26) – Comparison of the Present Finite Element Approach with Present Test Results.....101
Figure (6.27) – Comparison of the Present Finite Element Approach with Lormanometee's Test Results.....101
Figure (6.28) – Comparison of the Present Finite Element Approach with Lormanometee's Test Results.....102
Figure (6.29) – Comparison of the Present Finite Element Approach with Lormanometee's Test Results.....102
Figure (6.30) – Comparison of the Present Finite Element Approach with Eligehausen's Test Results.....103
Figure (6.31) – Comparison of the Present Finite Element Approach with Eligehausen's Test and Lowes' FEM results.....103
Figure (6.32) – Comparison of the Present Finite Element Approach with Minor's Test Results.....104
Figure (6.33) – Comparison of the Present Finite Element Approach with Minor's Test Results.....104
Figure (7.1) – Schematic Drawing of Models Studied.....121
Figure (7.2) – Schematic Drawing of the Model with Full Hook Development Length.....122

Figure (7.3) – Schematic Drawing of the Loads.....122
Figure (7.4) - FE Mesh for 30M bar with 100 mm bend radius and 12 d_b tail...123
Figure (7.5) - FE Mesh for 30M bar with 100 mm bend radius and 8 d_b tail.....124
Figure (7.6) - FE Mesh for 30M bar with 100 mm bend radius and 4 d_b tail.....125
Figure (7.7) - FE Mesh for 30M bar with 100 mm bend radius,12 d_b tail and straight bonded length of l_d 126
Figure (7.8) - FE Mesh for 30M bar with 200 mm bend radius and 12 d_b tail...127
Figure (7.9) - FE Mesh for 30M bar with 200 mm bend radius and 8 d_b tail.....128
Figure (7.10) - FE Mesh for 30M bar with 200 mm bend radius and 4 d_b tail...129
Figure (7.11) - FE Mesh for 35M bar with 125 mm bend radius and 12 d_b tail..130
Figure (7.12) - FE Mesh for 35M bar with 125 mm bend radius and 8 d_b tail...131
Figure (7.13) - FE Mesh for 35M bar with 125 mm bend radius and 4 d_b tail...132
Figure (7.14) - FE Mesh for 35M bar with 250 mm bend radius and 12 d_b tail..133
Figure (7.15) - FE Mesh for 35M bar with 250 mm bend radius and 8 d_b tail...134
Figure (7.16) - FE Mesh for 35M bar with 250 mm bend radius and 4 d_b tail...135
Figure (7.17) - FE Mesh for 45M bar with 200 mm bend radius and 12 d_b tail..136
Figure (7.18) - FE Mesh for 45M bar with 200 mm bend radius and 8 d_b tail...137
Figure (7.19) - FE Mesh for 45M bar with 200 mm bend radius and 4 d_b tail...138
Figure (7.20) - FE Mesh for 45M bar with 400 mm bend radius and 12 d_b tail..139
Figure (7.21) - FE Mesh for 45M bar with 400 mm bend radius and 8 d_b tail...140
Figure (7.22) - FE Mesh for 45M bar with 400 mm bend radius and 4 d_b tail...141
Figure (7.23) – Compression Curve.....142
Figure (7.24) – Tension Softening Curve.....142
Figure (7.25) – Steel Stress-Strain Diagram.....143
Figure (7.26) – Load-displacement for 30M bar and minimum bend radius.....143
Figure (7.27) – Load-displacement for 30M bar and twice minimum bend radius.....144

Figure (7.28) – Load-displacement for 30M bar, minimum bend radius and straight development length of l_d 144
Figure (7.29) – Load-displacement for 35M bar and minimum bend radius.....145
Figure (7.30) – Load-displacement for 35M bar and twice minimum bend radius.....145
Figure (7.31) – Load-displacement for 45M bar and minimum bend radius.....146
Figure (7.32) – Load-displacement for 45M bar and twice minimum bend radius.....146
Figure (7.33) – Different Locations on the Bar.....147
Figure (7.34) – Slip at Different Locations on the Bend for Case 1.....148
Figure (7.35) – Slip at Different Locations on the Bend for Case 2.....149
Figure (7.36) – Slip at Different Locations on the Bend for Case 3.....150
Figure (7.37) – Slip at Different Locations on the Bend for Case 4.....151
Figure (7.38) – Slip at Different Locations on the Bend for Case 5.....152
Figure (7.39) – Slip at Different Locations on the Bend for Case 6.....153
Figure (7.40) – Slip at Different Locations on the Bend for Case 7.....154
Figure (7.41) – Slip at Different Locations on the Bend for Case 8.....155
Figure (7.42) – Slip at Different Locations on the Bend for Case 9.....156
Figure (7.43) – Slip at Different Locations on the Bend for Case 10.....157
Figure (7.44) – Slip at Different Locations on the Bend for Case 11.....158
Figure (7.45) – Slip at Different Locations on the Bend for Case 12.....159
Figure (7.46) – Slip at Different Locations on the Bend for Case 13.....160
Figure (7.47) – Slip at Different Locations on the Bend for Case 14.....161
Figure (7.48) – Slip at Different Locations on the Bend for Case 15.....162
Figure (7.49) – Slip at Different Locations on the Bend for Case 16.....163
Figure (7.50) – Slip at Different Locations on the Bend for Case 17.....164
Figure (7.51) – Slip at Different Locations on the Bend for Case 18.....165
Figure (7.52) – Slip at Different Locations on the Bend for Case 19.....166
Figure (7.53) – Slip Trend on the Bend at Peak Load for Cases 1 to 3 with $4\,d_b$ to $12\,d_b$ of Tail Length Respectively.....167

Figure (7.54) – Slip Trend on the Bend at Peak Load for Cases 4 to 5 with $4d_b$ to $12d_b$ of Tail Length Respectively.....168

Figure (7.55) – Slip Trend on the Bend at Peak Load for Cases 7 to 9 with $4d_b$ to $12d_b$ of Tail Length Respectively.....169

Figure (7.56) – Slip Trend on the Bend at Peak Load for Cases 10 to 12 with $4d_b$ to $12d_b$ of Tail Length Respectively.....170

Figure (7.57) – Slip Trend on the Bend at Peak Load for Cases 13 to 15 with $4d_b$ to $12d_b$ of Tail Length Respectively.....171

Figure (7.58) – Slip Trend on the Bend at Peak Load for Cases 16 to 18 with $4d_b$ to $12d_b$ of Tail Length Respectively.....172

Figure (7.59) – Slip Trend on the Bend at Peak Load for Cases 19 with $4d_b$ to $12d_b$ of Tail Length Respectively.....173

Figure (7.60) – Standard hook with minimum and twice radii of bend.....174

1. Introduction

1.1. Scope

Bent bars are frequently used in reinforced concrete structures to help develop bar forces up to required capacities where there is shortage of space for straight bar development. These hooks are especially seen at corners and side joints of a building. These joints are essential parts of every reinforced concrete building. Therefore, their behavior has a major role in maintaining the safety of the structures. Figures (1.1) to (1.4) show schematic drawings of a variety of corner joints with hooks as a means of anchorage.

Reinforcement is always designed for the yield capacity at the cross section. Thus, failure to deliver this functionality will result in an un-conservative design. In order to make sure a reinforcement arrangement is strong enough, influential parameters have to be checked. In addition to the reinforced concrete design code CSA-A23.3 provisions for tail length, CSA-A23.3 commentary has a set of provisions with regard to bend radius. However, it is not clear which parameter has more influence on the strength of a hook. In addition, it is not clear if the bend radii proposed in commentary are the most efficient values with respect to capacity. Anchorage becomes more critical when bar diameter is large because with increased bar diameter increased bond is needed to develop the yielding capacity of the cross section. Therefore, the focus of the parametric study in this research is on bars with large diameters.

Reinforced concrete joints can be designed with or without stirrups inside of them based on different conditions in design. In seismic design it is essential to have extra confinement at the joint and, therefore, joints have stirrups. In regions not prone to earthquake there is no need for seismic considerations and thus joints can be stirrup free if other design requirements including cover are met. Hooks can be bent with minimum radius given in CSA-A23.3 commentary as well as a bend radius larger than the minimum. In the parametric study of this research the

effects of bend radius and tail length are studied. However, to accomplish this objective an appropriate finite element model is developed.

Part of this research, therefore, is an attempt to model and predict the behavior of reinforced concrete structures with respect to bond and anchorage. For this reason, explicit modeling of concrete-steel interface is considered. This ensures that further predictions by this modeling are reliable. The stated model has to account for various influential parameters that affect the behavior. In addition, it has to give close results in comparison to present and previous test results. Furthermore, it accounts for confined and unconfined conditions. After the completion of test, modeling and verification a number of the provisions of the Canadian code with respect to hook development will be studied and an evaluation is presented.

1.2. Objectives

Several objectives are pursued in this research. First, a finite element bond model is developed which is able to model confined and unconfined conditions. Both active confinement under compressive pressure and passive confinement provided by lateral reinforcement are studied. Secondly, this model is verified with many test results from the present experimental work and past researchers' experiments. As explained in the forthcoming chapters, implementation of the proposed model is extremely time consuming and uneconomical. Therefore, as the third objective, a comprehensive automatic interface model is developed to save tremendous time in analysis and to eliminate the necessity of performing a large number of trials and errors for each case of analysis. The last objective is to perform a parametric study on hooks with respect to bend radius and tail length.

1.3. Methodology

This research has been conducted in three phases. In stage one, a knee joint under closing moment has been designed, fabricated, instrumented and tested. As the second phase, a finite element analysis is carried out to model the test. However,

there are major complexities involved in this kind of analysis. Thus, an appropriate bond model is developed to enable the general purpose software ABAQUS to accurately analyze this specimen. The problem with the proposed bond model was that it needed an iterative procedure to converge to acceptable results. This iterative procedure was very time consuming and tedious to use. Therefore, as the third phase, a constitutive model is developed which is automatic and convenient to implement as a user subroutine in the software. To make sure the constitutive model is working properly, a set of evaluative analyses was carried out to compare the results of analysis and tests. Good agreement with present and previous experiments was achieved. The developed model was then used to study the behavior of bent large diameter bars. The anchorage of these bars was evaluated and suggestions for improvement to code provisions were made.

1.4. Outline of the Thesis

In chapter (2), major related research by past researchers is presented. In chapter (3) the experimental work for this thesis is presented. Chapter (4) explains how finite element modeling and analysis are carried out as well as how the proposed bond model is developed. Chapter (5) is a description of how to automate the procedure to save time and avoid trials and errors. In chapter (6), several cases of analysis are carried out to verify the proposed bond model against the present test and experimental work by past researchers. Chapter (7) presents a parametric study of hooks with large bar diameters. In this chapter analysis results are compared to code predictions and conclusions and suggestions are made to improve development of the bars with diameters studied.

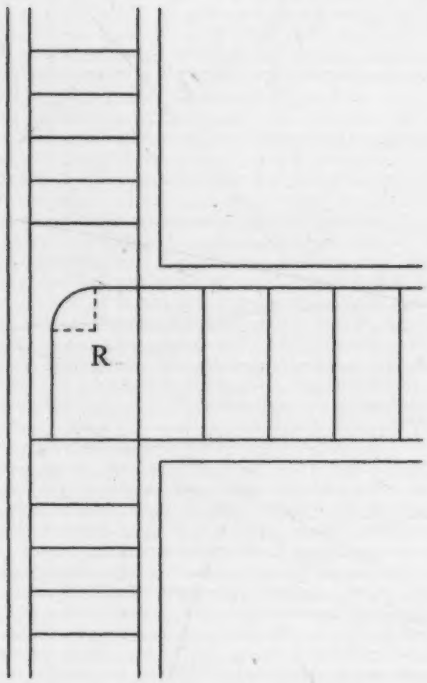

Fig (1.1) – Corner Beam-Column Connection with Minimum Bend Radius

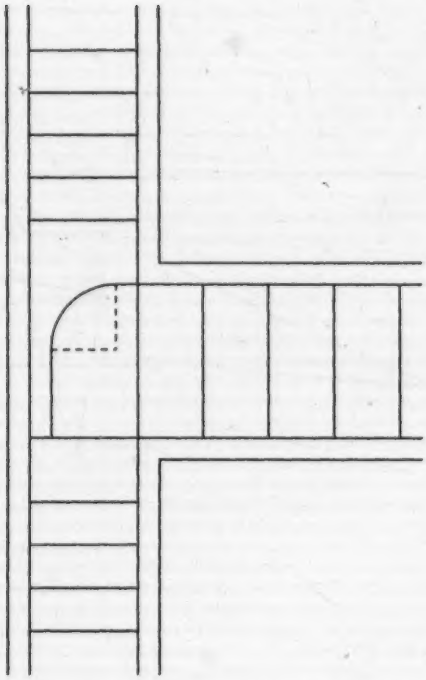

Fig (1.2) – Corner Beam-Column Connection with a Bend Radius Larger Than Minimum

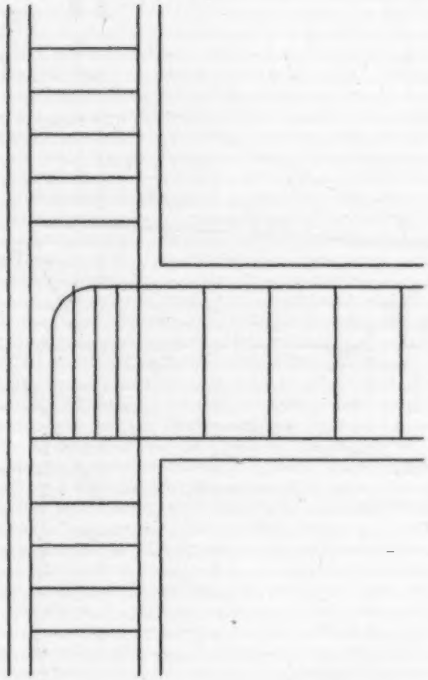

Fig (1.3) – Corner Beam-Column Connection Vertical Stirrups

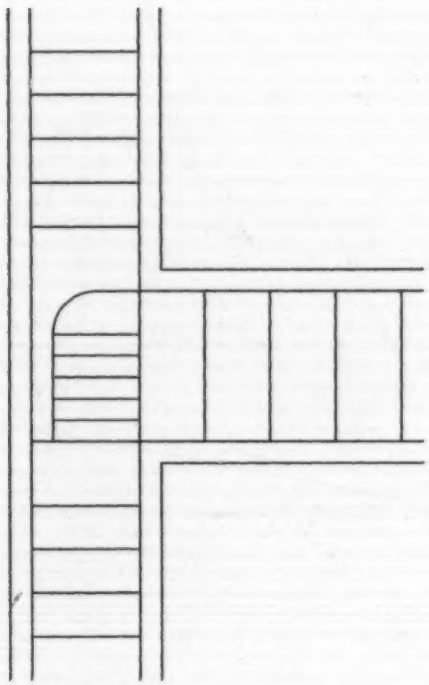

Fig (1.4) – Corner Beam-Column Connection with Horizontal Stirrups

2. Literature Review

2.1. Introduction

There are two different types of modeling of bond in structures. The first one considers full compatibility of displacement between concrete and bars. In this type of approach, bars are embedded elements into the concrete elements and the behavior of bond is modeled implicitly by modifying the concrete material properties. This is accomplished using a tension stiffening diagram. Figure (2.1) shows a schematic illustration of tension stiffening for plain and reinforced concrete. This diagram indicates that in tension tests reinforced concrete exhibits more tension capacity than reinforcement without concrete. In other words, some of the tension resistance in reinforced concrete is due to the concrete itself. The transfer of forces from reinforcement to concrete is by bond. Therefore, modeling the tension stiffening phenomenon numerically along with embedded bar elements means that bond is considered indirectly. This approach is particularly suited to structures with distributed reinforcement such as slabs and walls. An example of this type of analysis is the work by Link et al (1989) where they analyzed a slab with distributed reinforcement in two inclined directions. Their slab is shown in figure (2.3). Application of this approach is not desirable when bond behavior and anchorage of single bars are going to be studied.

Another method of modeling is to consider the interaction of bars and concrete explicitly. In this respect, coincident steel and concrete interfaces are defined and then related using a bond-slip model. A typical bond-slip relationship is shown in figure (2.2). A bond-slip model associates the bond of steel-concrete interface to the slippage of surfaces on one another. The bond-slip model can involve many other parameters besides slippage and thus is more effective in the research focusing on bond development. The second is used in this research. This has been partly accomplished through careful study of many different cases of

experimental work other researchers have done. Hence, a review of the past researchers' work on bond is of special interest for this thesis.

2.2. Experimental Work by Past Researchers

There are various methods to measure the bond between concrete and steel. The simplest form of measurement used by many researchers is to conduct a pullout test and divide the applied tension force by the peripheral surface of the bar to find the average bond at any time during the test. Among the many researchers who used this method are Malvar (1992), Eligehausen et al. (1983), Untrauer et al. (1968), Lormanometee (1974) and Thro et al. (1987). Another approach is direct measurement of bond at various locations along the length of the bar in a pullout or tension test. In this approach, strain gauges are installed at different locations on the reinforcement and the bond is computed in terms of the gradient of stress with respect to length. The work by Nilson (1972) is of this type.

Nilson (1968, 1972) performed a tension test on a rectangular prism specimen with a steel bar in the middle and strain gauges placed at various locations on the bar. Concrete gauges were placed inside concrete and close to steel surface to measure the strain in concrete. Nilson (1972) presented an equation to find slip in terms of steel and concrete strains. Nilson's specimen is shown in figure (2.4).

Malvar (1992) did a series of eleven experiments with cylindrical concrete specimens confined with a confining ring that applied normal radial pressure on the surface of concrete. The level of normal pressure was different in different specimens. The steel bar was placed in the middle of concrete cylinder and pulled out gradually. Malvar (1992) concluded that bond increases with increased confinement and bars with lugs perpendicular to the bar are more effective than the ones with inclined ribs. Figure (2.5) illustrates Malvar test specimen.

Eligehausen et al. (1983) carried out one hundred twenty five pullout tests on rectangular prism concrete specimens with a steel bar in the middle. This team

tested different confining pressures and different stirrup sizes as well as vertical reinforcement ratios, load rates and load types. They also performed experiments on the effect of rate of loading. Eligehausen et al. (1983) concluded that the bond capacity increases with increased normal pressure and that lateral reinforcement improves both the ultimate bond capacity and the bond slip response.

Untrauer et al. (1968) performed a set of thirty seven tests on 6 inch cube concrete specimens with a steel bar in the middle which is pulled out gradually. The specimens were tested under different conditions of concrete strength and normal pressure applied on the top and bottom of specimens. Untrauer et al. (1968) concluded that normal pressure has an increasing effect on maximum bond and the splitting cracks occur in a plane normal to the pressure surface along the bar.

Lormanometee (1974) carried out sixty pullout tests on a set of cube and rectangular prism specimens with steel bars in the middle and normal pressure on two opposing surfaces of these specimens. Different bar sizes and different pressure levels were investigated. Lormanometee (1974) concluded that confining pressure is more effective when applied on cube specimens rather than prism specimens. Figures of test setups by Eligehausen, Untrauer and Lormanometee will be presented in the verification chapter since they are used for that purpose.

Gambarova et al. (1997, 1998) carried out a series of pullout experiments on cylindrical and rectangular prism concrete specimens with a bar in the middle shown in figure (2.6). Their specimens included pre-split cracks that made it possible to control the cracking and location of concrete failure. Confining normal pressure was applied at different levels on their specimens. Gambarova et al. (1997, 1998) presented limit analysis equations for bond capacity in terms of number of pre-split cracks, width of pre-split cracks as well as level of confinement. Figure (2.6) shows Gambarova et al. (1997, 1998) test setup.

As for hook pullout tests, Marques et al. (1975) tested a series of twenty two

column specimens shown in figure (2.5) with #8 longitudinal bars and #7 or #11 hooks in the middle of the column. The columns had different types of confinements. Shear and axial forces were applied at the two ends of columns while the hook was pulled. Marques et al. concluded that when side splitting is restrained hook strength is increased and that 90 and 180 degree hooks do not differ in behavior. The test setup by Marques et al. (1975) is shown in figure (2.7).

Figures of test setup by Untrauer et al. (1968), Eligehausen et al. (1983) and Lormanometee (1974) will be presented in chapter 6. Properties of straight bar pullout and tension specimens used in forthcoming chapters of this research are given in table 2.1.

2.3. Analytical Work by Past Researchers

One of the earliest finite element approaches to reinforced concrete has been done by Ngo et al. (1967). Ngo et al. modeled the bond between concrete and steel surfaces with spring elements. Normal interaction was also modeled using spring elements. These springs had constant stiffness. Nilson (1968) proposed a curve for bond in terms of slip and used springs to connect the nodes of steel and concrete elements interacting by bond. Hofstetter (1995) reported that Keuser et al. (1987) and Mehlhorn (1990) developed bond elements that worked better than spring elements while Miguel et al. (1990) used a combination of bond elements and spring elements to model steel-concrete interaction. Lowes et al. (2004) proposed a bond-slip model and an interface element for confined concrete. However, their approach does not render appropriate results for unconfined concrete. Equations (2.1) to (2.3) show the relationship proposed by Lowes et al. (2004) for bond-slip behavior. Their relationship is in close agreement with Eligehausen et al. test results. All these studies were carried out using two dimensional representations of the specimens. In addition there are other deficiencies in these models such as inadequate modeling of confinement since they are able to model some conditions such as specimens with both stirrups and

confining pressure but are not able to give accurate results for other situations such as confining pressure only.

$$\tau_b = \begin{cases} \tau_1\left[f\left(\frac{s}{s_1}, 0.15, 2\right)\right] + \tau_r\left[f\left(\frac{s}{s_1}, 10^{-6}, 20\right)\right] + \tau_v\left[f\left(\frac{s}{s_1}, 10^{-6}, 20\right)\right] & s \prec s_1 \\ \tau_1 + \tau_r\left[f\left(\frac{s}{s_1}, 10^{-6}, 20\right)\right] + \tau_v\left[f\left(\frac{s}{s_1}, 10^{-6}, 20\right)\right] & s_1 \prec s \prec s_2 \\ \left[\tau_1 + k_3(s - s_2)\right] + \tau_r\left[f\left(\frac{s}{s_1}, 10^{-6}, 20\right)\right] + \tau_v\left[f\left(\frac{s}{s_1}, 10^{-6}, 20\right)\right] & s_2 \prec s \prec s_3 \\ \tau_r\left[f\left(\frac{s}{s_1}, 10^{-6}, 20\right)\right] + \tau_v\left[f\left(\frac{s}{s_1}, 10^{-6}, 20\right)\right] & s \succ s_3 \end{cases} \quad (2.1)$$

Where, τ_b is the total bond stress. $s, s_1, s_2, s_3, , \tau_1, \tau_r$ and τ_v represent slip, slip corresponding to peak bond, slip where bond starts to decrease, slip where mechanical interaction fails, mechanical bond, residual friction and virgin friction. Residual and virgin frictions are small values of bond remaining after mechanical failure. The function f is described in equation (2.2)

$$f(u, b, R) = \left[b + (1-b)\left[\frac{1}{1+|u|^R}\right]^{1+\frac{1}{R}}\right]u \quad (2.2)$$

$$\tau_1 = 0.8\Gamma_0\Gamma_1\Gamma_2\Gamma_3\Gamma_4\Gamma_5 \quad (2.3)$$

$$\Gamma_0 = 2.1\left[1 + 0.35\left(1 - \exp\left(-40\frac{p}{f_c'}\right)\right) + 0.4\left(1 - \exp\left(-\frac{p}{f_c}\right)\right)\right]\sqrt{f_c'} \quad (2.4)$$

$$\Gamma_1 = \exp(-H\alpha) \quad (2.5)$$

$$\Gamma_2 = \begin{cases} 1 + 1.4\left(1 - \exp\left(0.4\left(1 + \frac{\varepsilon}{\varepsilon_y}\right)\right)\right) & \varepsilon \prec \varepsilon_y \\ 0.1 + 0.9\left(\exp\left(0.4\left(1 - \frac{\varepsilon}{\varepsilon_y}\right)\right)\right) & \varepsilon \succ \varepsilon_y \end{cases} \quad (2.6)$$

$$\Gamma_3 = 0.27 + 0.58\exp\left[-0.225(s_{max} - s_{min})(1 - \exp(-20(N - 0.25)))\left(N^{-0.16-0.43(s_{max}-s_{min})}\right)\right] \prec 1 \quad (2.7)$$

$$\Gamma_4 = \begin{cases} 1.09 & d_b \le 19mm \\ 1.09 - \dfrac{0.18}{13}(d_b - 19) & 19mm \le d_b \le 32mm \\ 0.91 & d_b \succ 32mm \end{cases} \tag{2.8}$$

$$\Gamma_5 = \begin{cases} 0.8 & c \le d_b \\ 1 - 0.067\left(4 - \dfrac{c}{d_b}\right) & d_b \le c \le 4d_b \\ 0.1 & c \succ 4d_b \end{cases} \tag{2.9}$$

Where, $p, f_c', H, \alpha, \varepsilon, \varepsilon_y, s_{\max}, s_{\min}, N, c$ and d_b present confining pressure, strength of concrete, softening parameter, damage parameter, steel strain, steel yield strain, maximum historic slip, minimum historic slip, number of load cycles, concrete cover and diameter of bar. Radial forces are represented by equation (2.3).

$$\sigma_{rad} = \begin{cases} \tau_1\left[f\left(\dfrac{s}{s_1}, 0.15, 2\right)\right] + f_{rad}(r) & s \prec s_1 \\ \tau_1 + f_{rad}(r) & s_1 \prec s \prec s_2 \\ \left[\tau_1 + \dfrac{\tau_1}{9}(s - s_2)\right] + f_{rad}(r) & s_2 \prec s \prec s_3 \\ f_{rad}(r) & s \succ s_3 \end{cases} \tag{2.10}$$

Here, f_{rad} is a deformation dependent function that is specified for each case of analysis. Figures (2.8) and (2.9) show Nilson and Lowes et al. approaches.

Researcher	Number of Specimens Tested	f_c' (MPa)	f_y (MPa)	C/D
Malvar	11	39-44	400	1.5
Nilson	Not Available	30	280	2.5
Untrauer	37	25-45	634	2.2-3.5
Eligehausen	125	30	400	2
Lormanometee	60	27-36	400	2.2-3.5

Table 2.1 – Properties of Specimens

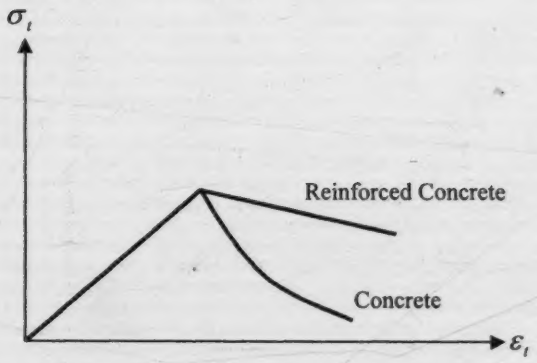

Figure (2.1) – Tension Stiffening

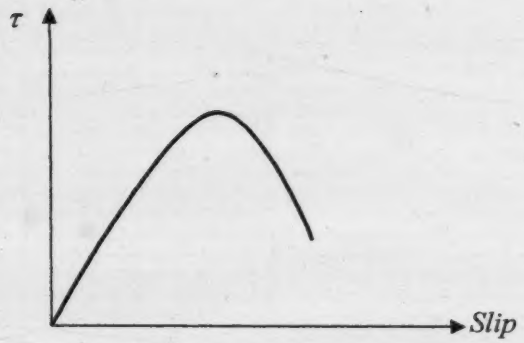

Figure (2.2) – Typical Bond Slip Relationship

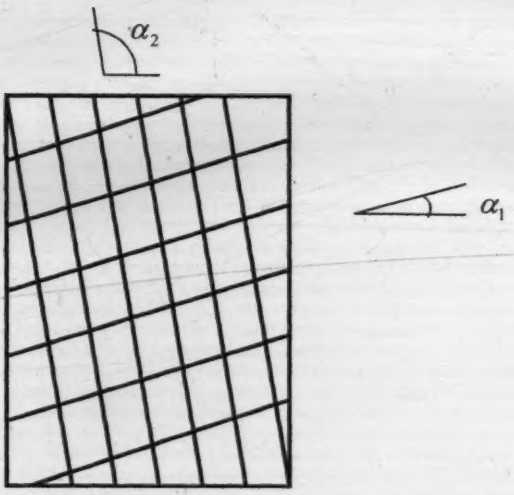

Figure (2.3) – Slab with Distributed Reinforcement in 2 Directions by Link et al. (1989)

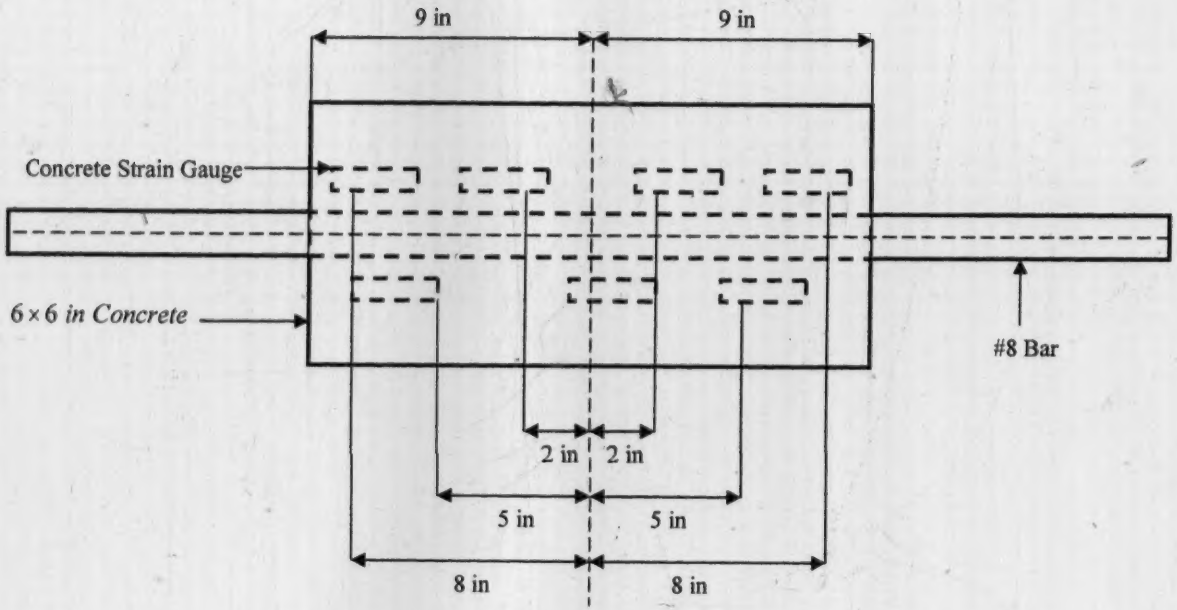

Figure (2.4) – Schematic Drawing for Nilson's (1972) Test Setup

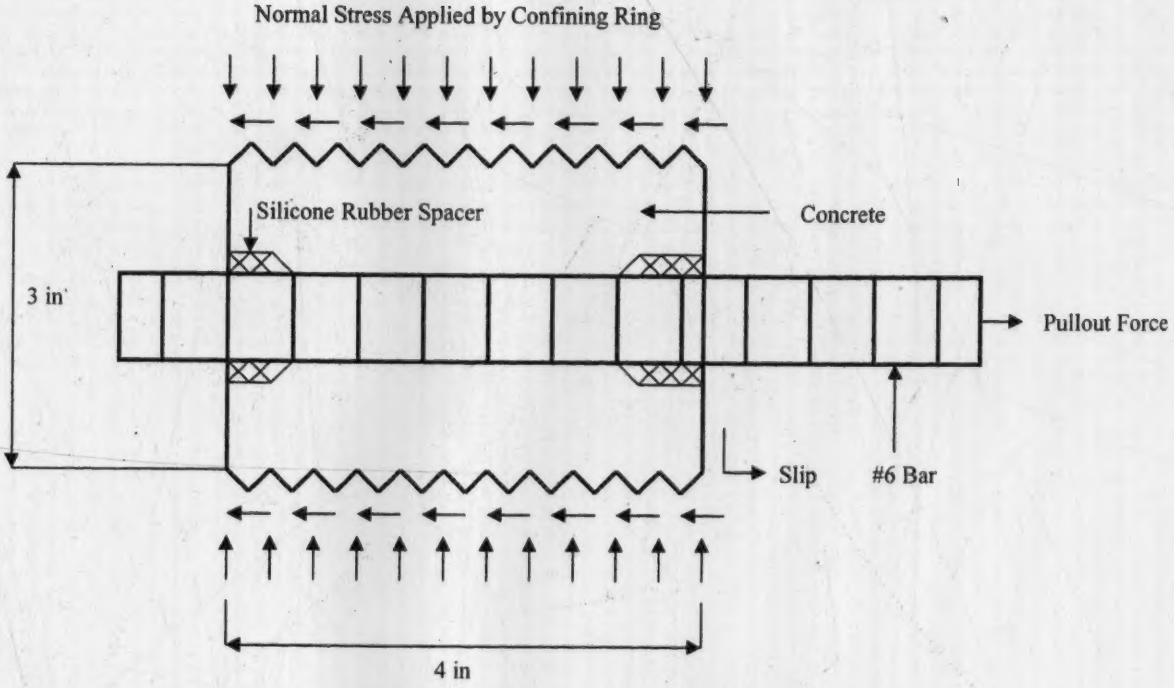

Figure (2.5) – Schematic Drawing for Malvar's (1992) Test Setup

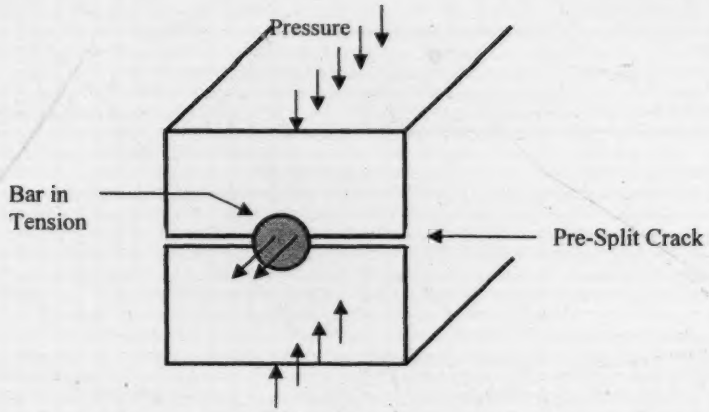

Figure (2.6) – Schematic Drawing for Gambarova's (1998) Test Setup

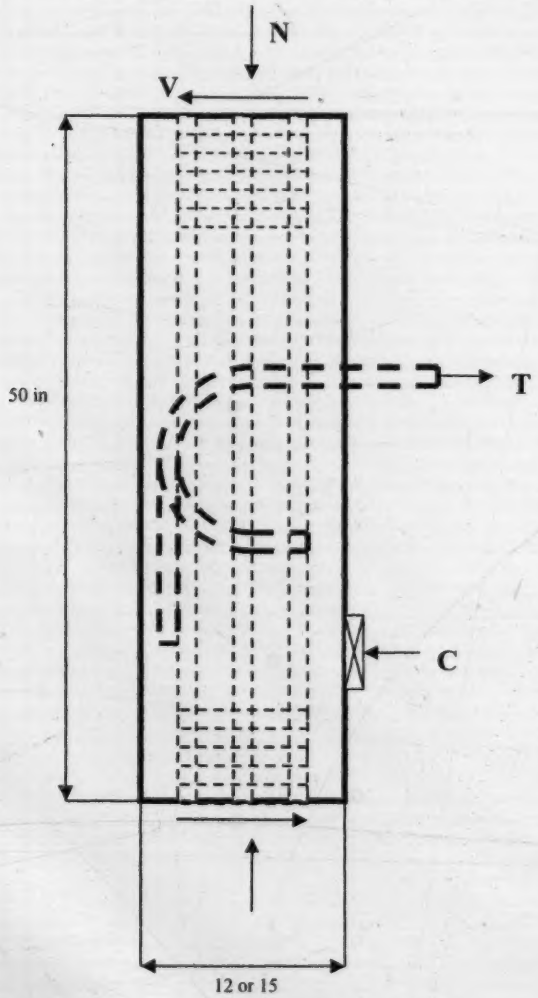

Figure (2.7) – Schematic Drawing for Marques et al. (1975) Test Setup

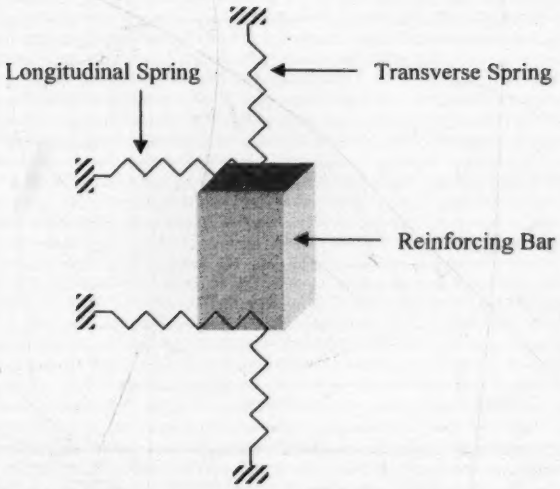

Fig (2.8) – Spring Elements by Nilson (1968)

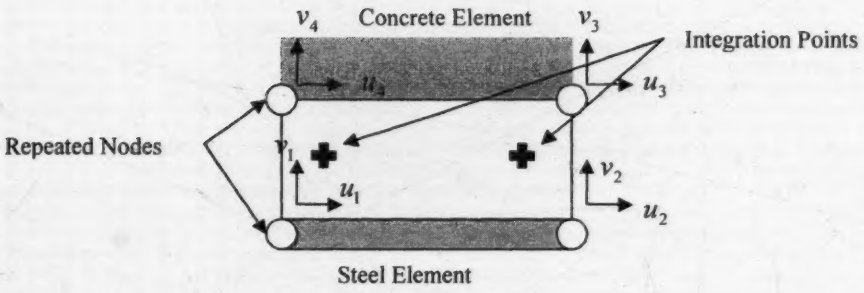

Fig (2.9) – Bond Element by Lowes et al. (2004)

3. Experimental Work

3.1. Introduction

Beam-column joints are one of the most important parts of a reinforced concrete structure. They are also the most challenging in finite element analysis. In designing this test it was important to make the specimen as simple as possible. At first, it was intended to design a joint under pure moments but later it was decided to go for a knee joint to have an easy loading format to apply. The simplest and the most practical way to test a reinforced concrete joint in laboratory is loading a knee joint in a universal servo controlled machine. This will produce closing moments, shear and axial force at the face of the joint. Since a reinforced concrete joint is a disturbed region, a strut and tie model is an effective way to design it. The results of this test will be used in a comparison against a finite element analysis.

3.2. Specimen Design

As mentioned above, strut and tie model has been used for designing of the specimen shown in figure (3.1). This method works with a series of load paths which are either in tension or compression called ties and struts respectively. The load paths chosen in strut and tie models are simplified and are approximations of what happens in reality. The indications P and F are approximations of strut and tie forces in figure (3.1). This is in fact an analogy to truss since a truss works with tension and compression members only. Special care was taken to ensure compression struts will not crush under peak compression stresses. This is accomplished by checking the dimensions of C-C-C, C-C-T and C-T-T nodes and by checking maximum compressive stresses along the length of struts. In addition, there has to be sufficient steel bars at the place of tension ties to make sure tension can be transferred throughout the model. The present specimen was designed for a capacity up to yielding of bars at the face of the joint. However, choice of hook development length was made in a way that the bars cannot fully develop yield strength and, therefore, they have to fail by loss of bond according

to the provisions of the Canadian concrete design code CSA, A23.3-94. This will ensure we can study the effect of partial confinement on bond capacity since other modes of failure have been eliminated. Partial confinement results from the normal pressure produced in the bend region. Thus, at the time one face of steel is under normal pressure the other is not.

According to CSA-A23.3 the hook development length as shown in figure (3.2) is the distance from the critical cross-section to the back surface of the hook. For 35M bars embedded into 35 MPa concrete the hook development length is 603 mm. However only 375 mm of development length was provided to make sure failure happens by splitting.

3.3. Test Setup

The specimen shown in figure (3.3) was tested under compressive force from MTS-6000 machine that will produce negative moment in the joint region. The layout of steel reinforcement is shown in figure (3.4). The strength of concrete and reinforcement were 35MPa and 400MPa respectively. The diameters of the longitudinal and shear reinforcement are 35mm and 15mm respectively. The longitudinal reinforcement is bent by 90 degrees in the middle with a diameter of 10 inches and is hooked by 180 degrees at both ends with the same diameter as the middle bend. The specimen is symmetric. The two ends of specimen have cross-section dimensions of $400mm \times 623mm$. In addition, the two ends of specimen have a length of 200 mm. Each arm of the specimen is 1000 mm long with the cross-section dimensions of $400mm \times 440mm$. Three layers of 35M longitudinal tension reinforcement were used. There were two layers of 20M longitudinal compression bars. Seven layers of 15M stirrups were positioned at 100 mm center to center. The clear concrete cover at the side, top and bottom were 22.5 mm, 65 mm and 80 mm respectively. The loading point was 283 mm below the top of the cross-section of specimen end.

3.3.1. Specimen Details and Instrumentation

Two 19mm thick steel plates were installed inside the wooden formwork at the two ends along with four steel studs welded to each plate to anchor them inside the concrete which was poured later on. Surface dimensions of the plates were the same as the two ends of the specimen. These plates help distribute the MTS-6000 compression load on the two ends to prevent the crushing of concrete at these locations.

One knife edge was installed on every plate to serve as a pin support for the specimen. Two restraining arms were secured on the top knife edge attaching to a steel column at the other end to prevent overturning of specimen during installation before loading. These arms were released after the loading began. Figure (3.4) shows the test setup.

Vertical displacement measurement is taken by LVDT's from the top end to the ground and from the corner to the ground. Figure (3.5) shows LVDT's. Strain gauges were installed from the face of the joint to the beginning of the bend shown in figure (3.8).

3.3.2. Results

The loading method was displacement control with an approximate rate of loading of 0.001 millimeters per second. Figure (3.6) shows the loading of the specimen. The loading was stopped several times to facilitate the demec readings however the demec data was never used because the growth of splitting cracks were so obvious there was no need to prove lateral expansion of crack widths by demec readings as with increased loading demec reading became impossible since the distance between demec targets became larger than the gauge.

The failure was by splitting of the concrete at the joint region near the peak load and as a result the side covers spalled off and then a descending branch occurred on load versus displacement diagram as can be seen in (3.7). The failed specimen is shown in figure (3.8). In the load-displacement diagram, the vertical

displacement is the average of the two measurements taken during the test as can be seen in the following equation:

$$\Delta = \frac{2\Delta_1 + 2\Delta_2}{2} = \Delta_1 + \Delta_2 \qquad (3.1)$$

Figure (3.10) shows the strain gauges placed at the beginning of the bend and the face of the joint. Figures (3.11) to (3.20) show strains at various locations for the working strain gauges.

As seen in figures (3.15) and (3.20) the values of peak average strains at the beginning of the bend and at the face of the joint are close. It means that at the peak load the value of average bond in the straight part of the joint reinforcement is small. This is because bond stress is a demand stress produced by the gradient of axial stress between two locations. In other words, the resultant force from bond stress between any two locations has to balance with the resultant forces obtained from the stress values in the cross-sections corresponding to these locations. Additionally, bond is the result of interaction between steel and concrete surfaces adjacent to each other. However, after the peak and close to the end of the test the stress at the beginning of the bend drops more than the stress at the face of the joint. Therefore, large bond stresses will be produced on the straight part of the joint region reinforcement between the face of the joint and the beginning of the bend.

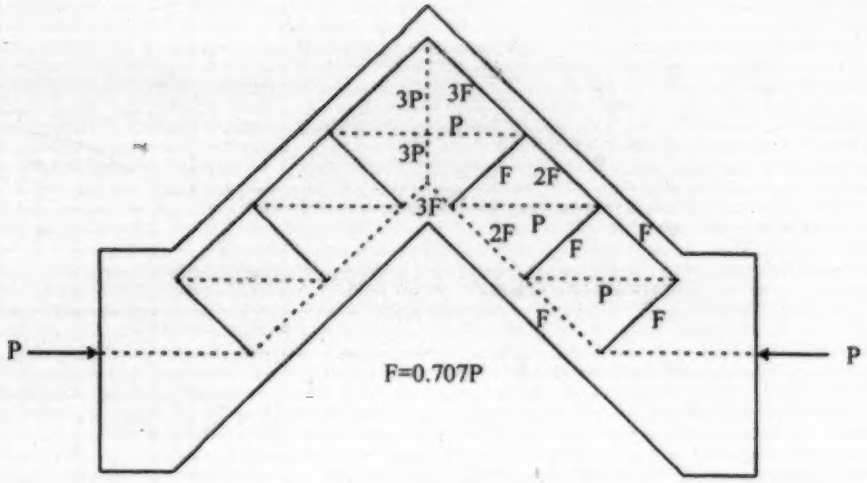

Figure (3.1) - Strut and Tie Model

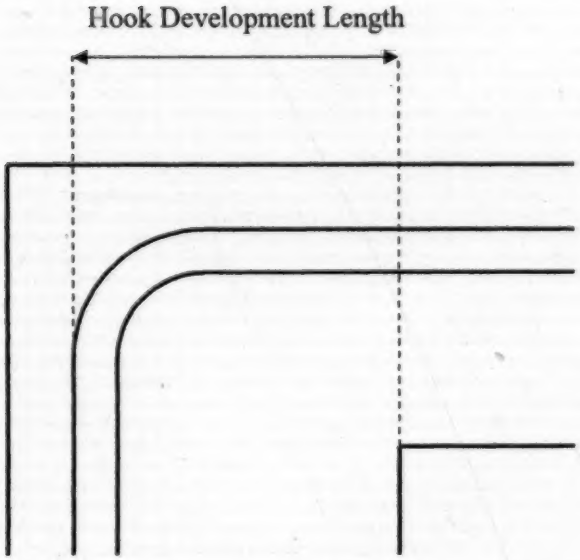

Figure (3.2) – Hook Development Length

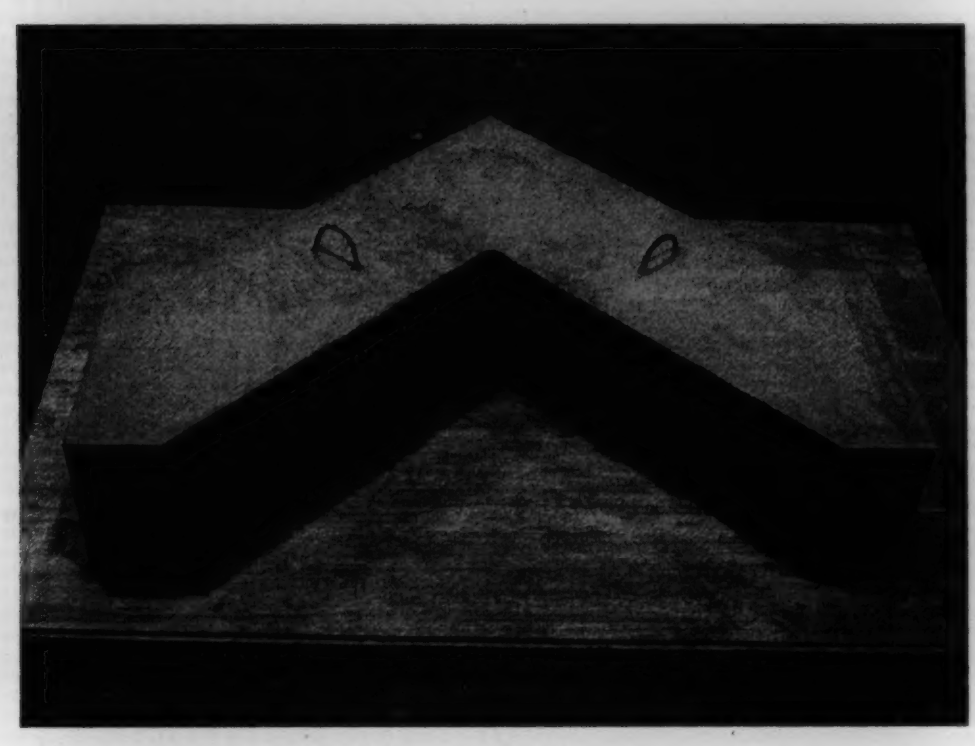

Figure (3.3) – Test Specimen

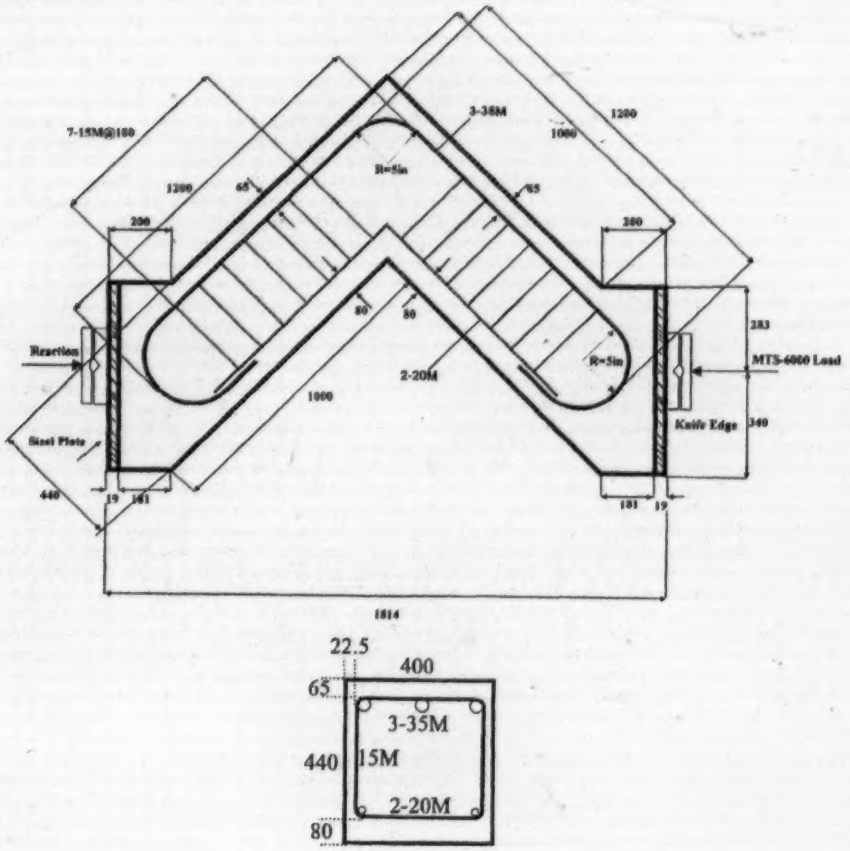

Fig (3.4) – Reinforcement

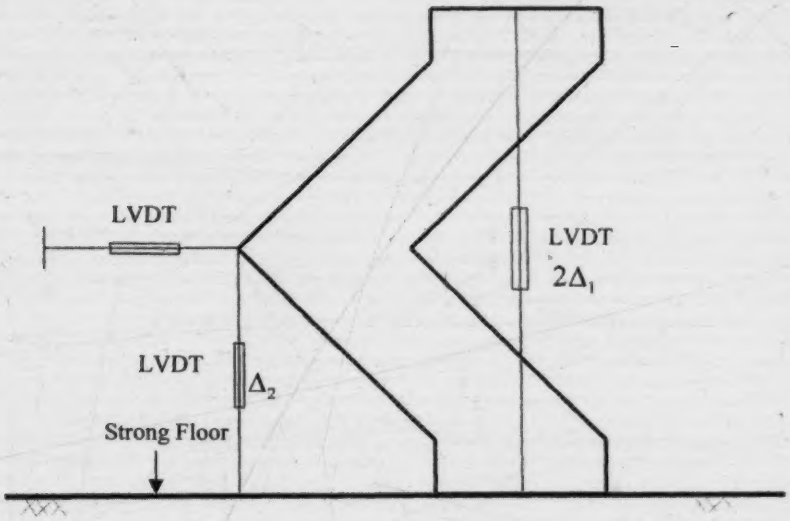

Fig (3.5) – LVDT's

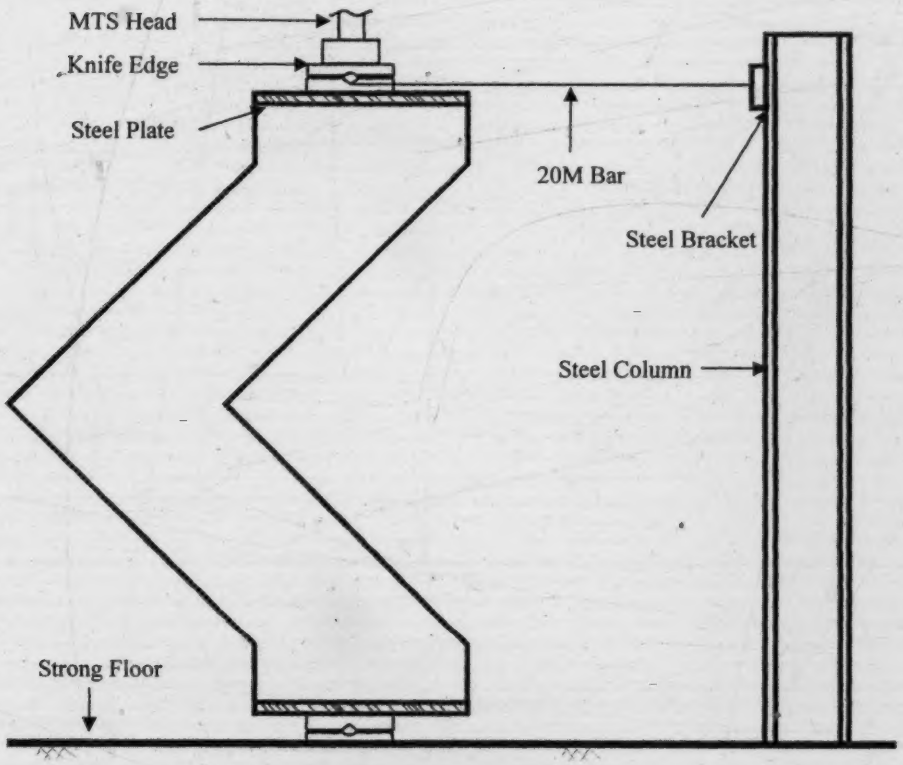

Fig (3.6) – Loading of Specimen

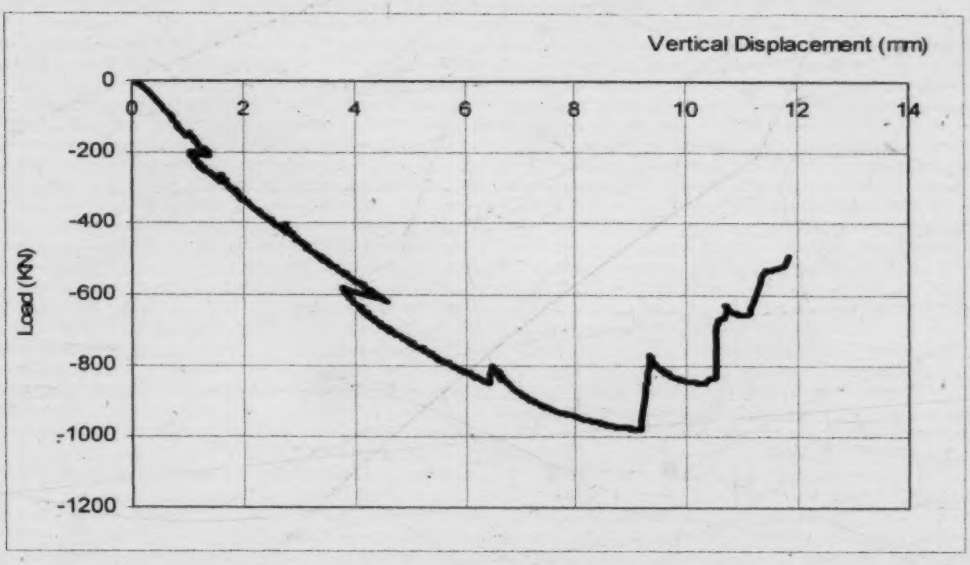

Figure (3.7) – Load-Displacement Diagram

Figure (3.8) – Failed Specimen

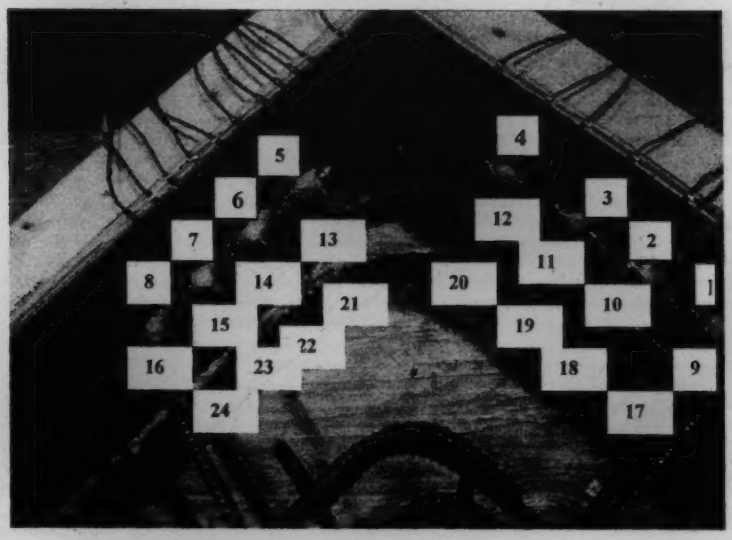

Fig (3.9) – Strain Gauges

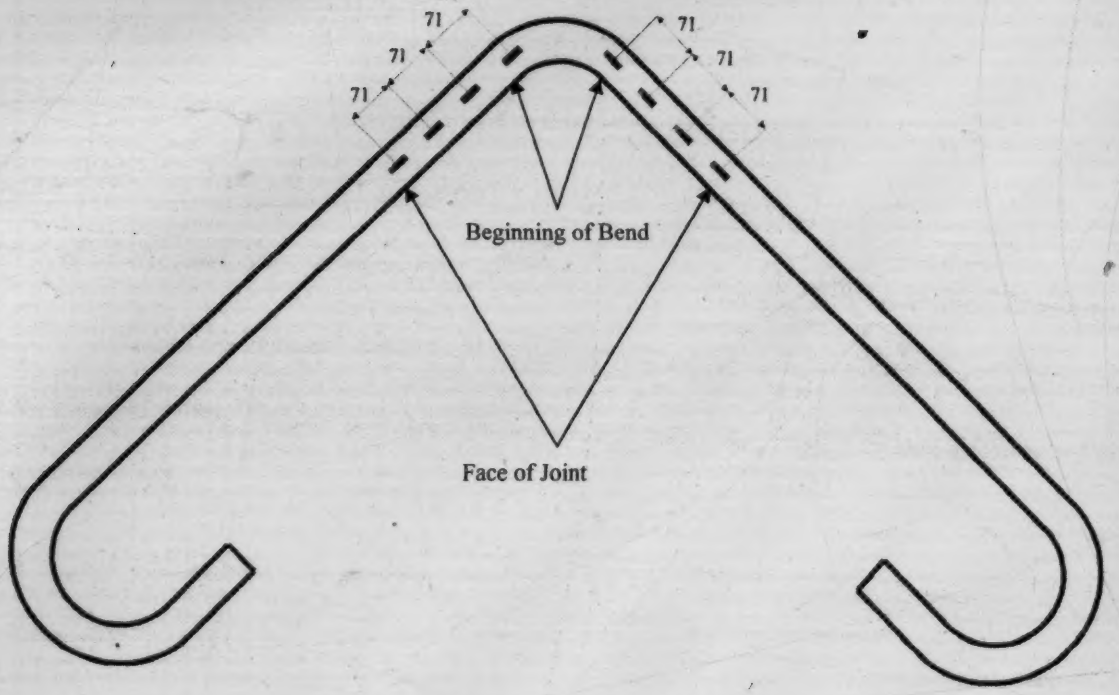

Figure (3.10) - Strain Gauges at the Beginning of the Bend and at the Face of the Joint

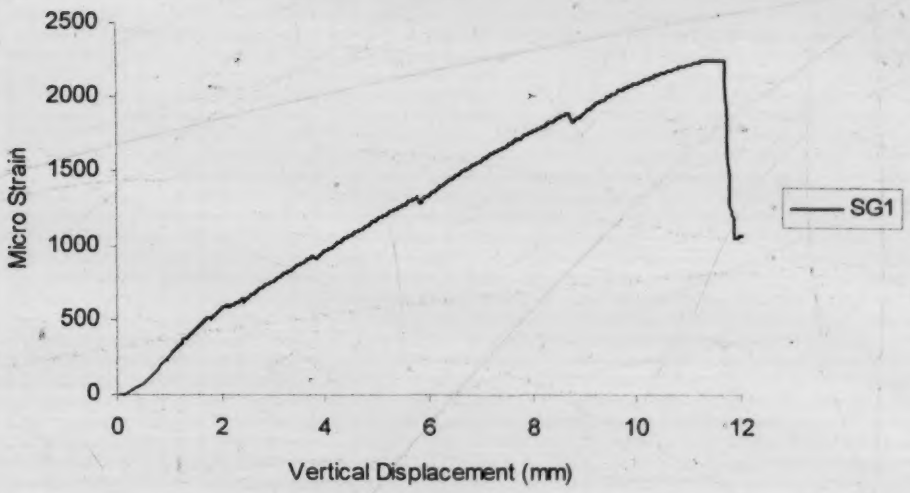

Figure (3.11) – Strain at the Face of the Joint for SG1

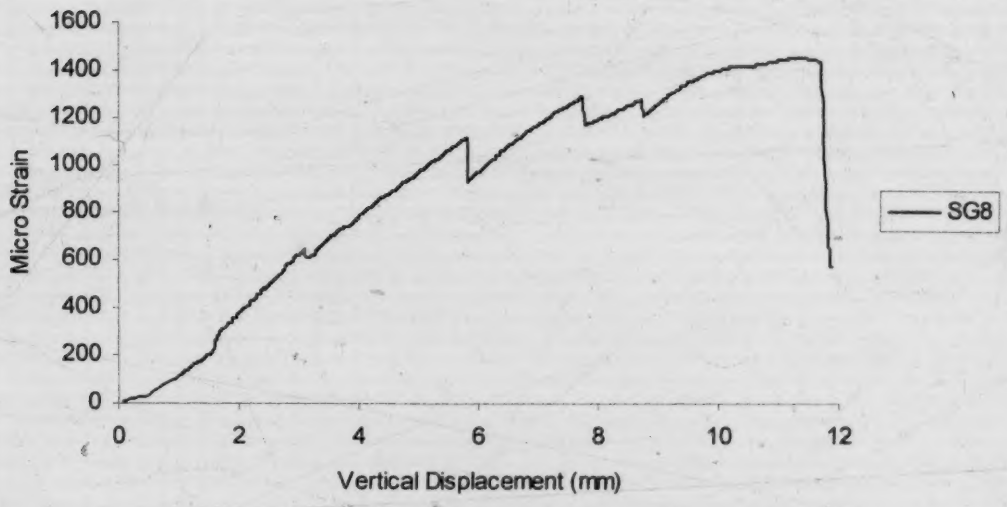

Figure (3.12) – Strain at the Face of the Joint for SG8

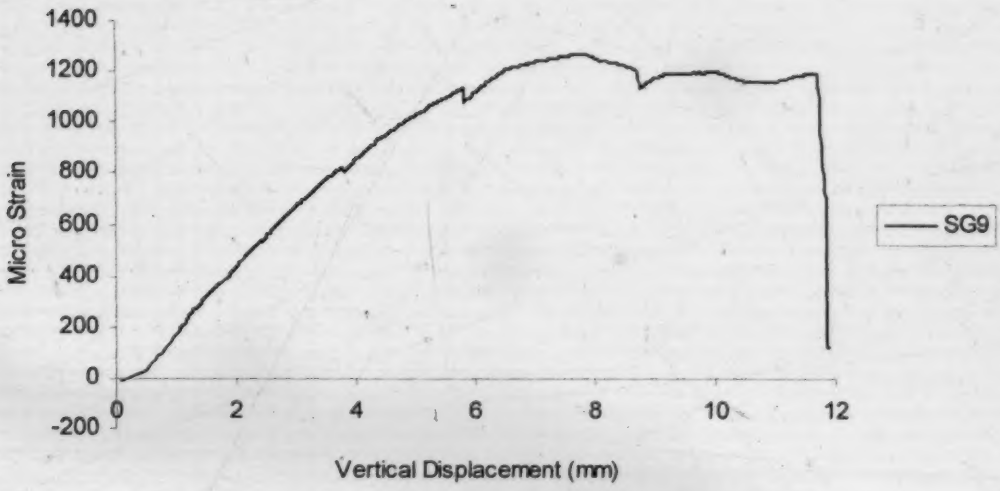

Figure (3.13) – Strain at the Face of the Joint for SG9

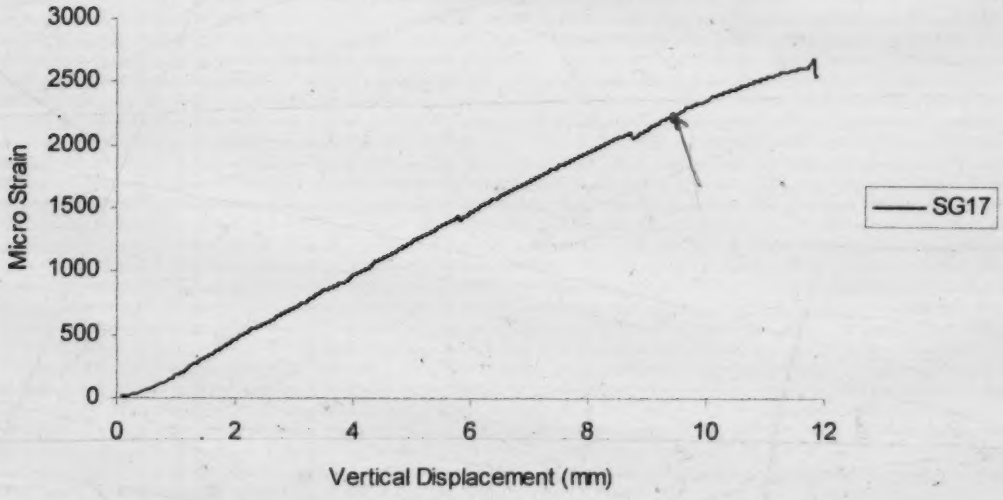

Figure (3.14) – Strain at the Face of the Joint for SG17

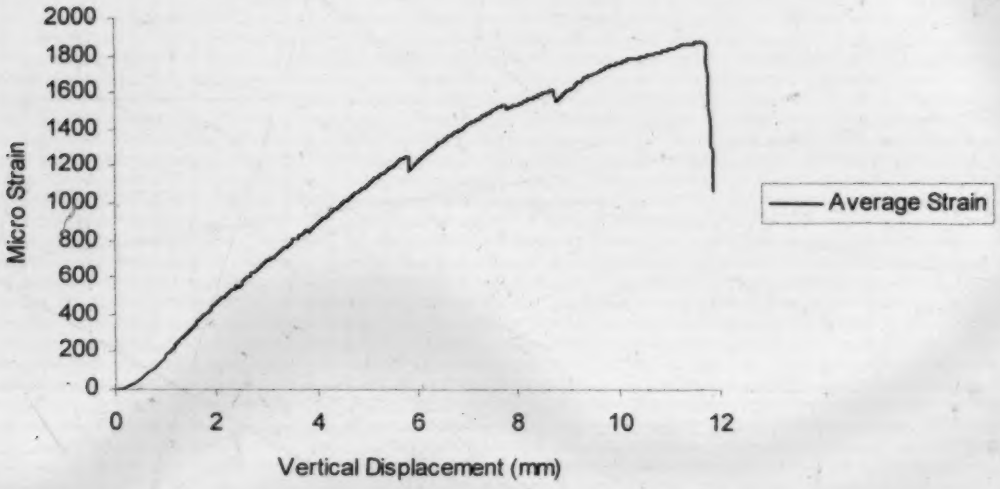

Figure (3.15) – Average Strain at the Face of the Joint

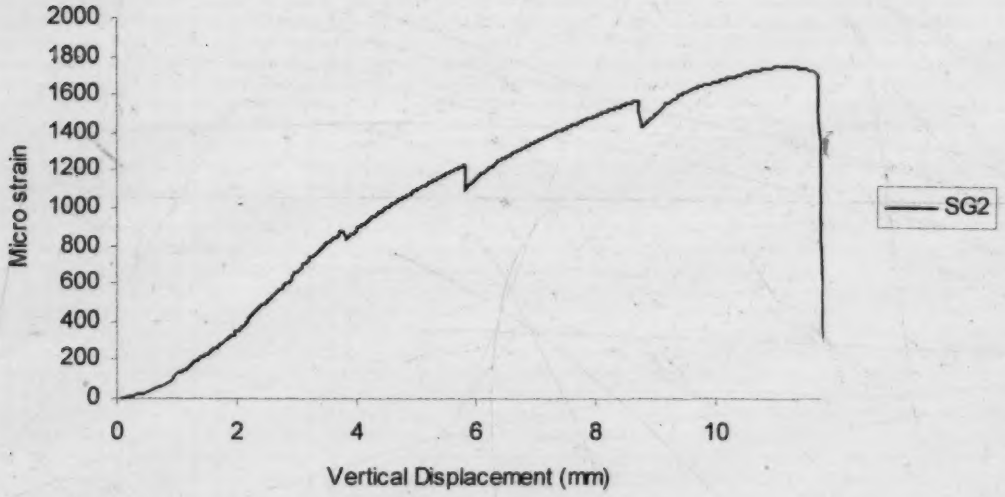

Figure (3.16) – Strain at SG2

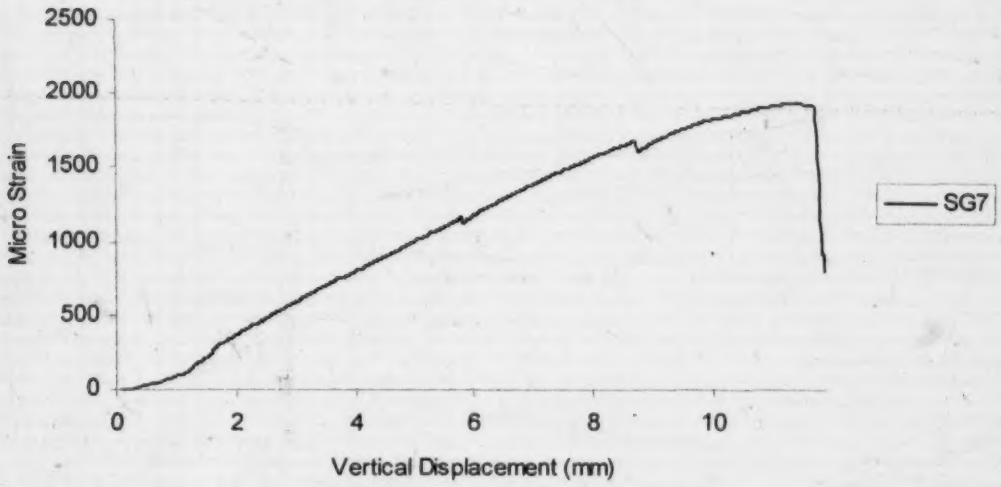

Figure (3.17) – Strain at SG7

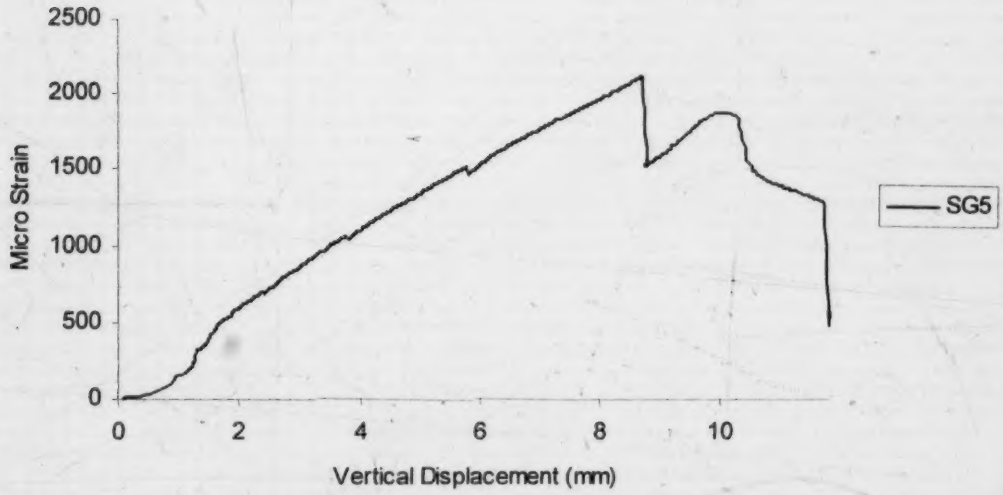

Figure (3.18) – Strain at SG5

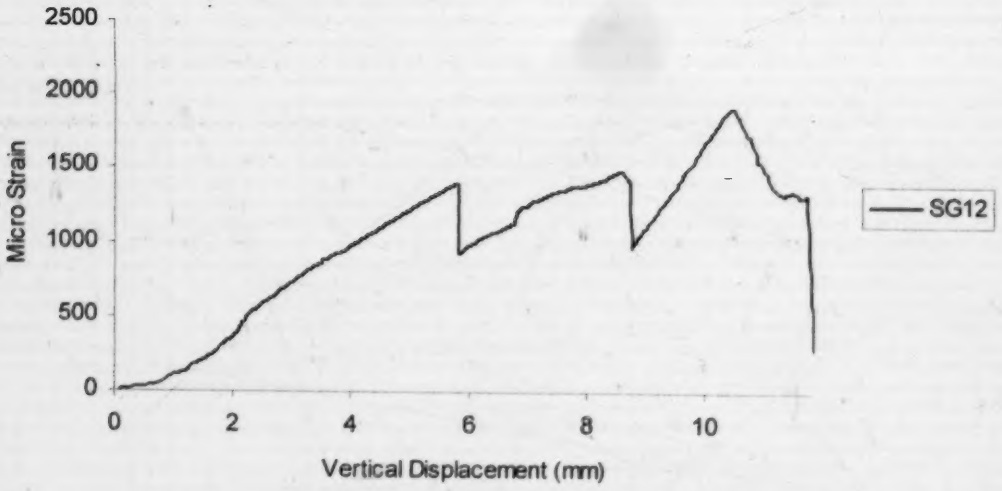

Figure (3.19) – Strain at SG12

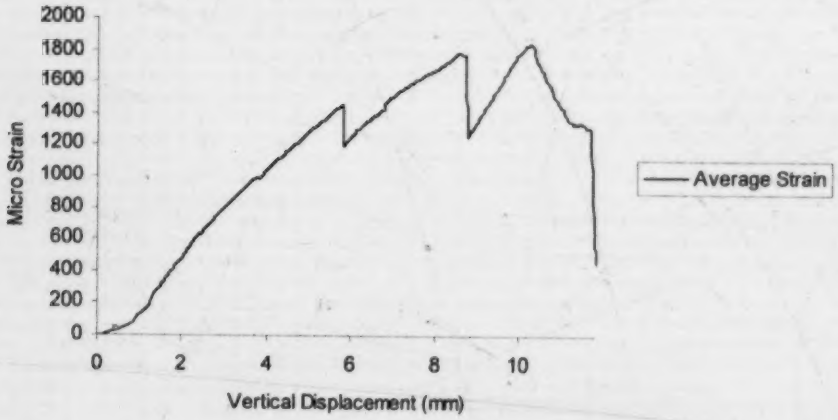

Figure (3.20) – Average Strain at the Beginning of the Bend

4. Analysis and Bond Model Development

4.1. Introduction

There are different methods of analysis for structural applications. These methods can be categorized as Newton-Raphson methods, implicit dynamic methods and explicit dynamic approach. Newton-Raphson methods are iterative analyses that work with nonlinear stiffness matrices. This category has a poor performance in reinforced concrete analysis. That is because of convergence problems and they are extremely time-consuming. The implicit dynamic analysis approach uses numerical integration methods such as linear acceleration (Bathe 1996). This kind of approach is not well suited to contact problems in reinforced concrete and similar to the Newton-Raphson algorithm is time consuming. Explicit dynamic analysis is the method of choice for reinforced concrete and contact problems because of the inherent discontinuous nature of these problems. This approach is powerful because it is not iterative, thus eliminating the convergence problem. This method uses the central difference integration scheme. Because of the obvious advantages, explicit dynamic analysis has been used in this research and will be explained in detail later in this chapter.

Modeling of material properties can be done in four major ways which are elasticity, hypo-elasticity, hyper-elasticity and plasticity. Elasticity is the simplest and the most inaccurate way to model a reinforced concrete structure and is not suitable for research purposes. Hypo-elasticity attempts to relate increments of stresses to increments of strains in a non-linear way. Mathematical implementations of hypo-elasticity were largely unsuccessful. Hyper-elasticity tends to establish a non-linear relationship between total stresses and total strains at each point of time and is decidedly not suitable for inelastic behavior. Plasticity is the most accurate approach for inelastic material modeling. This method assumes the existence of a yield surface and a plastic potential function and relates the increment of stress to the elastic part of the strain increment. When

modified for cyclic loads and load reversals, it is called damaged plasticity. Damaged plasticity approach has been used in this research.

There are two other major methods of modeling concrete material properties. The first method is discrete crack modelling. In this method when the tensile stress at a node of the concrete elements reaches the tensile strength of concrete, that node separates from surrounding elements and different node numbers are defined at the same location for adjacent elements. This method works best with a very fine mesh so the crack propagation path can be correctly simulated (Hofstetter, 1995). The second method is smeared crack modeling which maintains complete displacement continuity at nodes. However, when the principal stress at an integration point exceeds the tensile strength of concrete the strength of concrete in that direction is considered zero. Therefore, smeared crack model is like an orthotropic material model. In other words, in smeared crack model initial material properties of concrete are the same in both principal directions. However, with initiation of cracks material properties in these two directions deviate from each other (Hofstetter, 1995).

In comparison, damaged plasticity is the most accurate concrete model since it accounts for nonlinear compression and tension behavior of material in a tri-axial state of stress using yield and plastic potential functions. This method is explained in more detail in the following sections.

Modeling bond can be done in implicit and explicit ways. In the first method full connectivity between concrete and bar elements is implemented and bond is considered indirectly by a tension stiffening phenomenon. In explicit modeling of bond however, bond is considered directly by bond elements or surface interactions. The latter is used in this research and will be discussed in detail in this chapter.

4.2. Finite Element Mesh

The concrete is modeled with eight node three dimensional brick elements with eight nodes on each element along with wedge, triangular prism elements with six nodes per element. The main steel tension reinforcement is modeled with three dimensional brick elements while stirrups and compression bars are modeled with truss elements. All these elements have three translational degrees of freedom at each node. Shear and compression truss reinforcement are embedded into the concrete elements. In the embedment method, the nodes of an embedded steel element are considered parts of the host concrete elements. Thus, the degrees of freedom at the nodes of embedded elements can be found by interpolation of degrees of freedom of the nodes in the corresponding host elements using finite element shape functions (Hibbit et al, 2005). This type of interpolation produces the necessary constraint equations needed to eliminate the embedded element degrees of freedom and account for their influence on the concrete element degrees of freedom.

The end plate is modeled with flat rigid elements and the load is applied through one node on this rigid surface using displacement control conditions.

Because the specimen is symmetric there is no need to model all of it. Therefore, only one fourth of the specimen is modeled and symmetry is taken into account by means of appropriate boundary conditions on the planes of symmetry. Various types of meshes were tried and the one in figure (4.1) was found to be efficient.

One special problem with the brick elements is hourglassing. Hourglassing is a problem with first-order, reduced-integration elements including three dimensional brick elements. Hourglassing is a spurious deformation mode associated with zero energy levels (Belytschko, 1984). The wedge elements at the top of the model are used in the shown arrangement to prevent hourglassing formation as much as possible. This has been done along with enhanced hourglassing control over the whole model to make sure there will be little

spurious energy modes produced in the analysis.

The cross section of the tension reinforcement is modeled by an equivalent rectangular cross section that gives the same cross section area and moment of inertia as the actual circular cross section. This simplifies the mesh generation without sacrificing much precision. The equivalent cross section dimensions are shown in figure (4.2).

To allow modeling of the bond in surface behavior, tension bars are not connected to the concrete elements by nodal degrees of freedom, rather the normal interaction is modeled by a contact algorithm. The contact algorithm is based on a numerical concept. First the contact surfaces on the concrete and the corresponding surfaces on the bars are defined with separate nodes. As the surfaces tend to move relative to each other, the algorithm calculates compressive forces that tend to separate the nodes when surface penetration is detected.

To model tangential "bond" interaction the corresponding nodes, which are coincident at the beginning of analysis are linked with "Cartesian connector elements". A Cartesian connector element provides a connection between two nodes that allows definition of independent behavior in three local Cartesian directions. In this analysis these elements act only along the bar direction. In other words, the "x" axis in figure (4.3) is defined along the bar while "y" and "z" axes are perpendicular to "x" and form a right handed coordinate system. However, "y" and "z" axes are not used here. The relative movement between coincident nodes connected by Cartesian connector elements is controlled by a bond-slip relationship that will be discussed later in detail.

Briefly, the connector elements act like springs and for different values of slippage produce corresponding resisting forces on the connected nodes. The forces generated by the Cartesian elements are computed using the bond stresses from bond slip diagrams and tributary areas associated with nodes of concrete-steel interface. Each node is assigned a tributary area equal to one fourth of the

lateral surface extending halfway through lengths of adjacent elements. Since the perimeters of real and equivalent cross-sections are not equal the tributary area associated with each node corresponds to the real cross-section perimeter.

4.3. Analysis Procedure

The analysis is quasi static in an explicit dynamic form. It forms a class of time domain step by step integration. (Benson, 1992; Hibbit et al, 2005). The method of time integration is based on a central difference scheme. The equation of dynamic equilibrium is written for the current configuration (Bathe, 1996; Hibbit et al, 2005). The central difference method assumes that velocities at times $t-\frac{\Delta t}{2}$ and $t+\frac{\Delta t}{2}$ equal to slopes of displacement-time relationship from time $t-\Delta t$ to t and from time t to $t+\Delta t$ respectively. The velocity at time t is calculated as the average of the mid increment velocities and the same velocities are used to compute the current acceleration as the slope of velocity-time diagram. (Hibbit et al, 2005). Equations governing the central difference method are obtained as follows (Bathe, 1996):

$$\dot{q}_{t-\frac{\Delta t}{2}} = \frac{q_t - q_{t-\Delta t}}{\Delta t} \tag{4.1a}$$

$$\dot{q}_{t+\frac{\Delta t}{2}} = \frac{q_{t+\Delta t} - q_t}{\Delta t} \tag{4.1b}$$

$$\dot{q}_t = \frac{\dot{q}_{t+\frac{\Delta t}{2}} + \dot{q}_{t-\frac{\Delta t}{2}}}{2} \tag{4.1c}$$

$$\dot{q}_t = \frac{q_{t+\Delta t} - q_{t-\Delta t}}{2\Delta t} \tag{4.1d}$$

$$\ddot{q}_t = \frac{\dot{q}_{t+\frac{\Delta t}{2}} - \dot{q}_{t-\frac{\Delta t}{2}}}{\Delta t} \tag{4.1f}$$

$$\ddot{q}_t = \frac{q_{t+\Delta t} - 2q_t + q_{t-\Delta t}}{\Delta t^2} \tag{4.1g}$$

Where, q, $\dot{q}$, $\ddot{q}$ and t denote displacement, velocity, acceleration and time respectively. Considering the equilibrium for the current configuration, time "t", the following equations are obtained:

$$[M]\{\ddot{q}\}_t + [C]\{\dot{q}\}_t + [K]\{q\}_t = \{f\}_t \tag{4.2a}$$

$$\left[\frac{1}{\Delta t^2}[M] + \frac{1}{2\Delta t}[C]\right]\{q\}_{t+\Delta t} = \{f\}_t - \left[[K] - \frac{2}{\Delta t^2}[M]\right]\{q\}_t - \left[\frac{1}{\Delta t^2}[M] - \frac{1}{2\Delta t}[C]\right]\{q\}_{t-\Delta t} \tag{4.2b}$$

$$[\bar{M}]\{q\}_{t+\Delta t} = \{f\}_t - [\bar{K}]\{q\}_t - [\bar{K}]''\{q\}_{t-\Delta t} \tag{4.2c}$$

Where, $[M]$, $[C]$, $[K]$ and $\{f\}$ represent the mass matrix, damping matrix, stiffness matrix and external force vector respectively.

The central difference method is conditionally stable with respect to the time increment. The critical time increment is the smallest natural vibration period of the structure divided by π (Bathe, 1996). This relationship can be shown in the following equation:

$$T_{cr} = \frac{T_{\min}}{\pi} \tag{4.3}$$

Where, T_{cr} and $T_{\min}$ show the critical time increment and the smallest natural period of the structure respectively. An acceptable time increment can be approximated as the ratio of the smallest element dimension to the sound wave velocity defined as the square root of the ratio of the modulus of elasticity to the medium density, (Benson, 1992). This concept is shown in the following equations:

$$\upsilon = \sqrt{\frac{E}{\rho}} \tag{4.4}$$

$$\Delta t = \frac{d}{\upsilon} \tag{4.5}$$

Where, υ, E, ρ, d and Δt denote sound velocity, modulus of elasticity, density of material, smallest element dimension and time increment respectively.

Therefore, the sound wave velocities for steel and concrete media are approximately 5100 m/s and 3290 m/s respectively. Thus, for the same element dimension the required time step for steel is smaller.

To accelerate the analysis, the method of mass scaling has been used. In this method the density of the model is increased by a magnification factor to give a slower sound wave velocity, which results in a larger stable time increment for the same mesh (Hibbit et al, 2005). This will reduce the computing time. In this analysis variable mass scaling method has been used to apply the proper scale to the mass to give a critical time increment of 0.0005 Sec.

To verify the analysis is quasi static a check of kinetic energy level is necessary. In other words, the internal and external energy levels have to be fairly close while the kinetic energy has to be bounded and small, say 10 percent of the internal energy during the whole time of analysis.

4.4. Modeling of Material Properties

In order to perform an accurate analysis, there is a need for a concrete model that is able to account for the real behavior of concrete. According to the literature, modeling of material properties can be done in various ways such as elastic, hypo-elastic, hyper-elastic and plastic. In elastic type of modeling the relationship between stress and strain is usually linear and total strains are related to total stresses by a constitutive matrix. If the relationship between total stresses and total strains is nonlinear this kind of modeling is called hyper-elastic. However, if increments of strains are related to increments of stresses the material model is of hypo-elastic type.

In plastic analysis a yield surface is defined along with a plastic potential function. Negative values of yield function indicate elastic behavior while positive values indicate plastic behavior. The increment of plastic strain is assumed proportional to the gradient of a plastic potential function of stress. The

coefficient of proportionality is a function of both yield and plastic potential functions. This relation is called the flow rule. If the yield function and the plastic potential function are the same the flow rule is called "associated", otherwise it is a non-associated flow rule.

In modeling the steel material the yield function and plastic potential function are the same and defined by the well known von-Mises relationship.

In concrete damaged plasticity, used here, the yield function is Lubliner and the plastic potential function is Drucker-Prager (Drucker, 1951 and Hibbit et al., 2005). Damaged plasticity accounts for both compression hardening and tension softening. This method has been developed by Hillerborg et al. (1976), Lubliner et al. (1989) and Lee et al. (1998).

Damaged plasticity assumes that there are two main reasons for concrete failure. They are compression crushing and tension cracking. Uniaxial tension and compression behavior are the main input values of analysis and have to be defined before analysis is carried out. The corresponding stress-strain curves are used to define compressive and tensile behavior of concrete in terms of Cauchy stresses and logarithmic strains. Accordingly, the regular stress-strain values have to be adjusted to reflect this. However, this conversion only makes a real difference when strains are of very large values. Damage factor is used for cyclic loading and is not used in this research. Therefore, in this case damaged plasticity turns into concrete plasticity. In concrete plasticity stress invariants are used to define the plastic potential and yield functions. The constitutive relationship in absence of damage parameter depends on elastic strain increments and elastic material matrix only. Elastic strain increments are computed by subtraction of plastic strain increments from the strain increments. Plastic potential relationship by Drucker-Prager is a function in terms of hydrostatic pressure, Mises equivalent stress and a dilation angle which is normally taken as 15 degrees for concrete.

For the compression model the well-known Saenz stress-strain curve has been used to define the effective stress effective plastic strain relation (Chen, 1982). This model has been widely used in finite element analyses and has rendered good results. This model is shown in Figure (4.4). In this model, the ascending branch follows a curve described as:

$$\sigma = \frac{E_0 \varepsilon}{1 + \left[\frac{E_0}{E_s} - 2\right]\left(\varepsilon/\varepsilon_c\right) + \left(\varepsilon/\varepsilon_c\right)^2} \tag{4.6}$$

Where, E_0 is the initial modulus of elasticity, E_s is the secant modulus of elasticity corresponding to peak stress and ε_c is the strain corresponding to the peak stress. The descending branch is a straight line passing through two points (f_c', ε_c) and $(0.2 f_c', 4\varepsilon_u)$.

Concrete exhibits two phenomena associated with cracking in tension. The first is tension softening which is associated with gradual growth of the crack width in the so called "crack process zone" (Hillerborg, 1976). This is accounted for using the tension-displacement relation shown in figure (4.5) and described by the following curve proposed by Li et al (2002):

$$\sigma = f_t \left\{ 1 - \exp\left[-\left(\frac{0.05/w}{w_f} \right)^{1.3} \right] \right\} \tag{4.7}$$

Where, w and w_f are the crack width and the final crack width respectively and f_t is the tensile strength of concrete. This equation is based on the energy of fracture approach of Hillerborg (1976).

The second phenomenon is tension stiffening resulting from gradual loss of bond between concrete and reinforcement over the distance between cracks. In much of the literature this is described using a phenomenological average approach. It is more suited to distributed reinforcement such as in plates and walls. It is not suited for single bar representation. In this work, bond behavior is modeled

explicitly as shown next.

4.5. Modeling of Bond

Bond is composed of three components: chemical adhesion between concrete and steel surfaces, friction between concrete and reinforcement and bearing interaction of concrete keys against bar lugs. Before any failure, slippage is basically induced by local crushing and deformation of the concrete in the proximity of steel ribs. Bond failure is either caused by shearing of the concrete sections in front of the lugs of the reinforcing bar or by splitting of concrete adjacent to the bar. Splitting of concrete is a much more sudden type of failure than shearing of concrete sections.

The proposed model is based on a number of concepts:

1- The ultimate bond capacity is a function of the normal pressure on the bond surface in addition to all other parameters such as surface roughness, cohesion, etc. This capacity is obtained as a modification of the unconfined bond capacity.

2- The bond-slip relation in the absence of passive confinement such as the one provided by stirrups is a tension softening relation. Conversely, in the presence of heavy stirrups the relation is bilinear in which bond increases with slip then it remains constant. In between a rational transition of behavior can be defined.

This approach will be constituted similar to orthotropic concrete relationship.

4.5.1. Unconfined Ultimate Bond Capacity

The bond capacity for unconfined concrete can be obtained by either Tepfers' (1979) or Eligehausen's (1983) relationships which are shown in equations (4.8) and (4.9) respectively. Tepfers' relationships are based on theory of plasticity while Eligehausen's equation is empirical. Tepfers' relationships are accurate for small to medium ratios of concrete cover to bar diameter and are close to

Eligehausen's. However, for cover ratios more than 2.0 it is preferred to use Eligehausen's equation since Tepfers' approach results in capacities larger than those obtained from tests by previous researchers.

$$\tau(0)=\begin{cases}\dfrac{2C}{D}f_t & \dfrac{C}{D}\le 1\\ \left(\dfrac{C+D/2}{1.664D}+\dfrac{2C}{D}\right)\dfrac{f_t}{2} & \dfrac{C}{D}\ge 2\\ \textit{Interpolation of the above for ratios of } 1 \textit{ and } 2 & 1<\dfrac{C}{D}<2\end{cases} \qquad (4.8)$$

$$\tau(0)=1.5 f_t\sqrt{C/D} \qquad (4.9)$$

Where, C is the smallest concrete cover, D is the bar diameter and f_t is the tensile strength of concrete. Thus, the ratio of cover to bar diameter is an important factor in unconfined concrete bond capacity.

4.5.2. Confined Bond Capacity

Bond-slip relationship is accounted for on a node by node basis. In other words, depending on the normal pressure σ_N in different locations, different values of bond capacities can be assigned. The normal pressure in any direction provides confinement of concrete in that direction and confinement helps increase the bond capacity. It is expected that in different locations there are different normal pressures and consequently different bond capacities that have to be assigned to different places on the bars. One location may be subject to different levels of confinement on the exterior and interior sides as it is the case in the bend region. There is high normal pressure on the interior side of the bend while there is little on the exterior side. Therefore, these two sides experience different bond behaviors. Figure (4.6) shows the ratio of confined bond capacity, τ_{max} to unconfined bond capacity $\tau(0)$ as a function of the ratio of the normal pressure σ_N to concrete strength f_c'.

Bond capacity curves in figure (4.6) except the present one are created based on other researchers experiments, Malvar (1992), Eligehausen (1983), Untrauer (1968). The present bond capacity curve has been obtained by a large number of trials beginning from Eligehausen's curve and ending in the present curve in figure (4.6). In other words, different bond-confinement curves have been associated to the model and the present curve in figure (4.6) is the final result of that procedure. This curve leads to the closest results to the test described in chapter 3. It is also in good agreement with both Malver and Untrauer test results. It is a third order polynomial. The confined bond capacity in this research follows the curve shown in Figure (4.6). The relationship for this curve is equation (4.10).

$$\tau_{max} = \tau(0)\left(0.4086n^3 - 2.4855n^2 + 3.4769n + 1\right) \quad , \quad n = \frac{\sigma_N}{f_c'} \tag{4.10}$$

Where, τ_{max} is the confined bond capacity and $\tau(0)$ is obtained from equation (4.8). It is also worthwhile to note that figure (4.6) makes a comparison of the present curve and the ones obtained from previous researchers test results. The reason Eligehausen et al (1983) results are somewhat lower is that they applied compression on concrete tied with high ratios of stirrups which renders the concrete already confined. It is clear that applying compression on already confined concrete has less bond increasing effect than confining the initially unconfined concrete.

However, bond behavior is not a function of normal compression only. It is dependent on slippage too. The bond-slip relationship proposed in this research is given in equations (4.11a) to (4.11d). The procedure to find this equation is explained later. This model is initially developed to analyze the test described in chapter 3. However, it will be used to analyze other specimens from the literature in later chapters.

$$\tau_b = f(S,\sigma_N) = \begin{cases} 250S & S \le S_m \\ \tau_{\max} & S_m \le S \le S_{m2} \\ \tau_{\max} + \dfrac{\tau_{\max}}{S_{m2} - S_u}(S - S_{m2}) & S_{m2} \le S \le S_u \end{cases} \quad (4.11a)$$

Where,

$$S_m = \frac{\tau_{\max}}{250} \quad (4.11b)$$

$$S_{m2} = 1.468(S_m - 0.018) + 0.018 \quad (4.11c)$$

$$S_u = 21.11(S_m - 0.018) + 0.018 \quad (4.11d)$$

Here, τ_b is the current bond stress value and S, S_m, S_{m2} and S_u represent slip in millimeters, slip value beyond which bond does not increase, slip value at initiation of bond deterioration and the maximum slip value beyond which bond is considered zero respectively. A schematic illustration for equation (4.11a) is shown in Figure (4.7). In this figure $\tau_{\max}$ is the confined bond capacity which is a function of unconfined bond capacity, normal stress and concrete strength as described by equation (4.10).

The proposed bond-slip model accounts for slip and confinement as well as the ratio of cover to diameter. Equations (4.11) are illustrated in Figure (4.8).

The concrete with stirrups is treated differently as it does not have an abrupt loss of bond due to splitting. Therefore, there is no descending branch for this type of confinement. To model the behavior of concrete confined by stirrups equation (4.12) has been obtained using the results of tests by Eligehausen et al (1983). However, the descending branch for confined concrete is approximated as flat. The reason for this will be presented in chapter 5.

$$\tau_{\max} = 2.4\tau(0)\left(2.98n^3 - 3.75n^2 + 1.61n + 1\right) \quad , n = \frac{\sigma_N}{f_c'} \quad (4.12)$$

The bond capacity for concrete confined with stirrups is shown in Figure (4.9).

4.5.3. Discussion to Summarize the Rationale of the Research

The concept of the proposed model accounts for different concrete strengths and cover to bar diameter ratios using the equation for unconfined bond capacity. The maximum bond capacity is then considered a function of the normal stress as well as the unconfined bond capacity. According to previous research the slope of the ascending branch of the bond-slip relationship changes very little with increased compression. In other words, in a tri-linear model, like the proposed one, the stiffness of the ascending branch, is taken to be constant for all levels of confinement as proposed in equations (4.11). The actual value of initial slope used here which is $250\ N/mm^3$ is within the range of previous research results ranging from approximately $838\ N/mm^3$ by Nilson (1968) to $68\ N/mm^3$ by Durate (Brant et al., 1986). In addition, this slope results in a capacity and a load-deflection ascending branch that are close to the test results as will be discussed later.

Based on the results from tests in the literature, the slope of descending branch in the bond-slip diagram becomes less steep with increased levels of confinement and descending branches for fairly high levels of confinement tend to become almost parallel (Eligehausen et al., 1983 and Malvar, 1992). This is reflected in equations (4.11). Nevertheless, the descending branch of the bond-slip diagram has a direct effect on the descending branch of the load-deflection diagram of the structure. Hence, it has been chosen in a way to render a close approximation of the behavior of test specimen.

4.5.4. Development/Test of the Model

In order to test the model, the bond parameters were applied in an iterative procedure. First, to find the slope of the ascending branch, different linear bond-slip relationships were tested to find the slope that gives the closest behavior to the ascending branch of load deflection diagram. Hence, the $250\ N/mm^3$ value is used in equation (4.11).

Next it was necessary to find a bond-confinement curve and a descending branch

that render correct results. Therefore, an arbitrary bond-confinement and an arbitrary descending curve for bond-slip diagram were assumed. Based on the assumed bond-confinement curve different bond capacities were assigned to different locations of steel-concrete interface and a preliminary analysis was carried out. Compared to the previous trial analysis, the state of normal stress changed at different locations and hence new bond capacities were assigned to different locations for reanalysis. This process was repeated untill little difference was observed between capacities from output and input. However, having close input and output curves does not necessarily mean the correct bond-confinement relationship was achieved. The load bearing capacities of the model and the test had to be compared. If they were not close the bond-confinement curve was adjusted and the abovementioned procedure was repeated.

After a proper bond-confinement diagram was found, comparison was made to decide if the descending branch of load-deflection diagram was close to test. If it was not the case, the descending branch for bond-slip curve was adjusted for reanalysis and the iterative procedure was repeated. Equations (4.10) and (4.11) are the results of this procedure presenting bond-confinement and bond-slip respectively.

Figure (4.10) shows a 2D view of a typical tension bar and the corresponding elements and how the nodes are numbered. These numbers are used in captions for Figures (4.11) to (4.25). In Figures (4.11) to (4.25) diagrams for bond stress versus compressive stress are depicted. Figures (4.11) to (4.16) are for the bend region. Figures (4.17) to (4.25) show the bond-compression curves for some nodes in the hook region. The output bond-slip diagrams for some of the nodes are presented in Figures (4.26) to (4.29).

Capacities from output are obtained using bond-confinement diagrams such as those shown in Figures (4.11) to (4.25). This is done in conjunction with output bond-slip diagrams in Figures (4.26) to (4.29) to check if a node has already

reached its peak bond stress. In other words, a check of both output bond-confinement and bond-slip diagram is needed to make it clear if the peak bond stress in the bond-confinement diagram is the bond capacity. This check is shown in figure (4.11) where a schematic bond-slip and bond confinement for a node are illustrated. For clarity, in figure (4.11) different bond values on the bond confinement curve and their corresponding points on the bond-slip diagram are connected with horizontal lines. The locations corresponding to the bond capacity on the bond-confinement and bond-slip diagram in figure (4.11) are marked with crosses. When the bond slip curve starts to move into a descending branch at a specific bond value that value is the bond capacity. Otherwise, it is not clear whether or not a bond value is the real capacity since it maybe possible that the capacity is a higher value, which was never reached due to low slippage values. For the sake of brevity, only some diagrams from the last analysis trial are presented.

This approach has been applied to many input curves to obtain the one that gives the best results. As a result the input curve in Figure (4.6) and equation (4.10) has been proven the most efficient since it results in a behavior close to test and is in agreement with the literature and the corresponding output curve does not deviate much from it as it has an R^2 measurement of 0.97. Comparison between output and input curves for the bond capacity is made in Figure (4.30). This Figure shows these two diagrams are fairly close to give a good approximation of results and stop the iteration. The output curve has been obtained from diagrams of the type shown in Figures (4.11) to (4.25).

The input curve in Figure (4.6) determines what bond capacities are given to ABAQUS and the output curve has been obtained using bond-confinement output graphs some of which are presented in Figures (4.11) to (4.25).

Figure (4.26) shows the output bond-slip curves for the bend region. Figure (4.27) shows the bond-slip relationship from output for the straight region which is tied.

Figure (4.28) shows the bond-slip curves for nodes on the left hand side of the hook region. Figure (4.29) illustrates bond-slip output for the nodes on the right hand side of the hook region.

4.6. Comparison with Test

The load versus displacement diagram is presented in Figure (4.31). This Figure depicts the load and deflection of the loading point for the test and analysis. The figure shows that the two diagrams are close to each other as they have almost the same features which are load capacity, ascending branch and descending branch. Comparison of stresses at the beginning of the bend and at the face of the joint is shown in Figures (4.32) and (4.33).

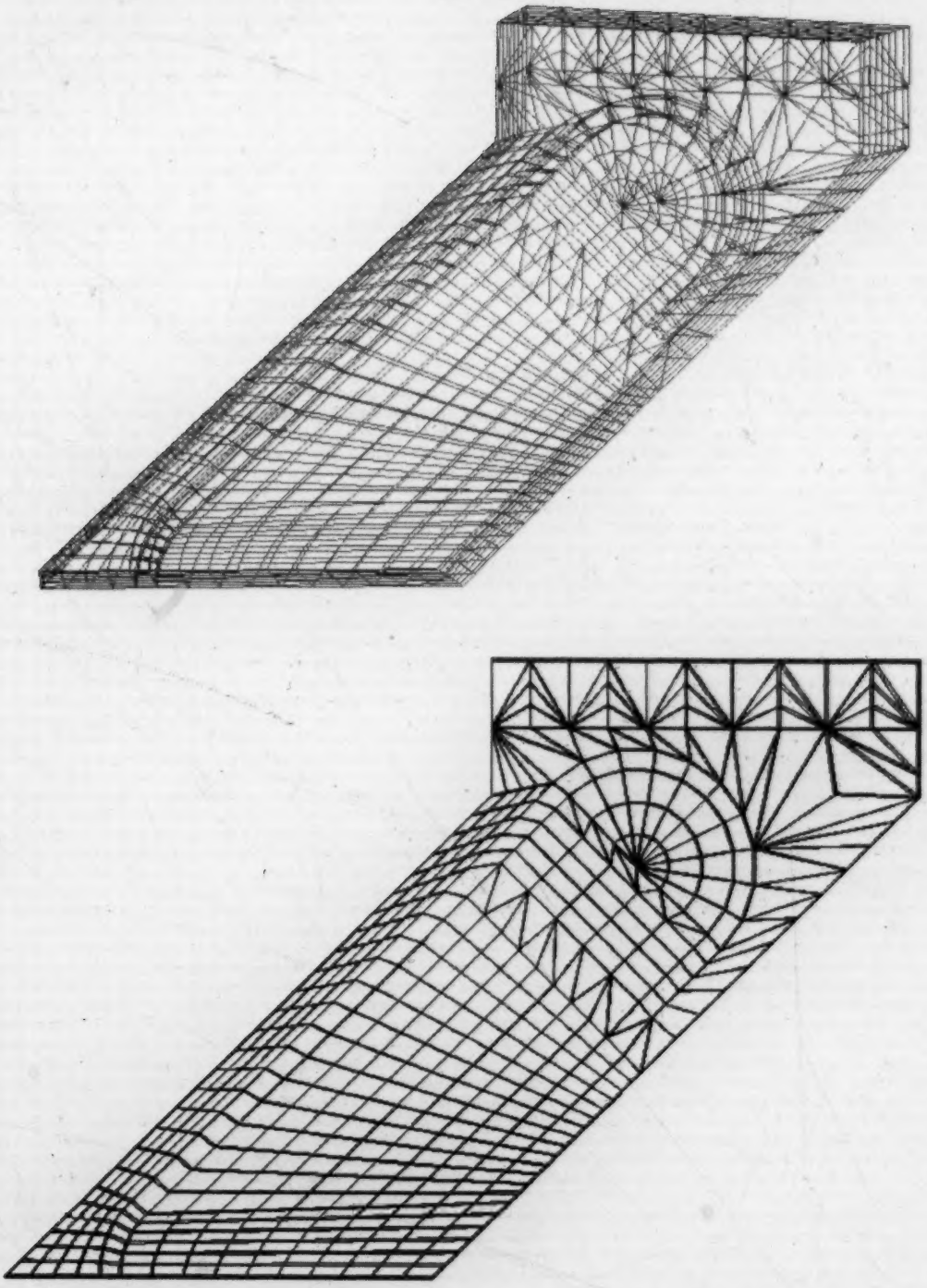

Figure (4.1) – Three and Two Dimensional Views of the Mesh

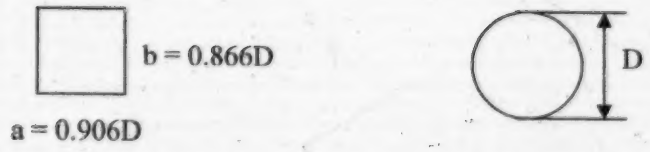

Figure (4.2) – Real Bar Cross Section and Its Equivalent

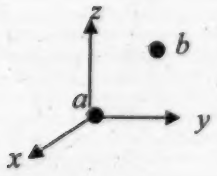

Figure (4.3) - Cartesian Connector Element in Local Coordinates

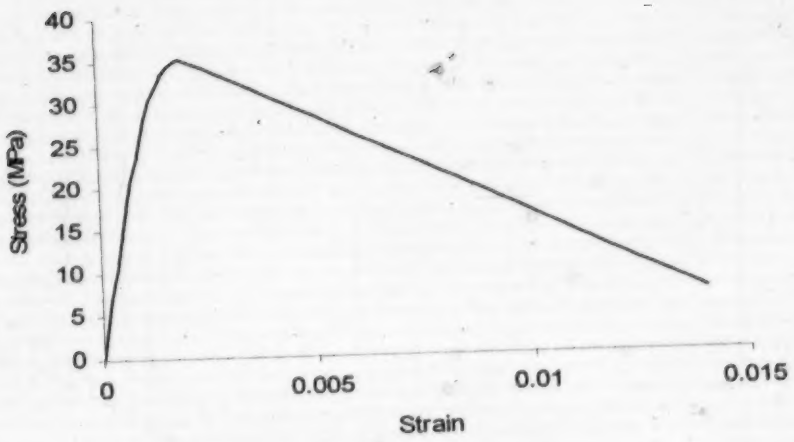

Figure (4.4) – Uniaxial Compression Curve

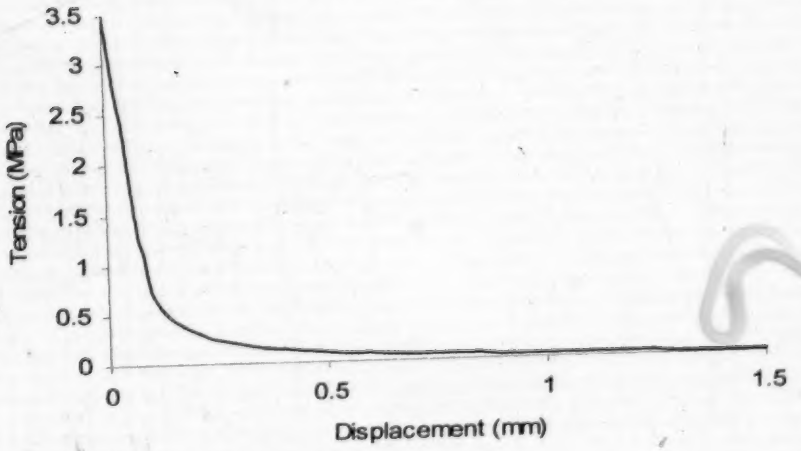

Figure (4.5) – Tension Softening

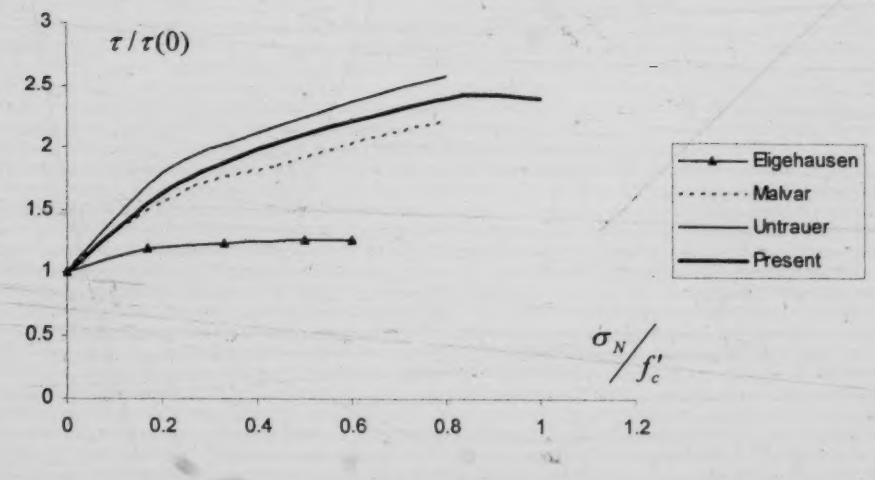

Figure (4.6) – Comparison of the Present Bond Capacity with the Literature.

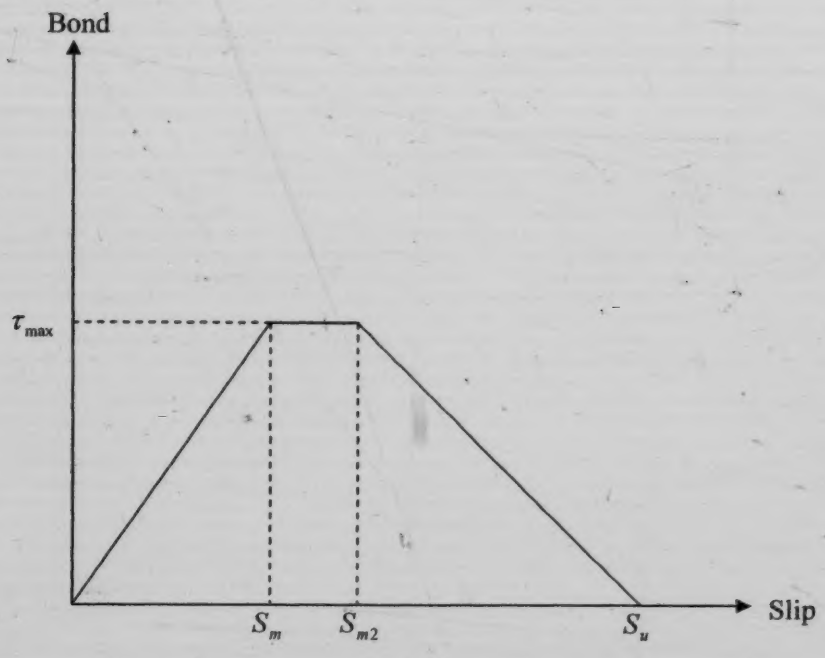

Figure (4.7) – Schematic Bond-Slip Curve

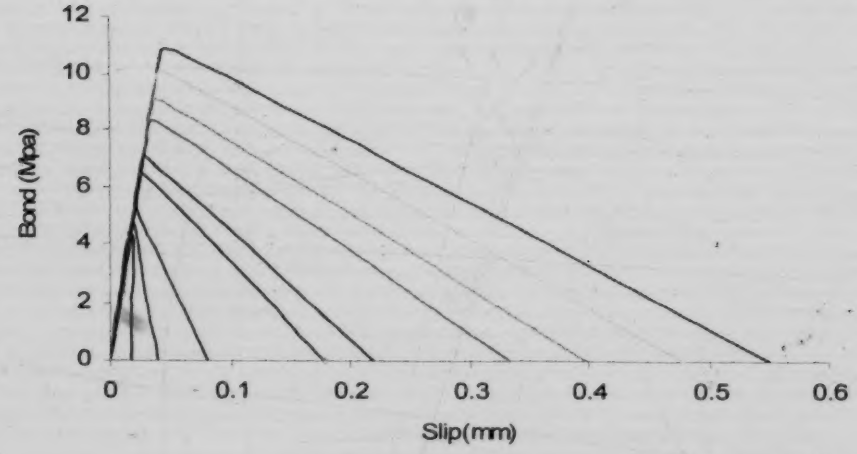

Figure (4.8) – Bond Slip Model for 35MPa Un-tied Concrete

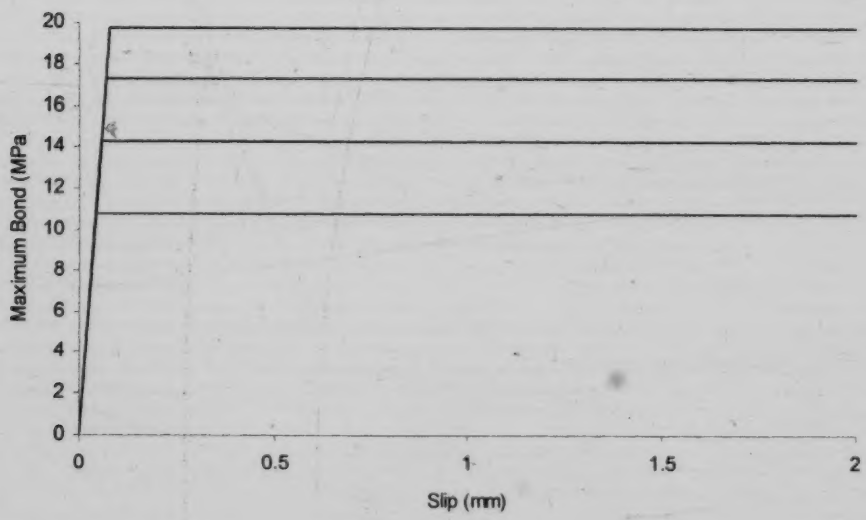

Figure (4.9) – Bond Slip Model for 35MPa Tied Concrete

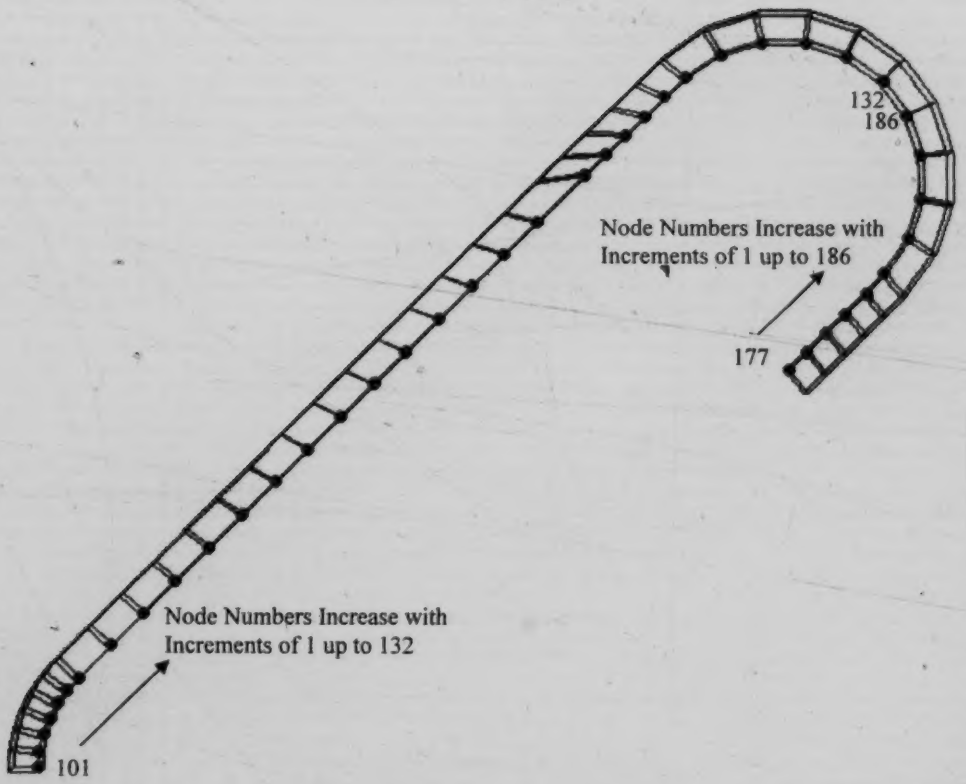

Figure (4.10) – Node Numbering

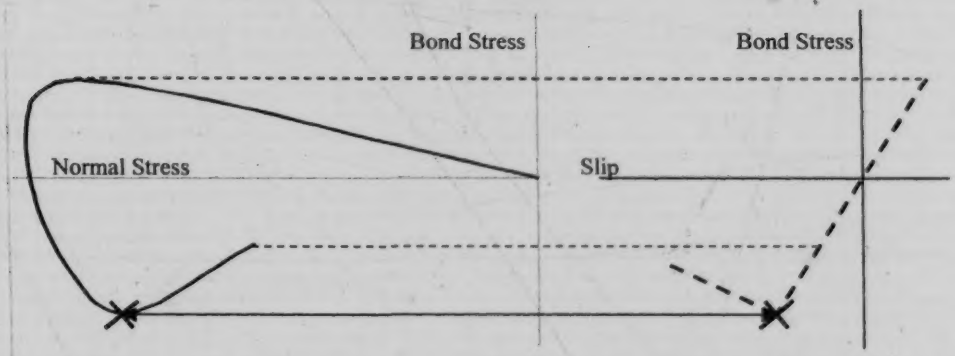

Figure (4.11) – Schematic Nodal Bond-Confinement and Bond-Slip Curves

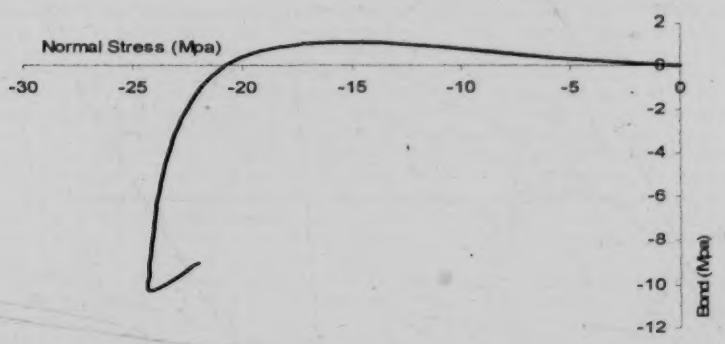

Figure (4.12) – Bond vs. Confinement for Node 103

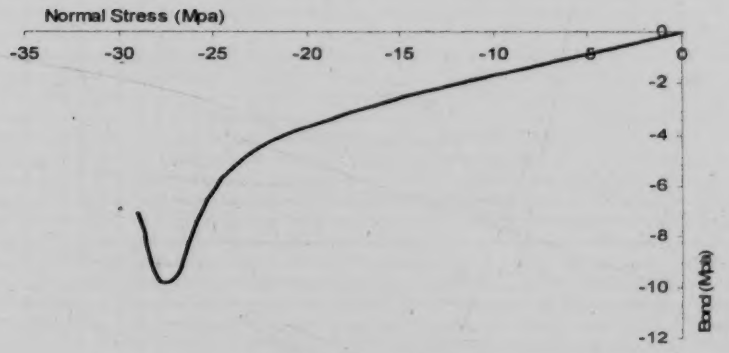

Figure (4.13) – Bond vs. Confinement for Node 104

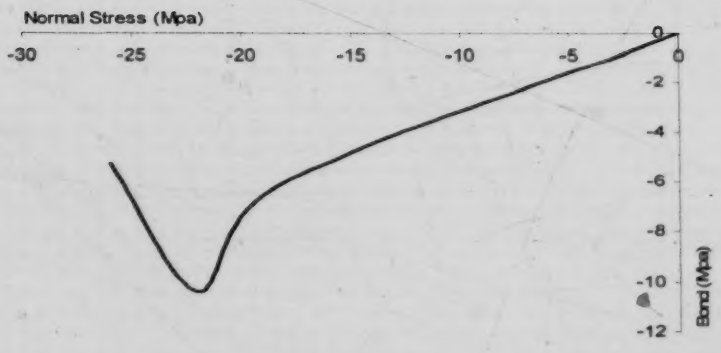

Figure (4.14) – Bond vs. Confinement for Node 105

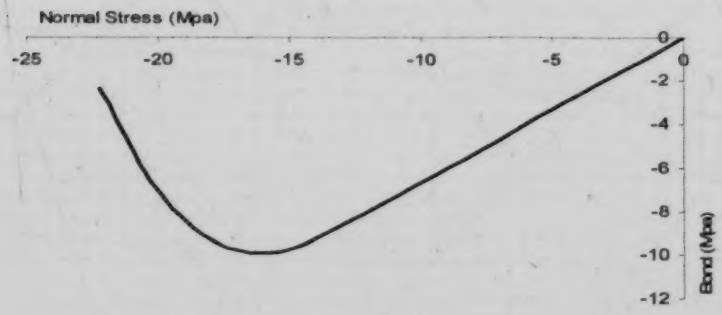

Figure (4.15) – Bond vs. Confinement for Node 106

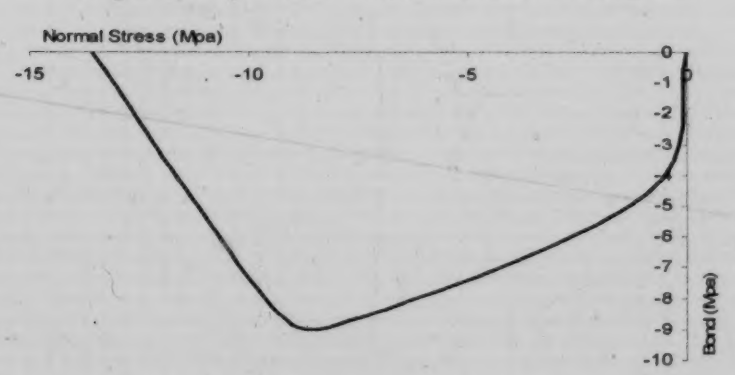

Figure (4.16) – Bond vs. Confinement for Node 107

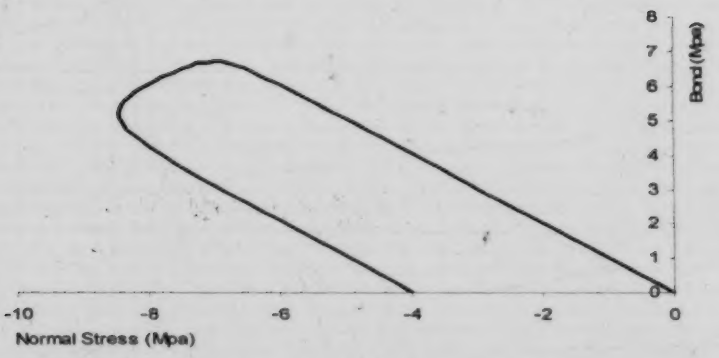

Figure (4.17) – Bond vs. Confinement for Node 128

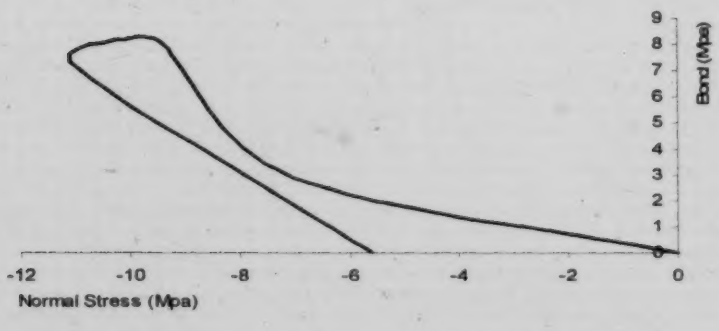

Figure (4.18) – Bond vs. Confinement for Node 129

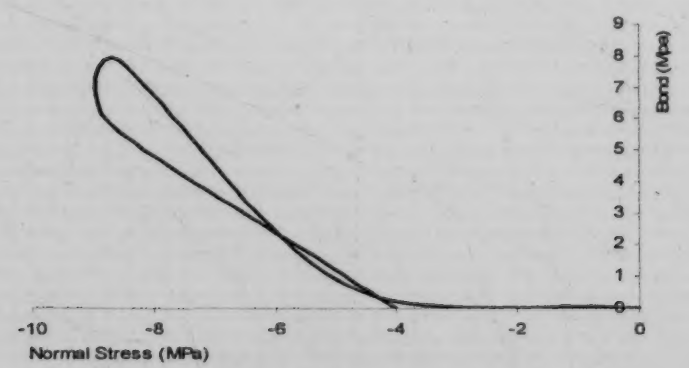

Figure (4.19) – Bond vs. Confinement for Node 130

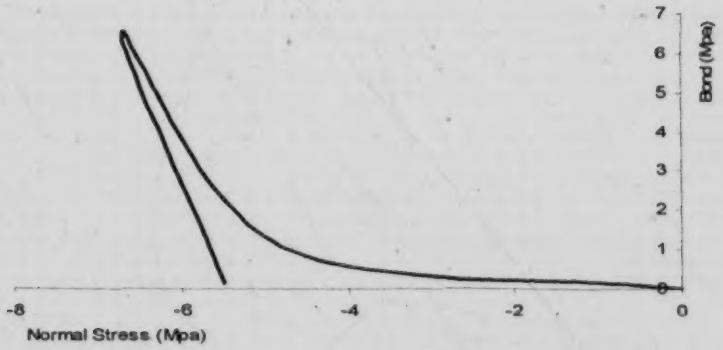

Figure (4.20) – Bond vs. Confinement for Node 131

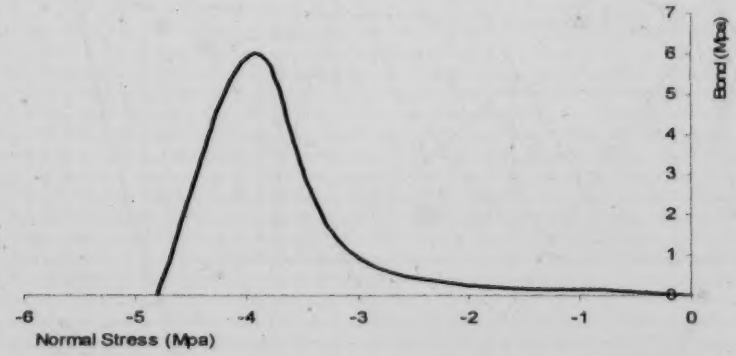

Figure (4.21) – Bond vs. Confinement for Node 132

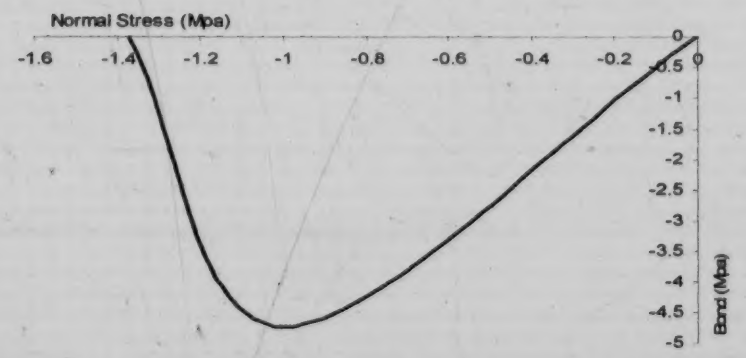

Figure (4.22) – Bond vs. Confinement for Node 183

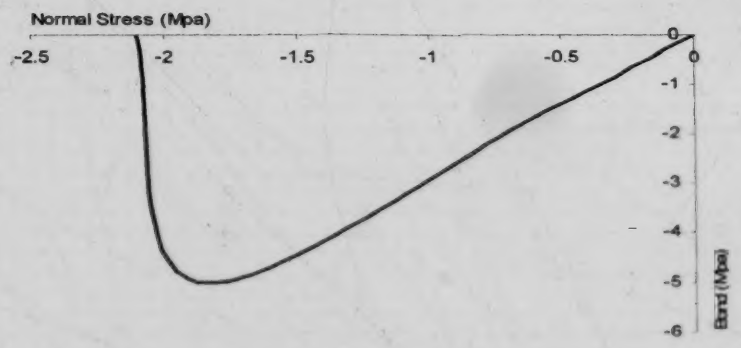

Figure (4.23) – Bond vs. Confinement for Node 184

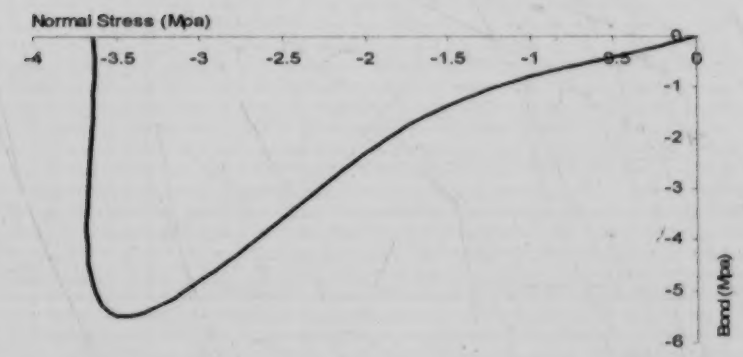

Figure (4.24) – Bond vs. Confinement for Node 185

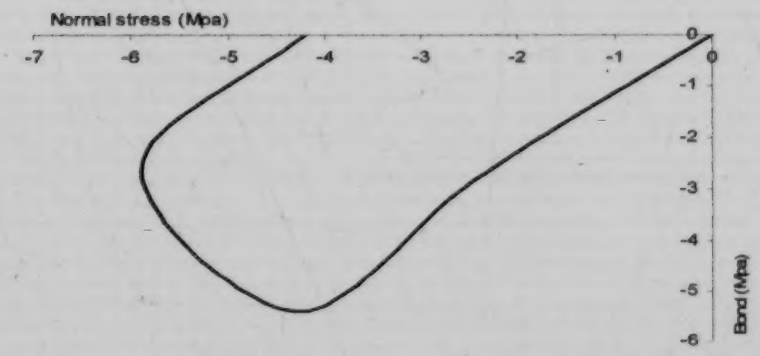

Figure (4.25) – Bond vs. Confinement for Node 186

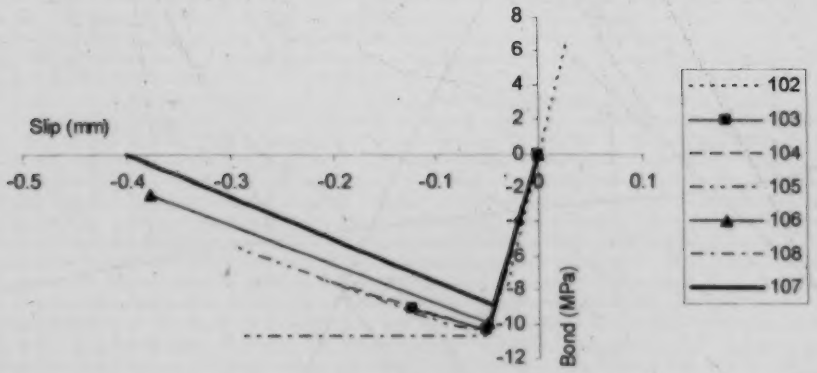

Figure (4.26) – Bond-Slip Relationship for Nodes 102-108

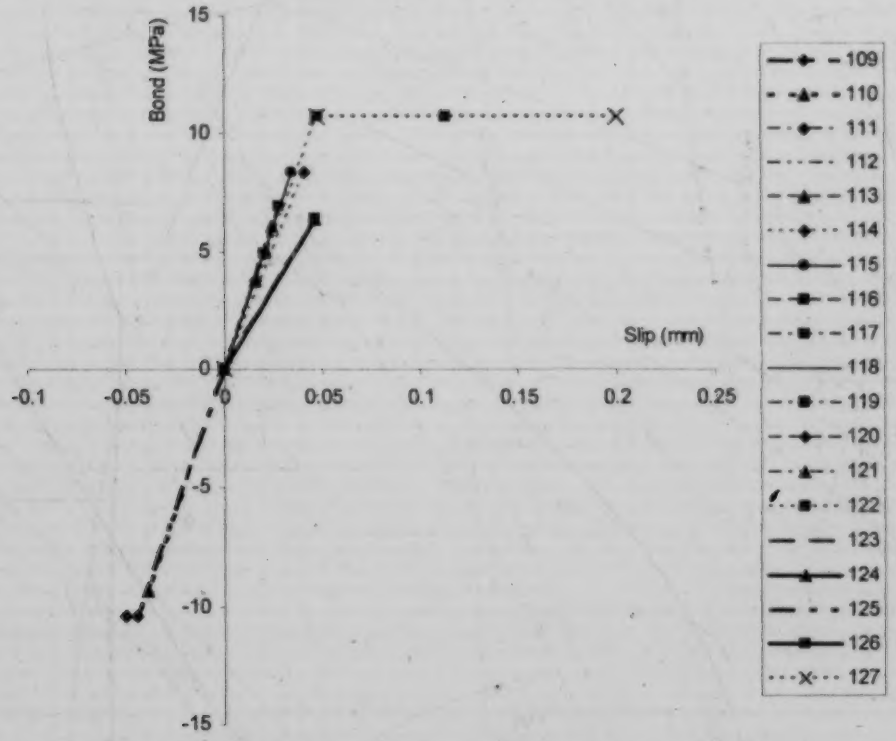

Figure (4.27) – Bond-Slip Relationship for Nodes 109-128

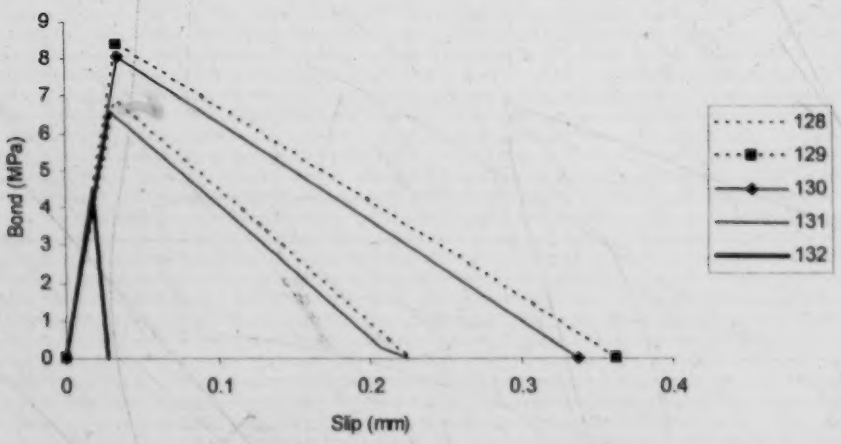

Figure (4.28) – Bond-Slip Relationship for Nodes 128-132

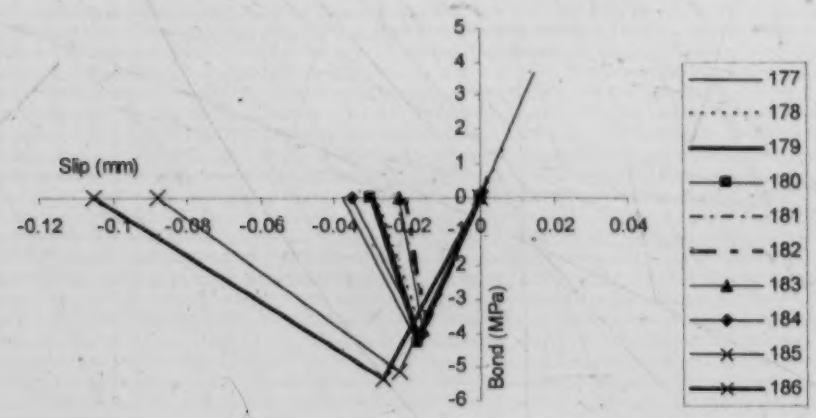

Figure (4.29) – Bond-Slip Relationship for Nodes 177-186

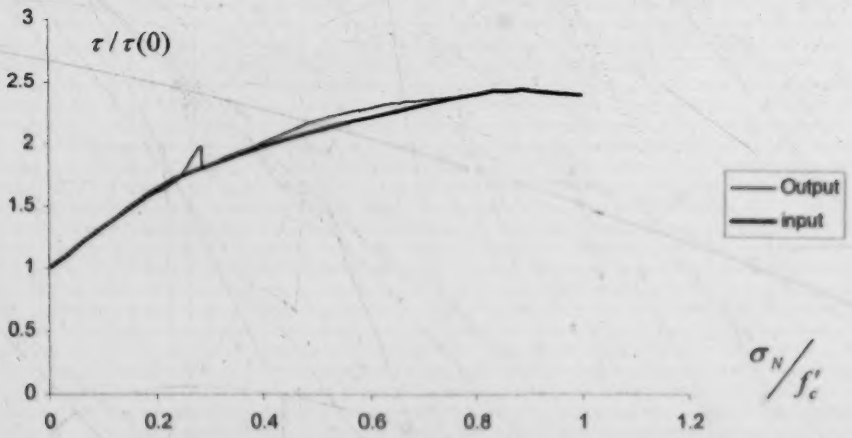

Figure (4.30) – Comparison of Input and Output curves

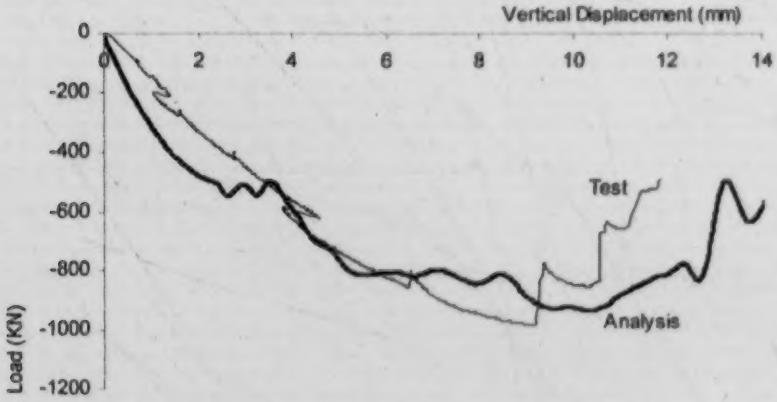

Figure (4.31) – Load-Displacement Diagram

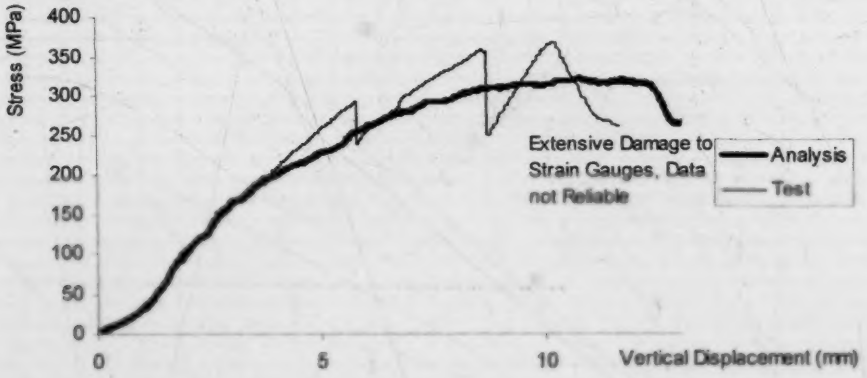

Figure (4.32) – Stresses at the Beginning of the Bend

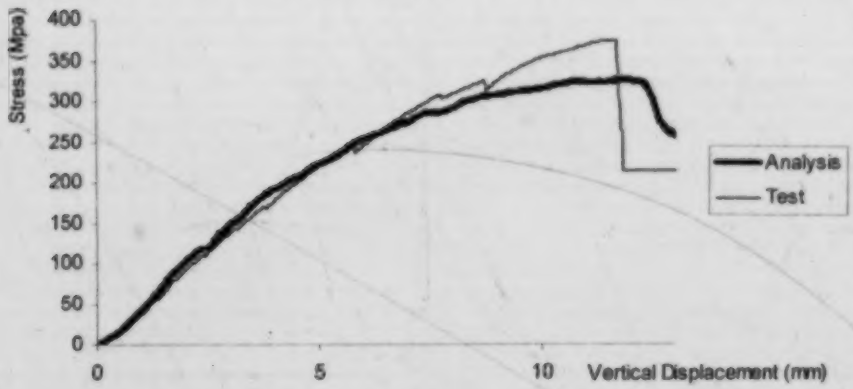

Figure (4.33) – Stresses at the Face of the Joint

5. Interface Constitutive Model

5.1. Introduction

The iterative procedure described in chapter 4 is time consuming. In this chapter a faster and more efficient method for analysis of problems with concrete-steel interface is developed. This is accomplished by introduction of an automatic procedure that applies the bond model, developed in chapter 4, to the interface without running the software several times. In other words, there will be no need to perform a trial and error procedure which is extremely time consuming. Therefore, using an automated method only one analysis will be performed per model. To achieve this purpose, there is a need for a FORTRAN subroutine added to ABAQUS to model this special surface behavior. An algorithm of this program is presented in this chapter. Two forms of this model, total and incremental, are presented. The total form works with total slip and stress values while the incremental method involves increments of these parameters. According to experience the incremental form seems to be working more efficiently with a user subroutine.

5.2. Total Form of the Bond Stress-Slip Response

The total form of this model is the same as the one developed in the preceding chapter but there is a modification with respect to stirrups. Here, a more general case is considered where the amount of lateral reinforcement is not zero but is not sufficient to provide full restriction of splitting either. Therefore, this is a case between the two extremes. With regard to the case without stirrups, there is no restraint against splitting and the slopes of the bond slip diagrams are steep in the descending branch.

For the case of fully confined concrete, the mode of failure is not splitting since concrete fails in shearing of concrete keys against steel surface. In this case there is still a descending branch corresponding to shearing mode of failure but it is far

less steep because the end of descending branch will occur at very large slippages that never happen for ordinary structures.

Therefore, for the type of analysis with small slip values carried out in here the slope of the descending branch for shear mode of failure is approximately zero and hence that descending branch is modeled as a flat branch. In addition, there is no need to model the descending branch for shearing failure because this failure mode is not a bond failure but a concrete failure. It happens by itself even with a flat descending branch. When the concrete at the interface reaches its critical value of shearing deformation it fails even without modeling of shear descending branch. For the case in between the two extremes and wherein confinement is not prefect the slope has to be a function of the splitting and the shearing zero slopes. Thus, there is a need to measure what amount of stirrup is sufficient. The recommendations of code for stirrup reinforcement are not adequate here since they are aimed to address the shear failure problem which is different from splitting. On the other hand, the seismic design deals with the confinement issue exclusively. For this purpose the code references to seismic demand have been used. The amount of lateral reinforcement enough to prevent splitting is considered sufficient if the ratio of $\frac{\rho}{\rho_a}$ which we will call the reinforcement ratio is equal to or more than 1.0. Here ρ_a is obtained from chapter 21 of ACI manual of concrete practice (2005), for spiral and circular hoop reinforcement as follows:

$$\rho_a = 0.12\frac{f'_c}{f_y} \tag{5-1}$$

Here, ρ_a is defined as the volumetric ratio of lateral reinforcement to the concrete core confined by this reinforcement. Since this is a simulation of failure with seismic loads using a more complicated equation for rectangular reinforcement may not help make modeling more accurate and, therefore, only the abovementioned equation is used for all cases.

When the reinforcement ratio $\frac{\rho}{\rho_a}$ equals 1 or more, perfect confinement is assumed and when this ratio is zero, concrete is unconfined. For this reason, with the ratio of 1.0 or more there is zero slope for the descending branch as with the zero ratio steep splitting slope is deemed. In other words, with the reinforcement ratio of zero the ultimate slip is the same as its unconfined value and for the reinforcement ratio of one or more the ultimate slip is a much larger value which will never be reached for structural cases of analysis. This large value only serves to provide a flat slope for the descending branch of the bond-slip relation. This phenomenon resembles the behavior of an exponential function. Thus, equations (5.2) to (5.8) are developed which are modifications to the equations (4.11a) to (4.11d) presented in chapter 4. The coefficient inside the exponent is chosen to give a good approximation of slope at both extremes.

$$\tau_b = f(S,\sigma_N) = \begin{cases} 250S & S \le S_m \\ \tau_{max} & S_m \le S \le S_{m2} \\ \tau_{max} + \dfrac{\tau_{max}}{S_{m2} - S_u}(S - S_{m2}) \exp\left\{-10\left(\dfrac{\rho}{\rho_a}\right)^{1.5}\right\} & S_{m2} \le S \le S_u \end{cases} \tag{5.2}$$

Where,

$$\tau_{max} = 2.4\tau(0)\left[1 - \exp\left\{-10\left(\frac{\rho}{\rho_a}\right)^{1.5}\right\}\right]\left(2.98n^3 - 3.75n^2 + 1.61n + 1\right) + \tau(0)\left(0.4086n^3 - 2.4855n^2 + 3.4769n + 1\right)\exp\left\{-10\left(\frac{\rho}{\rho_a}\right)^{1.5}\right\} \tag{5.3}$$

$$n = \frac{\sigma_N}{f_c'} \tag{5.4}$$

$$S_m = \frac{\tau_{max}}{250} \tag{5.5}$$

$$S_{m2} = 1.468(S_m - 0.018) + 0.018 \tag{5.6}$$

$$S_{u1} = 21.11(S_m - 0.018) + 0.018 \tag{5.7}$$

$$S_u = \frac{S_{u1}}{\exp\left\{-10\left(\frac{\rho}{\rho_a}\right)^{1.5}\right\}} \tag{5.8}$$

Equation (5.3) which defines the confined bond capacity, τ_{max}, has two parts. The first part deals with the effect of normal pressure in the presence of stirrups while the second part is the one developed for unconfined concrete. In fact, equation (5.3) is a combination of equations (4.10) and (4.12) together with inclusion of a new exponential expression related to volumetric lateral reinforcement ratio. In the presence of perfect reinforcement the reinforcement ratio is equal to or more than 1. Therefore, the first exponential expression in equation (5.3) would be extremely close to 1.0 and the second exponential expression would be close to zero. In other words, in presence of perfect confinement only the first part of equation (5.3) would be effective. In contrast, in case of no confinement the first expression in equation (5.3) would be zero and the second expression would be effective. In presence of partial confinement, a combination of first and second expressions of equation (5.3) is effective. Therefore, equation (5.3) can be used in the presence of both forms of confinement, normal pressure and stirrups. Equations (5.4) to (5.7) are explained in chapter 4. The exponential function in denominator of equation (5.8) equals 1.0 and approximately zero in cases of no confinement and perfect confinement respectively. Thus, in presence of no confinement equation (5.8) is the same as equation (4.11d). However, with increased levels of confinement equation (5.8) deviates from equation (4.11d) and becomes asymptotic to a flat line in case of perfect confinement. This phenomenon is illustrated in figure (5.1).

5.3. Incremental Form of Automatic Procedure

This form of modeling has been proven more efficient when used with an incremental surface interaction subroutine in ABAQUS. The necessary equations are derived by partially differentiating the equations in section 5.2 as follows:

$$d\tau = \frac{\partial \tau}{\partial S} dS + \frac{\partial \tau}{\partial n} dn \tag{5.9}$$

$$\frac{\partial \tau}{\partial S} = \begin{cases} 250 & S \le S_m \\ 0 & S_m \le S \le S_{m2} \\ \dfrac{\tau_{max}}{S_{m2} - S_u} \exp\left\{-10\left(\dfrac{\rho}{\rho_a}\right)^{1.5}\right\} & S_{m2} \le S \le S_u \end{cases} \tag{5.10}$$

$$\frac{\partial \tau}{\partial n} = \begin{cases} 0 & S \le S_m \\ \dfrac{d\tau_{max}}{dn} & S_m \le S \le S_{m2} \\ \dfrac{d\tau_{max}}{dn} + \dfrac{\left(d\tau_{max}/dn\right)}{S_{m2} - S_u}(S - S_{m2}) \exp\left\{-10\left(\dfrac{\rho}{\rho_a}\right)^{1.5}\right\} & S_{m2} \le S \le S_u \end{cases} \tag{5.11}$$

Where,

$$\frac{d\tau_{max}}{dn} = 2.4\tau(0)\left[1 - \exp\left\{-10\left(\frac{\rho}{\rho_a}\right)^{1.5}\right\}\right]\left(8.94n^2 - 7.5n + 1.61\right) + \tau(0)\left(1.2258n^2 - 4.971n + 3.4769\right)\exp\left\{-10\left(\frac{\rho}{\rho_a}\right)^{1.5}\right\} \quad ; \quad n = \frac{\sigma_N}{f_c'} \tag{5.12}$$

Equations (5.9) to (5.12) show that increment of bond stress has two parts one corresponding to slip and the other corresponding to normal stress and the total bond is accumulation of these increments as follows:

$$\tau = \int d\tau \tag{5.13}$$

5.4. Algorithm and Flowchart Diagram

Figure (5.3) presents the flowchart for the bond model automatic procedure. In this flowchart, the area associated with each node is specified first. Then, the orientation of the local frame of reference is given using the direction cosines of the tangent to the bar. The normal pressure increments and the increment of slip are computed next. The normal pressure is considered proportional to the amount of penetration by the master surface into the slave surface. Here, the master surface is the steel surface and slave surface is the concrete surface. However, the

reference coordinate system for the interface is different from the one used here and, therefore, a conversion has to be made to obtain the slip and its increment in the local frame of reference. This is accomplished using the direction cosines of the interface reference frame and the local reference system assigned at the beginning. These direction cosines are used to perform a dot product of the components of slip and slip increment on the local coordinate system. Thus, a projection of slip and its increment on the local frame of reference is obtained through this procedure. Figure (5.2) shows the interface and proposed model reference frames. As mentioned in ABAQUS user manual, the interface x direction is defined as the projection of the global x direction on the interface unless the global x direction is normal to the interface (Hibbit et al., 2005). In this case the interface x coordinate is the projection of z axis on the interface (Hibbit et al., 2005). The interface y axis is perpendicular to the interface x axis in a way that x and y and z axes make a right handed system (Hibbit et al., 2005). The interface z axis is the slave surface normal and therefore the direction of which is determined by node numbers of the slave surface (Hibbit et al., 2005).

The next step is to calculate the bond capacity based on the values obtained in preceding steps. Next is to compute the incremental bond stress, $d\tau$, corresponding to different regions on the bond-slip diagram depending on the value of slip. These increments have to be mapped back to the software frame of reference and added to the previous values corresponding to the preceding iterations. The last stage is to store the current values of bond in the local coordinate system for every location as they will be used in the next step. Considering the small value of tensile chemical adhesion normal to the concrete-steel interface may help some cases of analysis become more stable as in some cases where there may be large out of plane deformations of the interface but in many cases it is neglected. According to the pullout tests by Feldman et al. (2005) on plain reinforcement the value of this stress is about $0.3\sqrt{f_c'}$ to $0.35\sqrt{f_c'}$ along the length of the plain bars. Here, it is assumed that this stress is the same in the

direction normal to bars. Considering this phenomenon when there is no instability due to deformations has little effect and hence is neglected.

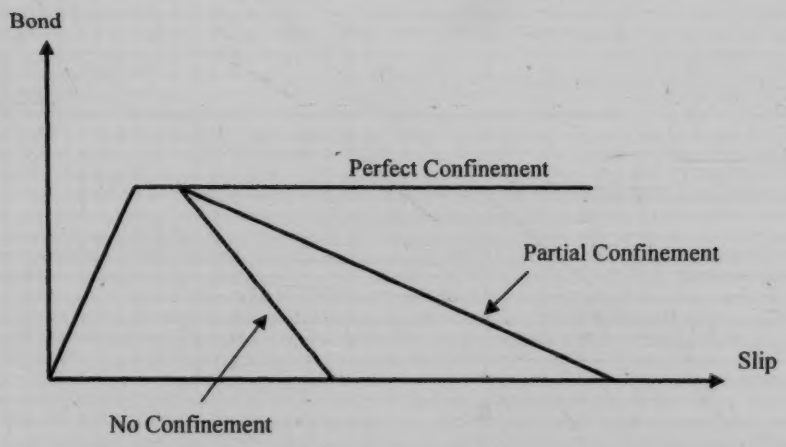

Figure (5.1) - Schematic Bond Slip Models for No, Perfect and Partial Confinement

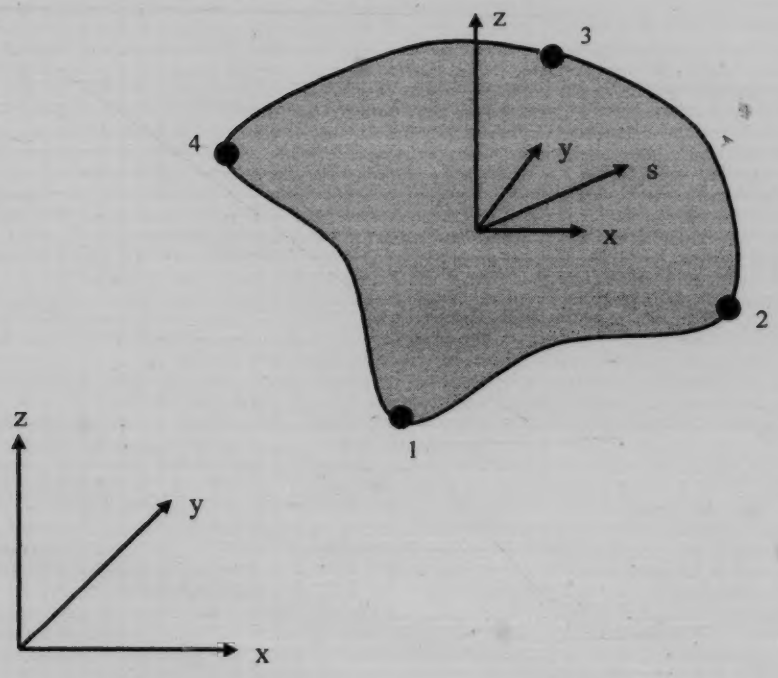

Figure (5.2) - Global, Interface and Model Coordinate Systems

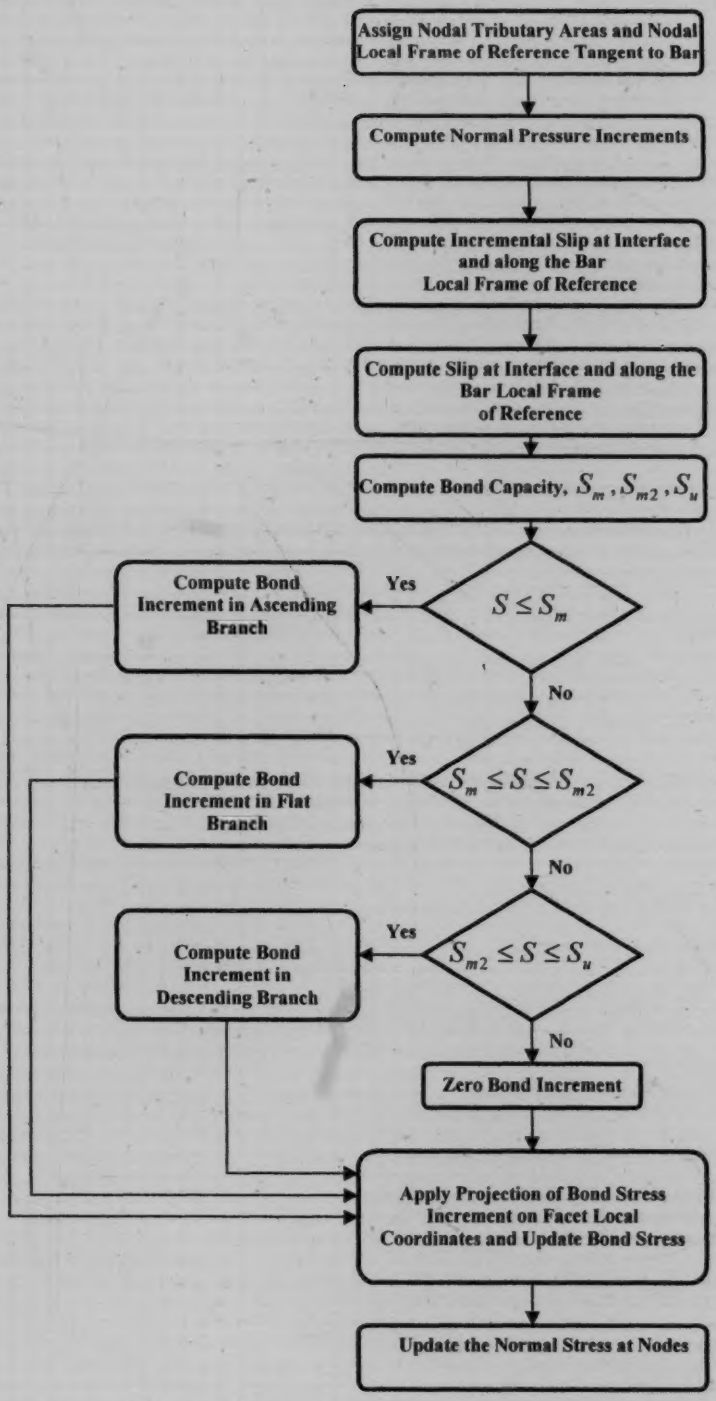
Assign Nodal Tributary Areas and Nodal Local Frame of Reference Tangent to Bar
Compute Normal Pressure Increments
Compute Incremental Slip at Interface and along the Bar Local Frame of Reference
Compute Slip at Interface and along the Bar Local Frame of Reference
Compute Bond Capacity, S_m, S_{m2}, S_u
$S \le S_m$
Yes
Compute Bond Increment in Ascending Branch
No
$S_m \le S \le S_{m2}$
Yes
Compute Bond Increment in Flat Branch
No
$S_{m2} \le S \le S_u$
Yes
Compute Bond Increment in Descending Branch
No
Zero Bond Increment
Apply Projection of Bond Stress Increment on Facet Local Coordinates and Update Bond Stress
Update the Normal Stress at Nodes

Figure (5.3) - Flowchart for Automatic Bond Model

6. Verification of Constitutive Model

6.1. Introduction

In this chapter, the proposed automatic bond model is tested against the results from the experimental work of chapter 3 and other researchers' tests to further verify the accuracy of the model. A total of 14 models were studied. These finite element models are simulations of past researchers' test specimens.

6.2. Properties of the Models

In this section properties of all test specimens tested by previous researchers are explained. These properties include strength of concrete, yield stress of steel bars and diameter of reinforcing bars as well as the number of specimens modeled in this chapter.

The properties of the present experimental work are explained in chapter 3. Specimens from Untrauer (1968), Eligehausen (1983) and Lormanometee (1974) are straight bar pullout specimens while specimens tested by Minor et al. are hook pullout tests. Table 6.1 shows all cases studied in this chapter.

6.2.1. Untrauer et al. (1968)

Three pullout specimens from Untrauer et al. (1968) are modeled. Untrauer's specimens are 6 inch cubes with a #6 (19mm) American bar in the middle. Normal pressure was applied on the top and bottom surfaces of the specimen. Three different values of 25 MPa, 32 MPa and 33 MPa define the strength of concrete in these specimens and the corresponding finite element models. Yield strength of steel is 635 MPa for all three specimens. Untrauer et al. used high strength steel to make sure their specimens fail in splitting. Figure (6.1) shows specimens tested by Untrauer et al.

6.2.2. Lormanometee (1974)

Six pullout specimens from Lormanometee (1974) were modeled by finite element method. Lormanometee's specimens are 6 inch cubes with #6 (19mm)

and #9 (28.5mm) American bars in the middle and top and bottom surface pressure were applied on them. Four different values define concrete strength in these specimens and the corresponding finite element models. These values are 35.8 MPa, 27 MPa, 28.45 MPa and 33 MPa. Yield stress for steel is 400 MPa for all these specimens and finite element models. Figure (6.1) shows specimens tested by Lormanometee.

6.2.3. Minor et al. (1975)

Two hook pullout specimens from Minor et al (1975) are modeled by finite element method. Specimens tested by Minor et al. are 90 degree hook pullout tests. These specimens are shown in figure (6.2). As for type of bar, #7 (22.22mm) American bars were used in Minor's specimens. The nominal yield strength of steel was 400 MPa but in the actual tests, each specimen exhibited a somewhat higher strength. However in analysis the nominal strength was used and analysis was terminated at that strength and the corresponding diagrams are presented up to this nominal strength.

6.2.4. Eligehausen et al. (1983)

Two pullout specimens from Eligehausen (1983) are modeled by finite element method.

A typical Eligehausen's specimen is shown in figure (6.3) which includes a #8 (25.4mm) American bar. Pressure is applied on top and bottom surfaces. The strength of concrete is 30 MPa for both specimens and the corresponding finite element models. Yield strength of steel is 530 MPa for both models and the corresponding finite element models. Eligehausen et al. specimen 1.4.2 does not have any stirrups or vertical reinforcement. However, specimen 6.4 has #4 stirrups and vertical bars and a normal pressure of 13.5 MPa on the two ends. In all Eligehausen's specimens a plastic sheet was placed in the middle of specimen to make a pre-split region in the middle except a small area within the stirrups. In addition, a tube has been used to de-bond that part of steel going through the plastic sheet region.

6.3. Finite Element Mesh

The finite element mesh for specimen of chapter 3 is shown in figure (6.4) and has already been explained in detail in chapter 4. Therefore, in this chapter only the finite element meshes for specimens tested by other researchers will be described in detail.

6.3.1. Untrauer et al. (1968) and Lormanometee (1974)

The finite element mesh for these specimens is illustrated in figure (6.5). Three dimensional wedge elements have been used to model concrete in these specimens. However, reinforcement is modeled with three dimensional brick elements. The type of elements used for these specimens are chosen according to several trials because using three dimensional brick elements for concrete in these cases results in severe distortion of elements and the mesh. Using a very coarse mesh decreases the accuracy of analysis. Because of the symmetry of these specimens, only one fourth is modeled. Appropriate boundary conditions are applied on the planes of symmetry to reflect the symmetry about the corresponding planes. These specimens were pullout tests and therefore in analysis a moving boundary condition is applied to one end of reinforcement and the corresponding face of the concrete finite element mesh is restrained by appropriate boundary conditions to simulate the pullout condition. Normal pressure was applied on top and bottom faces of these specimens. Therefore, in the finite element model normal pressure was applied on the bottom face while the top face was restrained by symmetry boundary conditions.

Considering the steel-concrete interface, the nodes of steel and concrete elements on this interface are not connected in the mesh. In other words, different node numbers are assigned to the same location corresponding to the nodes on steel-concrete interface. Although at the beginning of analysis concrete and steel nodes of the contact interface are coincident they slip on each other later in the analysis and the bond model procedure of chapter 5 is applied on this surface by a FORTRAN user subroutine. In addition, the steel contacting surface tends to

penetrate into the concrete contacting surface which is checked by the model normal interaction between two surfaces in the abovementioned subroutine. In the three finite element models made for Untrauer et al. specimens three different normal pressures are applied: 6.21 MPa, 0 MPa and 6.53 MPa. For the case of six finite element models simulating Lormanomette's tests four different normal pressures were applied: 0 MPa, 17.23 MPa, 2.6 MPa and 14.6 MPa.

6.3.2. Eligehausen (1983)

The finite element mesh for Eligehausen's specimens consists of three dimensional wedge elements for concrete and steel. This type of element was chosen based on a number of trials with other element types. Here, coarse meshes rendered inaccurate results and on the other hand too fine meshes result in excessive distortion of mesh. Therefore, in this case using a large number of elements should be avoided. Eligehausen's specimens were modeled from the face of the bonded bar through the end of its length and the unbonded length was not modeled since it is not considered in the bond model procedure and carries no force.

Eligehausen's tests are pullout tests and to simulate that the end of the bar in the finite element mesh has to be under moving boundary conditions while the corresponding concrete face is restrained. These specimens are symmetric about two planes, and therefore, only one fourth was modeled. Boundary conditions due to symmetry were imposed on the planes of symmetry. In these specimens, Normal pressure was applied on two opposite faces. Therefore, in the finite element mesh a normal pressure was applied at the bottom face while the top face of mesh was restrained as a condition of symmetry. Figure (6.6) shows the finite element mesh for Eligehausen's specimen. Stirrups were modeled by truss elements but are not highlighted here.

At the steel-concrete contact surface, nodes are not connected in the conventional way in a finite element mesh. They are connected through the contact algorithm

described in chapter 5 using a FORTRAN user subroutine. Coincident nodes are considered for the concrete-steel interface at the beginning of analysis but later in analysis these nodes take different locations and corresponding bond stresses and normal pressures are imposed on them. Normal pressures applied to the two finite element meshes simulating Eligehausen et al. specimens were 0 MPa and 13.5 MPa.

6.3.3. Minor et al. (1975)

As for the specimens tested by Minor et al. three dimensional wedge elements have been used for both concrete and steel. The choice of element type has been made according to several trials. Minor et al. specimens were symmetric about only one plane, and therefore, only half of them were modeled. Appropriate boundary conditions were applied to reflect on this symmetry. Since this is a pullout test, moving boundary conditions have been imposed on the end of reinforcement while the bottom part of the corresponding face of concrete was restrained against moving. This produces a moment which is balanced by a couple produced by the boundary conditions on a group of elements on top and bottom faces of finite element mesh. This is illustrated in figure (6.7). The steel concrete interface is modeled using concrete and steel elements with initially coincident but separate nodes, which relate to each other later in analysis using the contact algorithm of chapter 5. Since there is an unbonded straight part in Minor et al. specimen, the corresponding steel-concrete interface in that part is not assigned any bond behavior. Therefore, for the unbonded part of interface steel and concrete surfaces can freely slip on each other without any resisting bond.

6.4. Material Properties

The damaged plasticity model is applied to model the concrete. This type of material model is described in chapter 4 and will not be explained here.

The compression and tension softening curves for different models are presented in figures (6.8) to (6.25).

6.5. Analysis Procedure and Results

For the case of the specimen of chapter 3, three diagrams are compared. These diagrams are the test load-displacement diagram, analysis result using the method explained in chapter 4 and analysis result using the method of chapter 5. For other cases only two graphs are compared which are the test result and analysis result using the method of chapter 5.

Analysis procedure is explicit analysis using software ABAQUS which is explained in chapter 4. To speed up analysis the method of mass scaling has been used. The values of scaling used in these analyses are different. That is because based on the dimensions of specimen and steel and conditions of loading different values are needed to give a stable analysis. All specimens were tested with low loading rates except Eligehausen's which were tested under higher loading rate conditions. For Untrauer specimens a variable mass scaling procedure was used to give a stable time increment of at least 0.0005 seconds for all elements. The time increment used was 0.0003 for the total analysis period of 10 seconds. For Lormanometee's specimens a variable mass scaling was used to give a stable time increment of 0.005 seconds. The time increment used was 0.0005 seconds for a total analysis period of 10 seconds. In the case of Eligehausen's specimens variable mass scaling was used to give a stable time increment of 0.001 seconds. The time increment used was 0.0003 seconds for a total analysis period of 20 seconds. For Minor's specimens a variable mass scaling was used to give stable time increment of 0.005 seconds and the time increment used was the 0.005 seconds for the total analysis period of 5 seconds.

Table 6.2 provides a summary of the present finite element models and analysis results of straight length pullout specimens tested by past researchers. This table makes it clear that there is close agreement between the present finite element results and the literature. Table 6.3 provides a summary of the present finite element results and the experimental results of hook pullout tests. Slip values for each model are mentioned in terms of u_y which is the slip value at yielding of

steel in finite element analysis. Good agreement can be seen between analysis and test results in this table using R^2 measure.

Additionally in this section, bond-slip diagrams for a number of these models are compared with the available test result diagrams. These diagrams are shown in figures (6.26) to (6.33). According to these figures there is good agreement between the present finite element results and the present and past test result diagrams. Two comparisons have been made with the finite element model proposed by Lowes et al. (2004). Their model is accurate with respect to confined concrete but is not accurate to model unconfined concrete. This is because Lowes' model is not able to model splitting of concrete. Lowes et al. tried to model both confined and unconfined concrete by proposing a zero thickness interface element and imposing special mathematical conditions in their formulation. They were successful with respect to perfectly tied concrete cases since their model is perfectly able to simulate shearing mode of failure which happens in confined cases. However, their model failed to render an accurate result for cases involving no confinement. For the unconfined case, Lowes et al. approach does not match the real capacity and general behavior exhibited by test. Eligehausen et al. confined and unconfined specimens were modeled by Lowes et al. Comparison of their results with test results and the present finite element approach in this research is given in figures (6.30) and (6.31). These figures show the present finite element model is able to model both confined and unconfined concrete.

6.6. Conclusion

The present automatic bond model has been compared with the present and past experimental results. Good agreement is observed between results from present finite element approach and present and previous tests. In two cases, the present approach has been compared with previous finite element results. As can be seen in figure (6.30), when there is no stirrups the previous finite element model gives results that do not match test results. The present model does not exhibit this deficiency and it gives a close match to previous test results. With respect to the

case with lateral reinforcement although a flat descending branch was used, the failure due to shear of concrete happened in a close match to test results.

Case	Specimen Name	Researcher	Bar Type	f'_c (Mpa)	f_y (Mpa)
1	Specimen of Chapter 3	Present	35M	35	400
2	36625	Untrauer (1968)	# 6	25	635
3	46600	Untrauer (1968)	# 6	32	635
4	47620	Untrauer (1968)	# 6	33	635
5	6-6-52-0-A4	Lormanometee (1974)	# 6	35.8	400
6	6-6-52-48-A2	Lormanometee (1974)	# 6	35.8	400
7	6-6-52-24-A6	Lormanometee (1974)	# 6	35.8	400
8	6-6-39-0-D1	Lormanometee (1974)	# 6	27	400
9	9-6-41-0-G1	Lormanometee (1974)	# 9	28.45	400
10	9-6-48-43-J6	Lormanometee (1974)	# 9	33	400
11	1.4.2	Eligehausen (1983)	# 8	30	530
12	6.4	Eligehausen (1983)	# 8	30	530
13	7-8.5-90-1.5 A	Minor (1975)	# 7	38	400
14	7-8.5-90-1.5 B	Minor (1975)	# 7	40	400

Table (6.1) – Specimens Modeled in This Chapter

Case	Specimen Name	Researcher	σ_N (Mpa)	τ_{max} from Test (Mpa)	τ_{max} from FE (Mpa)	$\frac{\tau_{max-FE}}{\tau_{max-Test}}$
2	36625	Untrauer	6.21	13	12.3	0.95
3	46600	Untrauer	0	9	8.8	0.98
4	47620	Untrauer	6.53	16.3	14	0.86
5	6-6-52-0-A4	Lormanometee	0	8.8	9.6	1.09
6	6-6-52-48-A2	Lormanometee	17.23	19	19.7	1.04
7	6-6-52-24-A6	Lormanometee	8.61	18.9	17	0.9
8	6-6-39-0-D1	Lormanometee	0	8.1	7.9	0.98
9	9-6-41-0-G1	Lormanometee	0	6.2	6.13	0.99
10	9-6-48-43-J6	Lormanometee	14.6	18.6	15.5	0.83
11	1.4.2	Eligehausen	0	6	5.5	0.92
12	6.4	Eligehausen	13.5	17	17	1
					Average =	**0.958182**
					Standard Deviation =	**0.07**

Table (6.2) – Summary of Straight Length Tests and FE Models

Model	Slip (mm)	Lead Stress from Test (MPa)	Lead Stress from FE (MPa)	Comparison
Model A	$u_y = 0.85$	357	400	$R^2 = 0.96$
	$0.75u_y$	298	330.5	
	$0.5u_y$	224	245.3	
	$0.25u_y$	116	133.1	
	0	0	0	
Model B	$u_y = 1$	371.62	400	$R^2 = 0.92$
	$0.75u_y$	311	383	
	$0.5u_y$	225	282.1	
	$0.25u_y$	123.32	151.34	
	0	0	0	

Table (6.3) – Hook Pullout Models

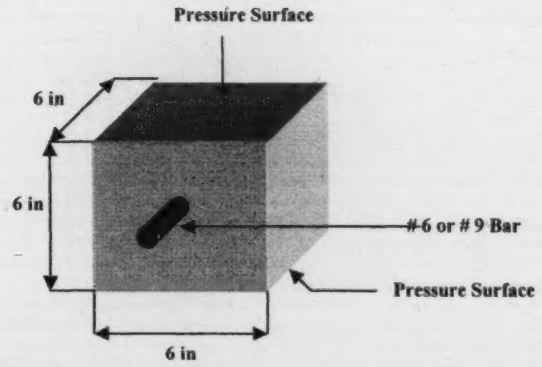

Figure (6.1) - Schematic Drawing of Specimen Tested by Lormanometee (1974) and Untrauer et al. (1968)

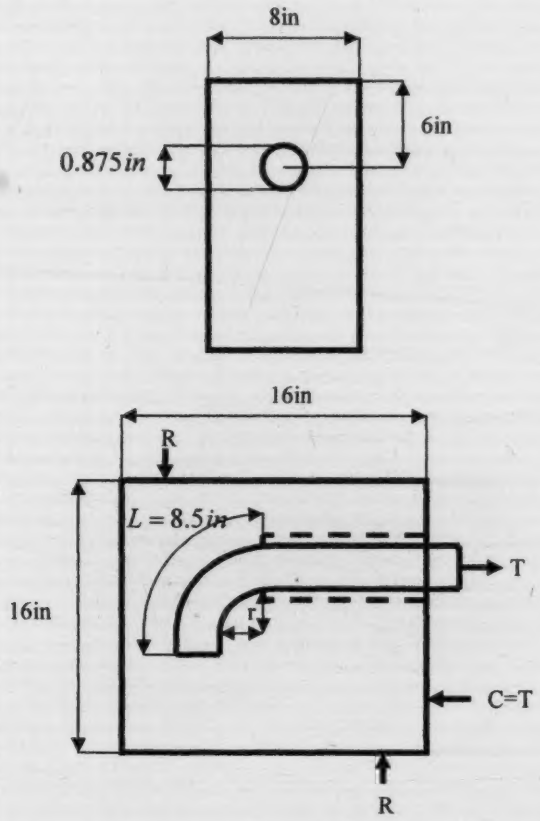

Figure (6.2) - Schematic Drawing of Specimen Tested by Minor et al. (1975) (Not to Scale)

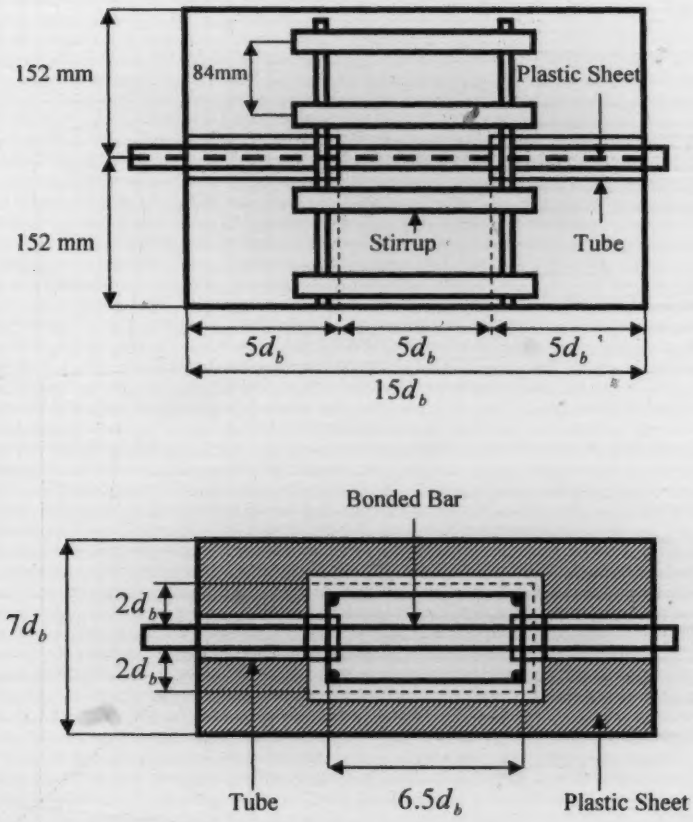

Figure (6.3) - Schematic Drawing of Specimen Tested by Eligehausen et al. (1983)

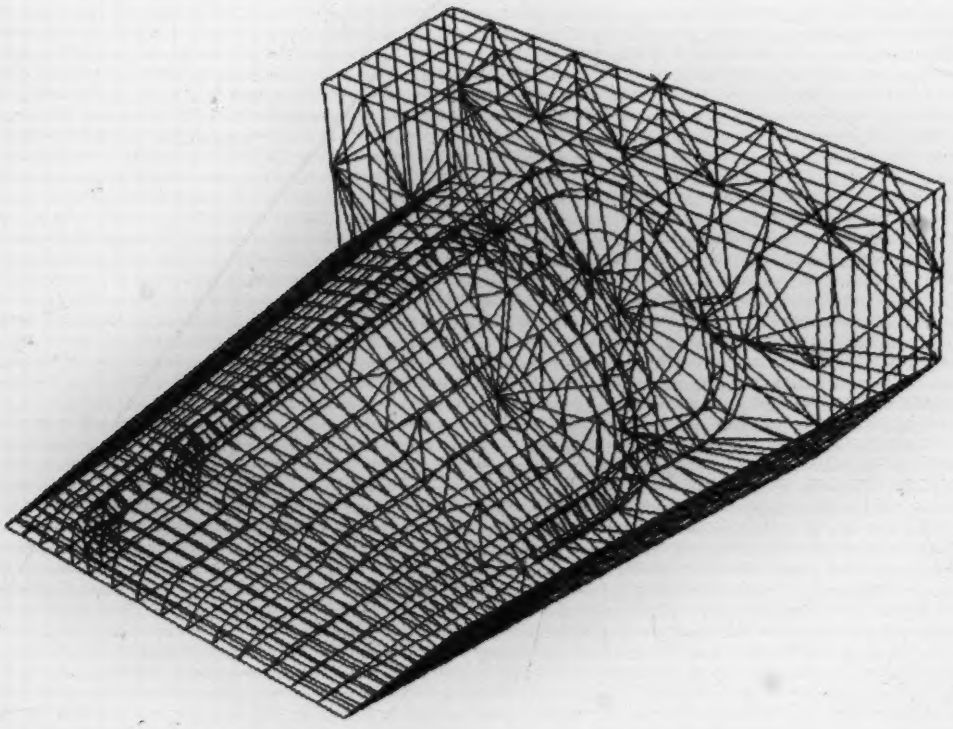

Figure (6.4) – FE mesh for Specimen of Chapter 3

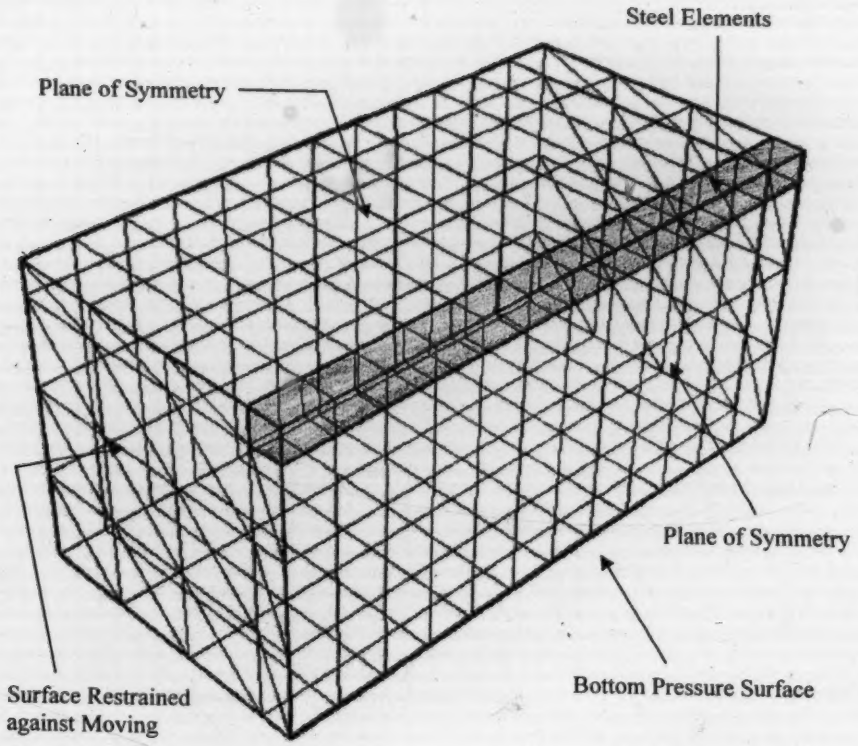

Figure (6.5) – FE mesh for 6 Inch Cube Specimens from Untrauer and Lormanometee

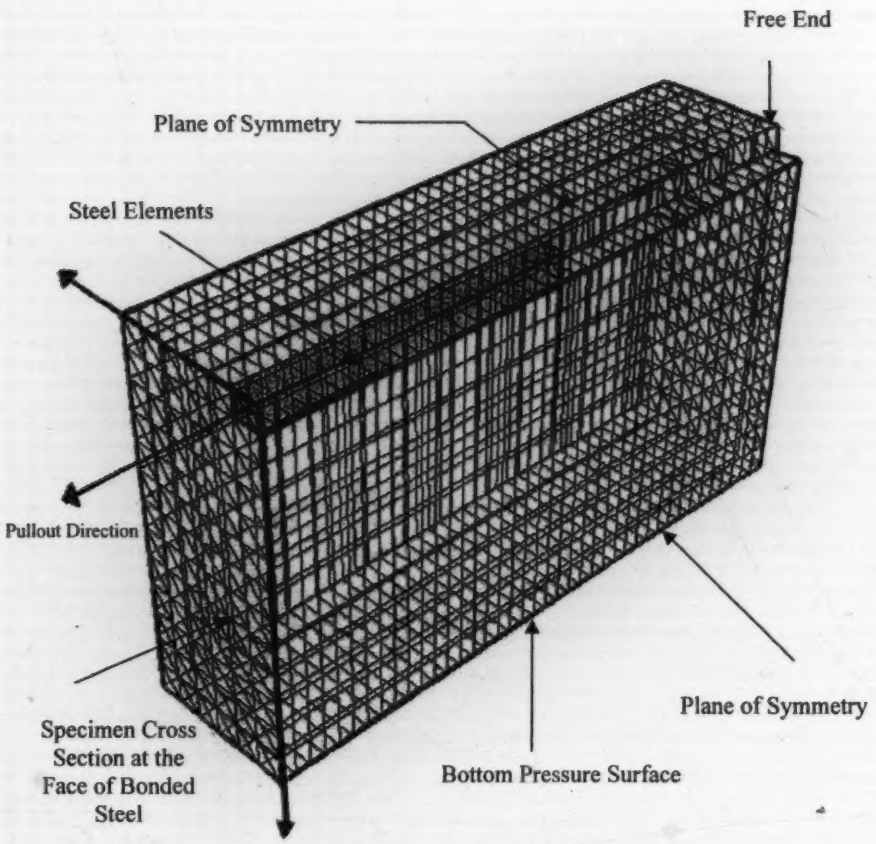

Figure (6.6) – FE mesh for Eligehausen's Specimens

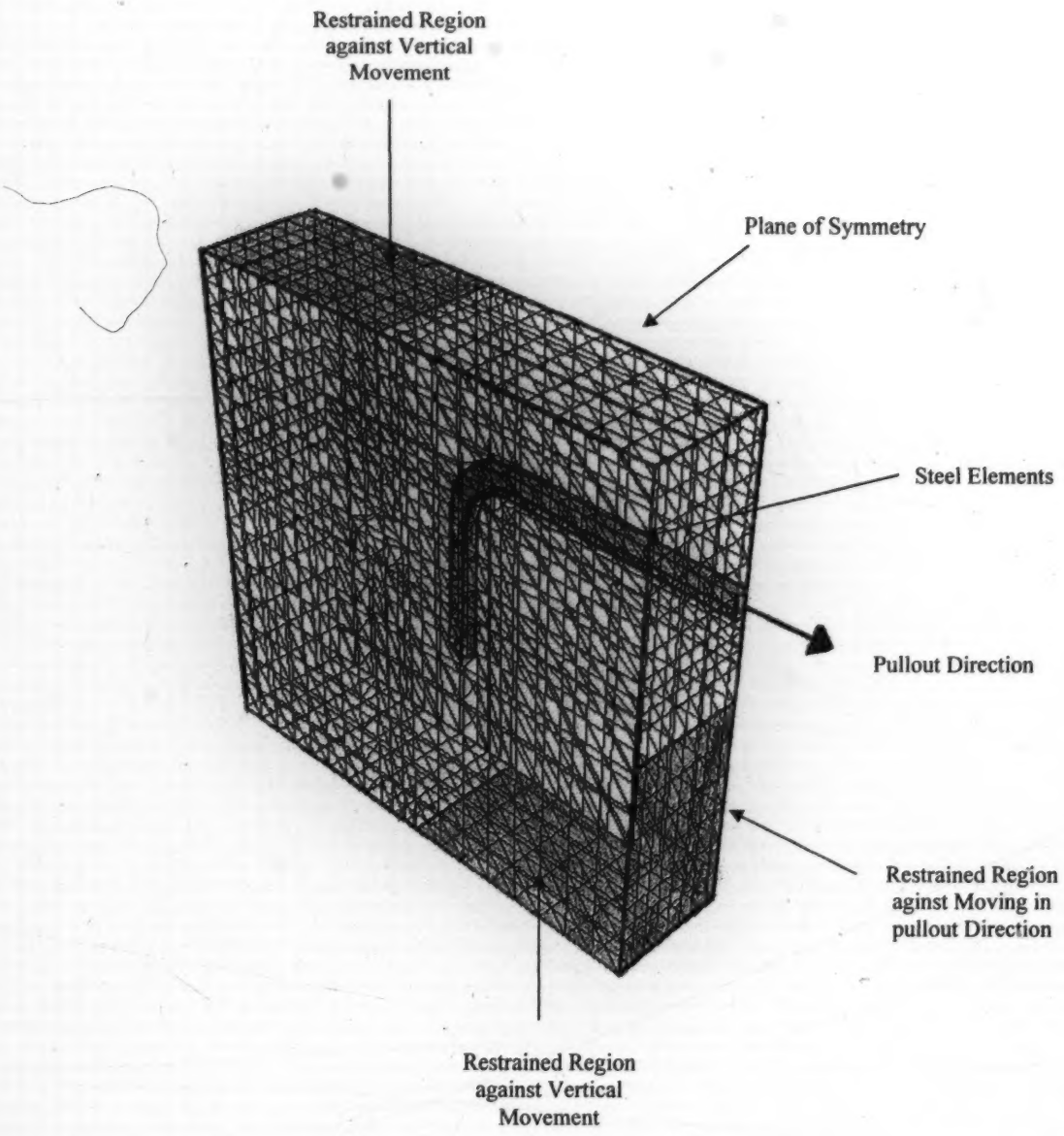

Figure (6.7) – FE mesh for Minor Specimens

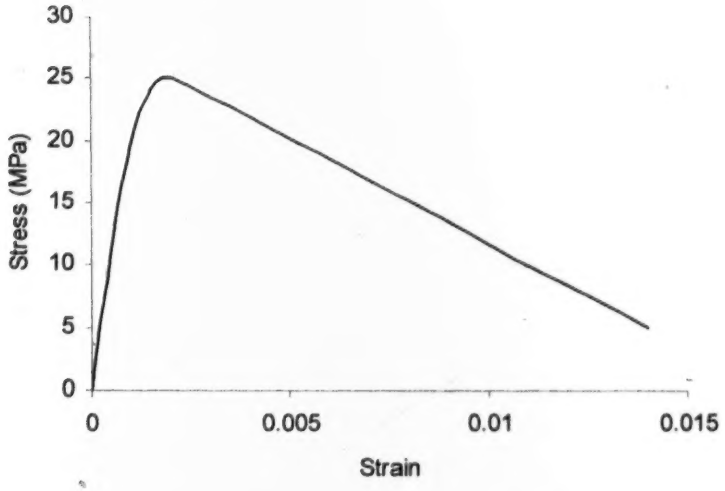

Figure (6.8) – Saenz Compression Curve for FE Model of Case 2

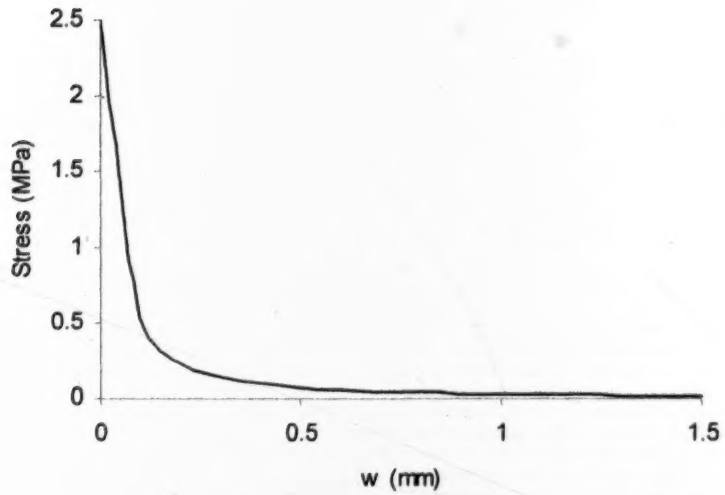

Figure (6.9) – Tension Softening Curve for FE Model of Case 2

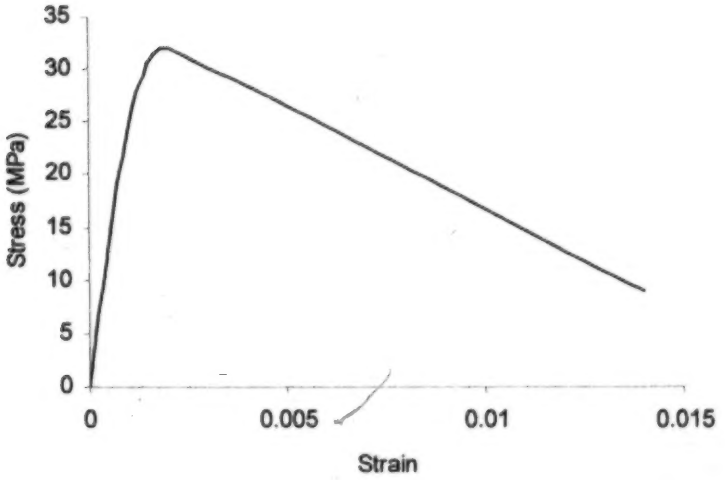

Figure (6.10) – Saenz Compression Curve for FE Model of Case 3

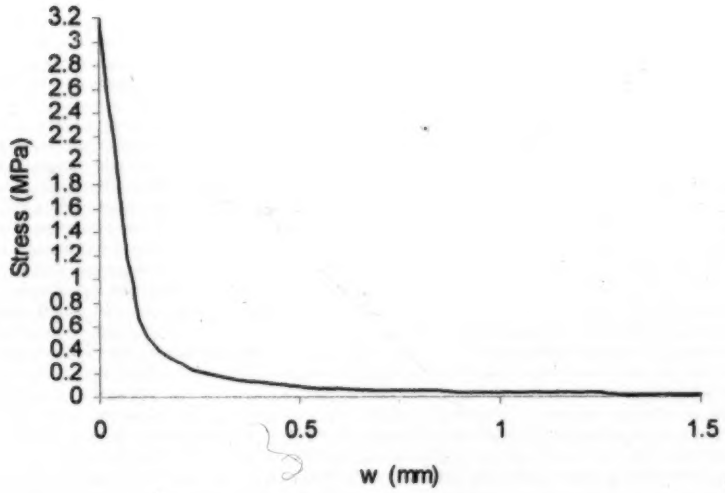

Figure (6.11) – Tension Softening Curve for FE Model of Case 3

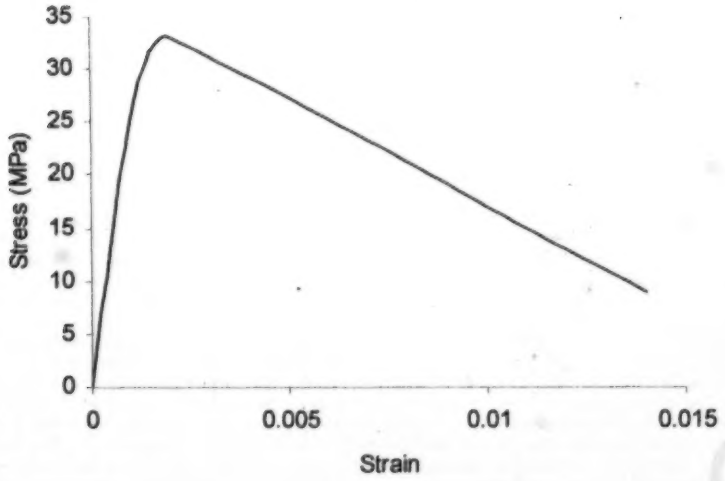

Figure (6.12) – Saenz Compression Curve for FE Model of Cases 4 and 10

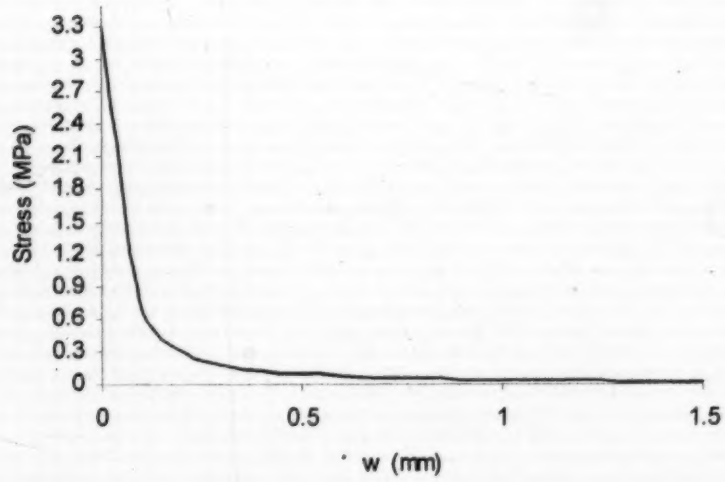

Figure (6.13) – Tension Softening Curve for FE Model of Cases 4 and 10

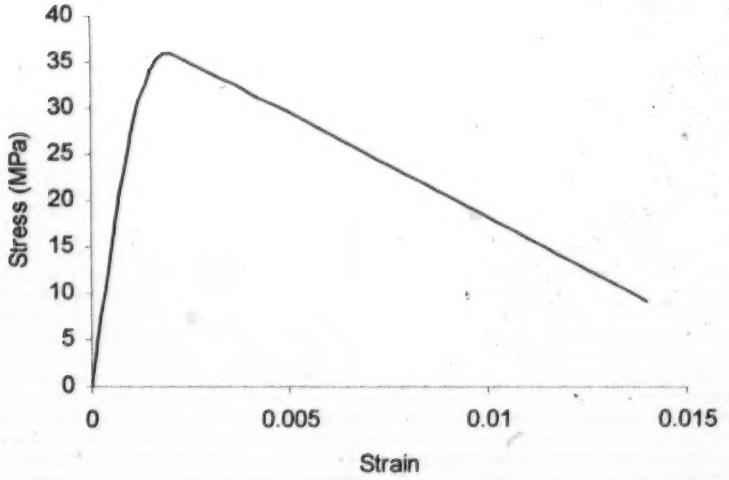

Figure (6.14) – Saenz Compression Curve for FE Model of Cases 5, 6 and 7

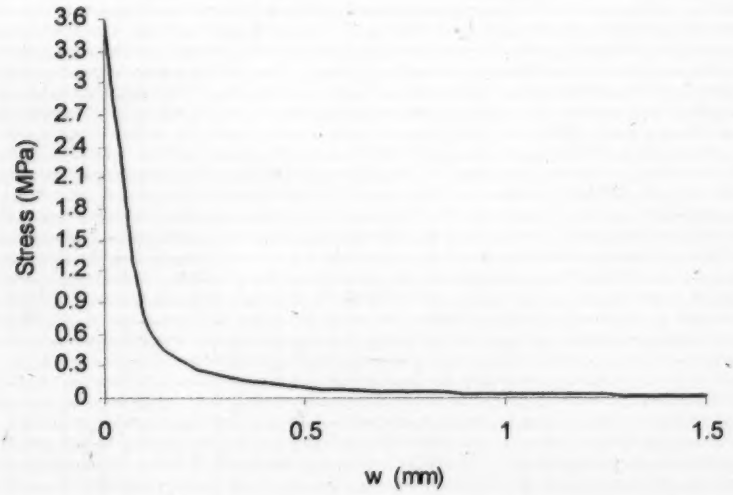

Figure (6.15) – Tension Softening Curve for FE Model of Cases 5, 6 and 7

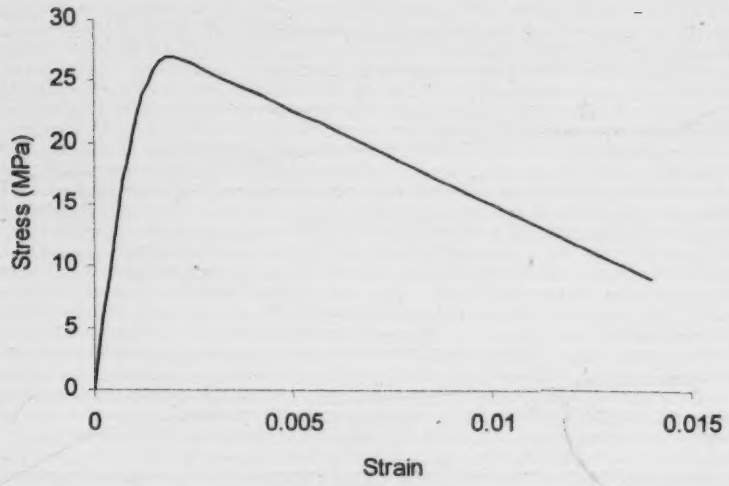

Figure (6.16) – Saenz Compression Curve for FE Model of Case 8

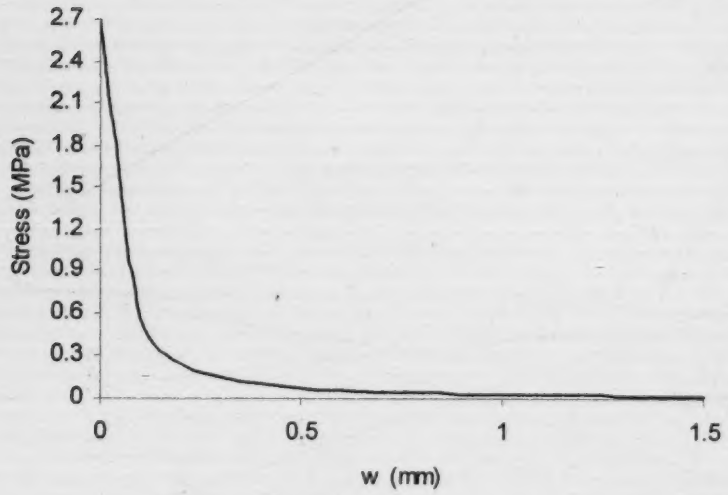

Figure (6.17) – Tension Softening Curve for FE Model of Case 8

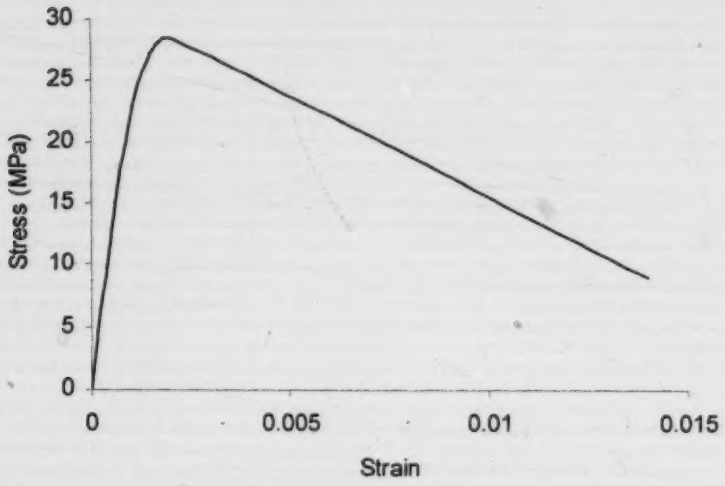

Figure (6.18) – Saenz Compression Curve for FE Model of Case 9

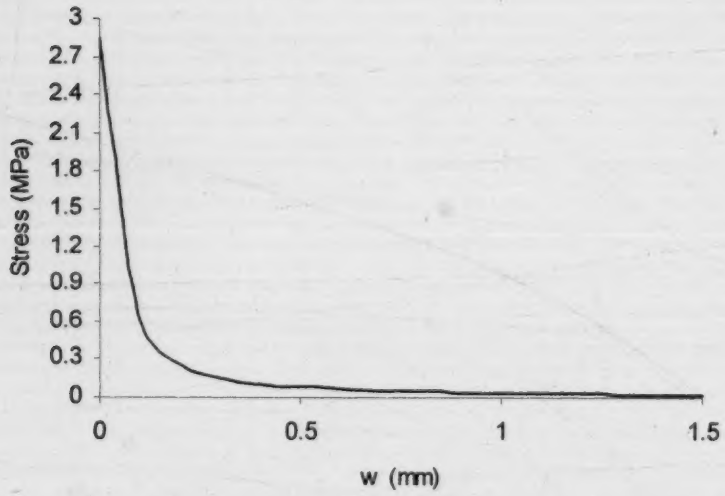

Figure (6.19) – Tension Softening Curve for FE Model of Case 9

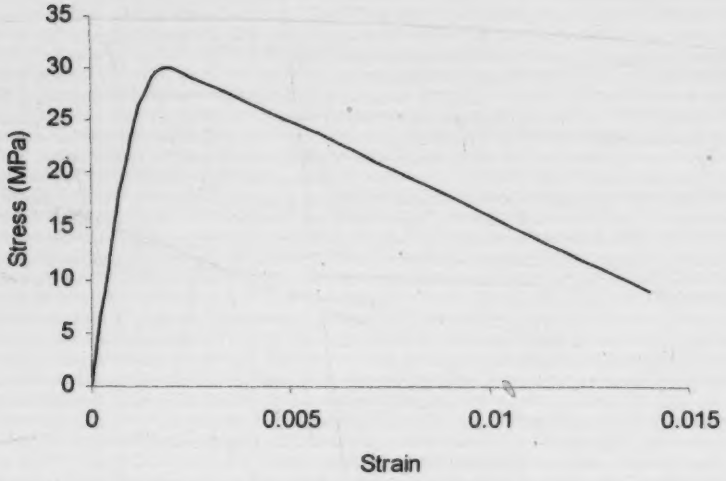

Figure (6.20) – Saenz Compression Curve for FE Model of Cases 11 and 12

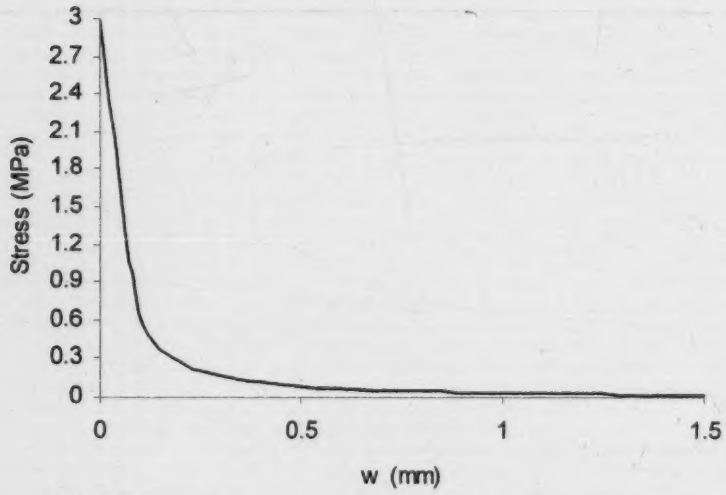

Figure (6.21) – Tension Softening Curve for FE Model of Cases 11 and 12

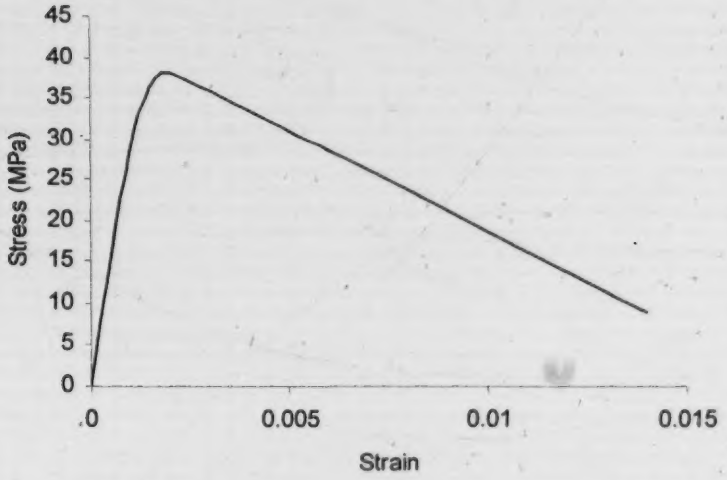

Figure (6.22) – Saenz Compression Curve for FE Model of Case 13

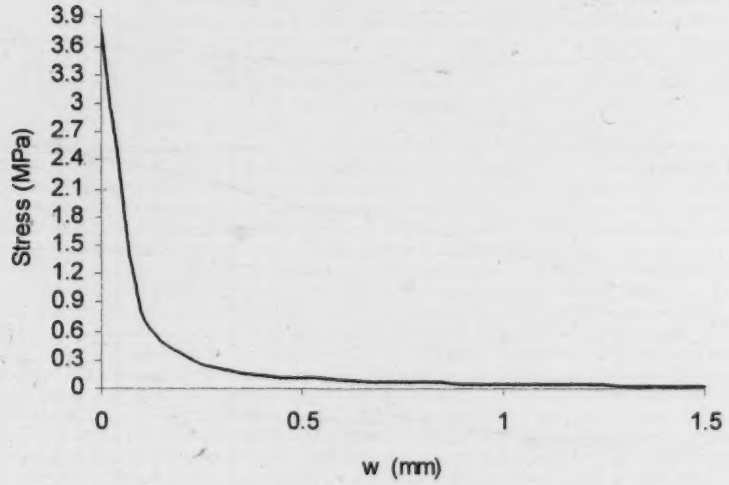

Figure (6.23) – Tension Softening Curve for FE Model of Case 13

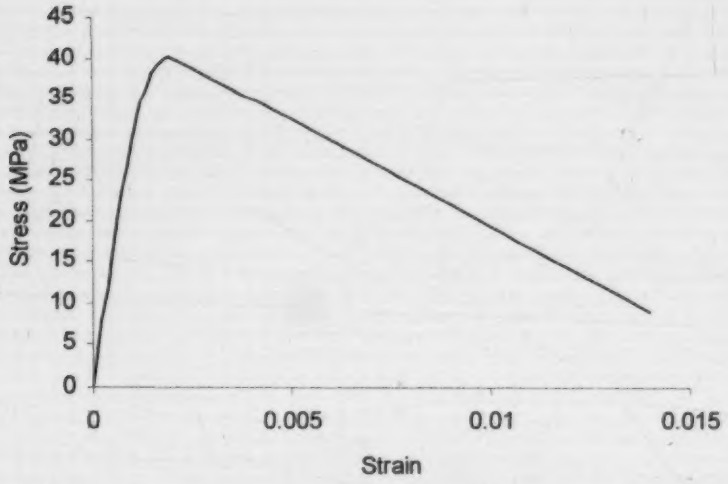

Figure (6.24) – Saenz Compression Curve for FE Model of Case 14

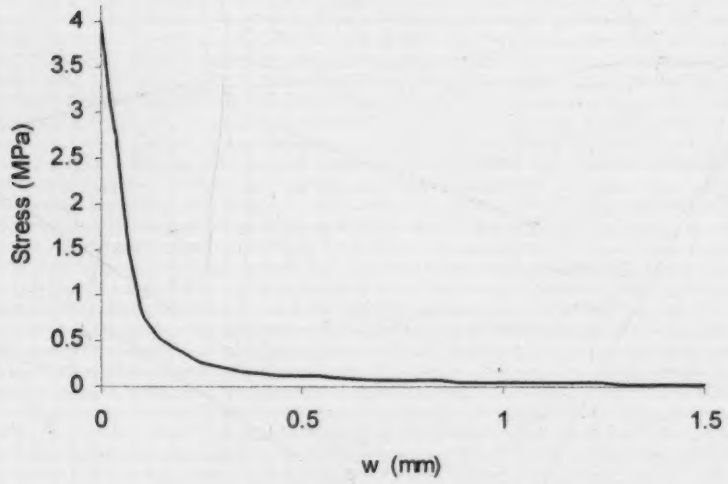

Figure (6.25) – Tension Softening Curve for FE Model of Case 14

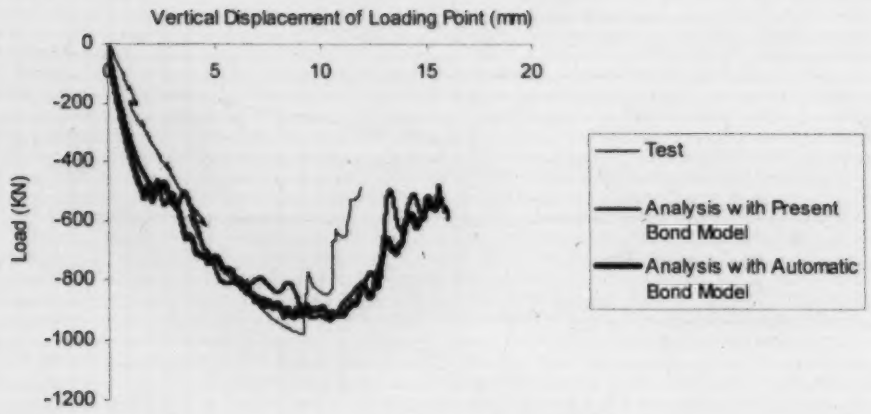

Figure (6.26) – Comparison of the Present Finite Element Approach with Present Test Results

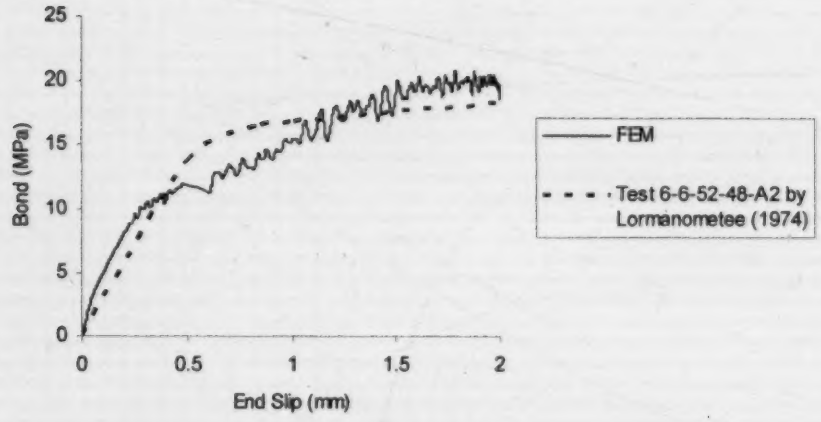

Figure (6.27) – Comparison of the Present Finite Element Approach with Lormanometee's Test Results

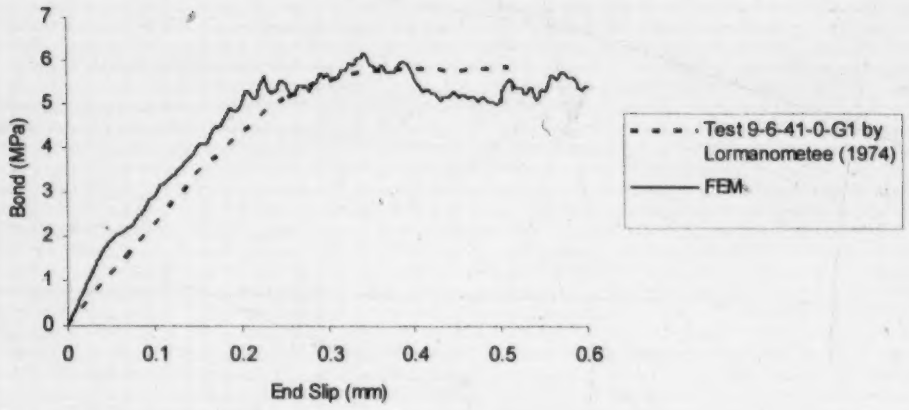

Figure (6.28) – Comparison of the Present Finite Element Approach with Lormanometee's Test Results

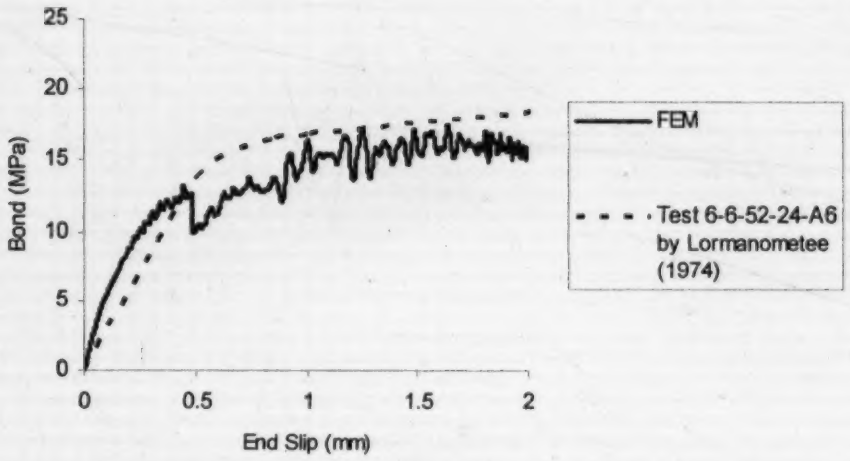

Figure (6.29) – Comparison of the Present Finite Element Approach with Lormanometee's Test Results

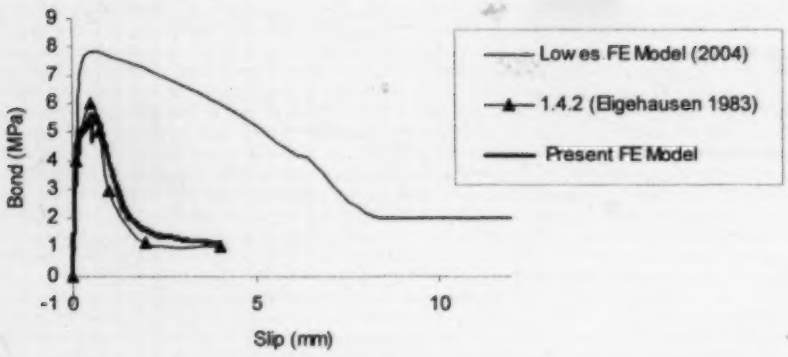

Figure (6.30) – Comparison of the Present Finite Element Approach with Eligehausen's Test Results

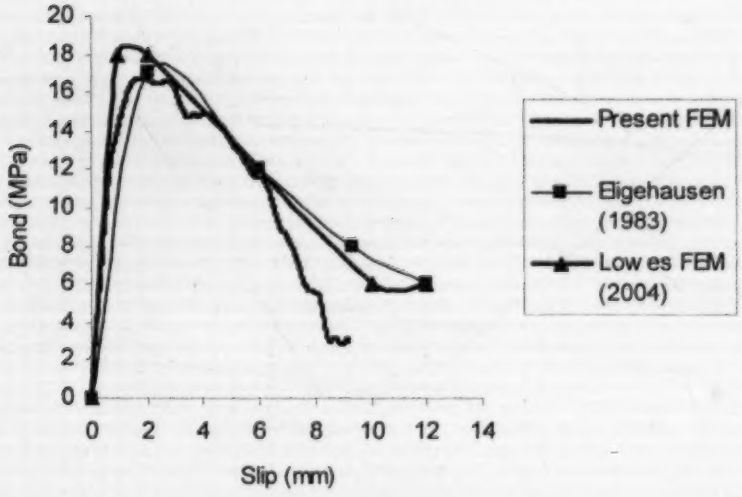

Figure (6.31) – Comparison of the Present Finite Element Approach with Eligehausen's Test and Lowes' FEM results

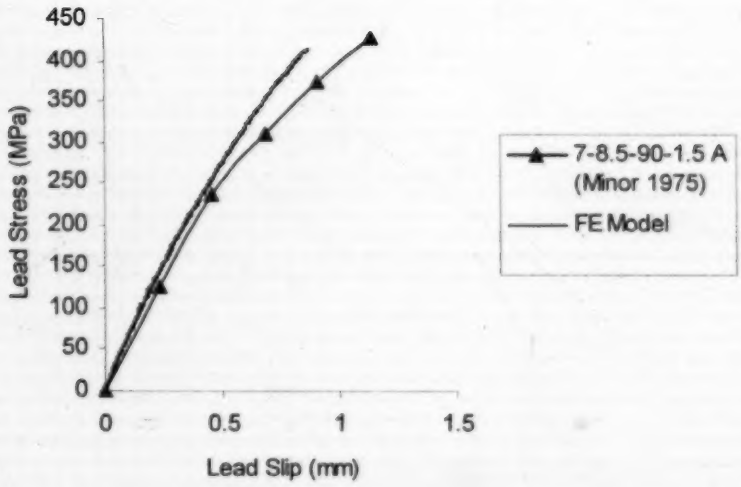

Figure (6.32) – Comparison of the Present Finite Element Approach with Minor's Test Results

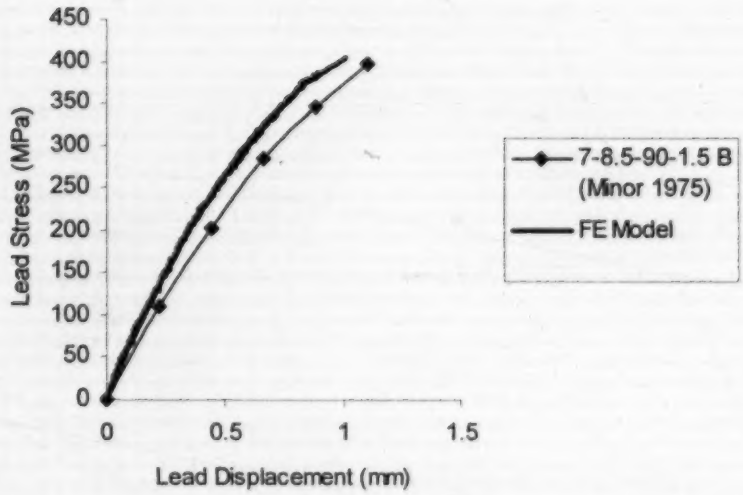

Figure (6.33) – Comparison of the Present Finite Element Approach with Minor's Test Results

7. Parametric Study of the Anchorage of Hooked Bars

7.1. Introduction

The purpose of this chapter is to evaluate a few of the Canadian code provisions with respect to anchorage of hooked bars. In this chapter a finite element parametric study of 90 degree hooks is carried out using the bond model developed in this research. Reinforcing bars used in this study are of large diameters. This kind of hook is widely used in beam-column joints and other structures such as tunnels and bridges. The development length of large diameter bars are the most critical since they require more bond accumulated to achieve yield stress of the corresponding large cross-sections. The parameters of interest in this chapter are the radius of bend, and the length of hook tail. These parameters are studied to determine their influence on hook capacity. A comparison of results with the provisions of the Canadian code is made to identify if these provisions are conservative. Finally conclusions and suggestions are presented.

7.2. Description of the Models

Figure (7.1) illustrates the type of joint models being studied. The hook consists of a bent part, a tail and a straight length. The pulling force is applied at the end of the straight part as the reaction to this force is applied on the concrete below. The resulting moment will balance with two compressive reactions on top and bottom faces of the model. Except in one case, the straight part is unbonded but the bend and tail parts are fully bonded. This facilitates the exclusive study of the bent and tail parts as it greatly helps make a meaningful comparison with the code.

Bars of interest are 30M, 35M and 45M Canadian bars. For every bar size two radii of bend are studied which are the minimum bend diameter and twice the minimum bend diameter as defined in the Appendix A of the CSA-A23.3 code for the 400W type of steel. The minimum bend diameter in the code is recommended

for practical reasons. In other words, it is impractical to bend large bars with smaller than minimum diameters in the workshop. These minimum values are specified in table (7.1) with a star in front of the corresponding values. However, it is possible to have a bend diameter larger than the minimum. Development lengths of hooks in CSA-A23.3 are based on an equation in terms of bar diameter and strength of concrete. In other words, the development length equation of the code does not account for the bend radius and the same equation is used for the different bend radii as long as strength of concrete and bar sizes are the same. Tail lengths of interest are $12\,d_b$, $8\,d_b$ and $4\,d_b$. The concrete strength is 30 MPa. The tail length of $12\,d_b$ is recommended by the A23.3 code for anchorage of 90 degree hooks. Based on ACI Manual of Concrete Practice (2005), for small concrete covers and small tail lengths there is a possibility for the tail to pop out. Different tail lengths are examined to clarify the effect of tail length on the capacity of hooks.

Based on CSA-A23.3, when both the side and top covers are less than 60 mm thick, stirrups should be used to confine the hook. However, dimensions of these models are selected to give a stirrup-free design based on the provisions of CSA-A23.3. Stirrups are avoided because only the effects of bend radius and tail length are to be studied. In other words, using stirrups would interfere with other parameters and a clear conclusion on the effect of the parameters of interest would not be made.

High strength concrete and large covers are avoided to allow for the undesirable failure, which is under investigation, to happen, although there is no apparent mistake in design. Based on bond capacity equations for confined and unconfined concrete in chapters 4 and 5, bond capacity increases with increased concrete strengths and cover values.

7.3. Finite Element Mesh

Nineteen different finite element meshes were used in this study. For cases 1 to 3 the cross section dimension and the length of the model in millimeters are 425×648 and 680 respectively. The bend radius of reinforcement for these cases is 125 mm. For case 1, 2 and 3 the tail lengths are 140 mm 280 mm and 420 mm respectively. For cases 4 to 6 the cross section dimensions and the length of the models in millimeters were 425×773 and 805 respectively. The bend radius of reinforcement for these cases is 250 mm. In cases 4, 5 and 6 the tail lengths are 140 mm, 280 mm and 420 mm respectively. For cases 7 to 9 the cross section dimensions and the length of the models in millimeters are 400×558 and 590 respectively. The bend radius of reinforcement for these cases is 100 mm. In cases 7, 8 and 9 the tail lengths are 120 mm, 240 mm and 360 mm respectively. For cases 10 to 12 the cross section dimensions and the length of models were 400×658 and 690 millimeters respectively. The bend radius of reinforcement for these cases is 200 mm. In cases 10, 11 and 12 the tail lengths are 120 mm, 240 mm and 360 mm respectively. For cases 13 to 15 the cross section dimensions and the lengths of models were 475×853 and 885 millimeters respectively. The bend radius of reinforcement for these cases is 200 mm. In cases 13, 14 and 15 the tail lengths are 180 mm, 360 mm and 540 mm respectively. For cases 16 to 18 the cross section dimensions and lengths of models were 475×1053 and 1085 millimeters respectively. The bend radius of reinforcement for these cases is 400 mm. In case 16, 17 and 18 the tail lengths are 180 mm, 360 mm and 540 mm respectively. For case 19 the cross section dimensions and the length of the model were 400×558 and 590 millimeters respectively. The bend radius of reinforcement for this case is 100 mm. In case 19, the tail length is 360 mm. Table 7.2 shows all mesh dimensions. In this table, because of the condition of symmetry the model widths are divided by two.

Concrete and steel elements are both modeled with three dimensional wedge elements as shown in figures (7.4) to (7.22). Because of the symmetry only half of the structure is modeled and the condition of symmetry is applied by

appropriate boundary conditions on the plane of symmetry. To demonstrate the difference in different meshes important concrete and steel dimensions are shown on the surface of the meshes in figures (7.4) to (7.22).

Coincident concrete and steel nodes are defined at the concrete-steel interface. These nodes initially take the same location but further in analysis they take different locations and will not be coincident. In other words, they slip on each other and steel nodes penetrate into concrete surface. The relative movement of steel and concrete nodes in governed by the bond model explained in chapter 5. FORTRAN user subroutines have been used to facilitate this bond model. The unbonded part of steel is excluded in the contact modeling since the movement of steel in this region produces no bonding force.

The pullout condition is modeled by using changing displacement boundary conditions on the nodes on the perimeter of the cross section of the reinforcement. The bottom part of the concrete cross section is restrained against movement in pullout direction. The resulting moment from the pullout procedure is balanced by a set of boundary conditions on a group of elements on top and bottom surfaces. These boundary conditions restrain movement in vertical direction. Equivalent cross sections are used to model reinforcement. This kind of cross section was described in chapter 4. Since the perimeter of the equivalent cross section is not the same as the real circular cross section the bond forces carried by nodes are computed with regard to the real cross section perimeter.

7.4. Analysis Procedure

Quasi static explicit analysis has been carried out using the bond model and automatic procedure introduced in the preceding chapters. To accelerate the analysis the method of mass scaling has been adopted. Variable mass scaling has been used in a way that for meshes with 30M bars it gives a stable time increment of 0.002 seconds for all elements. The time increment was 0.0004 seconds for a total time period of 5 seconds. Continuation of pullout boundary conditions

beyond the mentioned total time results in instability of analysis. This can be attributed to the abrupt nature of failure once the bend region has failed. In this situation the bond on the tail cannot balance the pullout force no matter what the length of tail is. For meshes with 35M bars and minimum bend radius the variable mass scaling used gives a stable time increment of 0.004 seconds for all elements. The time increment used is 0.0004 seconds for a total time period of 5 seconds. For meshes with 35M bars and double minimum bend radius the mass scaling used gives a stable time increment of 0.002 seconds. The time increment used was 0.0004 seconds for a total time period of 5 seconds. For meshes with 45M bars and minimum bend radius the mass scaling used gives a stable time increment of 0.002 seconds. The time increment was 0.0004 seconds for the total time period of 5 seconds. For meshes with 45M bars and twice minimum bend radius the mass scaling used gives 0.002 seconds stable time increment. The time step was 0.0004 for total time period of 8.0 seconds.

7.5. Material Properties

The material model used for concrete is the damaged plasticity model. It accounts for both effects of nonlinear compression and tension. This is accomplished by incorporating a compression curve and tension softening curve into the model. In addition, Lubliner yield surface and Drucker-Prager plastic potential functions are used. Because of the monotonic nature of loading in these models damage parameters are not used. The compression and tension softening curves used are Saenz and Li et al. curves. The compression and tension softening curves are shown in figures (7.23) and (7.24). Steel stress-strain curve is shown in figure (7.25).

7.6. Analysis Results

Figures (7.26) to (7.32) show the stress-displacement curves for all models. These curves show the conditions for the beginning of the bend which is called lead here. As can be seen in figure (7.26) the behavior of different models with different tail lengths with 30M bars bent with minimum radius are very close.

Figure (7.27) shows that the capacity of a bent bar increases with increased bend radius. Figure (7.28) demonstrates the fact that by adding the straight development length required by the code the stress at the bar end becomes very close to yielding stress. Figure (7.29) shows that for 35M bars with different tail lengths and minimum bend radius the capacity remains the same. Figure (7.30) illustrates that 35M bars bent with twice minimum radius exhibit a much larger capacity. Figure (7.31) indicates that for 45M bars bent with minimum bent radius and different tail lengths there is little difference in pullout capacities. Figure (7.32) shows that with twice the minimum bend radius for 45M bars with different tail lengths the capacity increases remarkably and the one with $12d_b$ tail length exhibits a slightly larger capacity. This can be attributed to the large bend diameter of the bend which makes the bar exhibit some of the characteristics of straight bars. In other words, as the shape of the bar approaches that of a straight bar, the tail length becomes a more influential parameter.

Slippage tends to decrease from the beginning of the bend toward the end of the bend. It is worthwhile noting that the amount of slip becomes smaller as it proceeds through the tail. The slippage at the end of the tail is a very small value. Figure (7.33) shows a number of locations on the bar. These locations correspond to beginning, middle and the end of the bend region. Load-slip diagrams for the locations shown in figure (7.33) on the bar are given in figures (7.34) through (7.52). In these diagrams the load is presented as a fraction of the load necessary to yield the bar. These diagrams are presented to clarify the trend of slip at different locations on the bend region.

The diagrams in figures (7.34) to (7.52) also provide a means to make a comparison of slip trends for bars with the same diameter but different tail lengths. This kind of comparison is presented in figures (7.53) to (7.59). Comparison of slip values provides a deeper understanding of hook behavior. Figures (7.34) to (7.36) show that for 35M bars with minimum bend radius and different tail lengths slip at the beginning of the band is always larger than other

places on the bend region. The amount of slip decreases further through the middle to the end of the bend.

Figures (7.37) to (7.39) show that for 35M bars bent with twice minimum bend radius and different tail lengths slippage at location 283 is larger than the one at location 346 which in turn is larger than the slip at location 409. The peak load and the corresponding slip are larger than those in figures (7.34) to (7.36). Figures (7.37) to (7.39) also show that with increased tail length the amount of slip in the middle and end of the bar decrease slightly. Figures (7.40) to (7.52) exhibit the same general features mentioned above for 30M and 45M bars.

In Figures (7.53) to (7.59) the slip trend is shown along the length of the bend region with origin being the beginning of the bend. The slip values in diagrams (7.53) to (7.59) correspond to the peak load. Horizontal axes in these diagrams are in terms of bend length divided by the bend radius. It can be seen in these diagrams that for the same location of bend region, slip is slightly larger for hooks with smaller tails, however in general they are very close. Table (7.3) shows the slip values at different locations on the bend region corresponding to the peak load.

Overall, from figures (7.34) to (7.36) the peak load for cases 1 to 3 is 50 % of the yielding load. The slip values discussed from now on are values corresponding to the peak load. For case 1, the slips at the beginning, middle and end of bent region are 0.75 mm, 0.19 mm and 0.09 mm respectively. In case 2, slippage varies from 0.75 mm at the beginning to 0.17 mm in the middle to 0.09 mm at the end of the bend region. In case 3, the amount of slip at locations 283, 346 and 409 are 0.7 mm, 0.17 mm and 0.1 mm respectively. From figures (7.37) to (7.39) the peak load for cases 4 to 6 is eighty one percent of the yielding load. Case 4 exhibits slippages of 0.9 mm, 0.24 mm and 0.015 mm for locations 283, 346 and 409 respectively. Case 5 has a slippage of 0.9 mm for the beginning of the bend, 0.14 mm for the middle and 0.02 mm at the end. Case 6 shows a slip of 0.9 mm at

location 283, 0.108 mm at location 346 and 0.015 mm at location 409. From figures (7.40) to (7.42) the peak load for cases 7 to 9 is fifty six percent of the yielding load. For case 7, there is a slippage of 0.67 mm for location 283, 0.24 mm for location 346 and 0.08 mm for location 409. In case 8, slippages at the beginning, middle and end of the bend are 0.68 mm, 0.16 mm and 0.09 mm respectively. Case 9, shows slip values of 0.7 mm, 0.15 mm and 0.09 mm for locations 283, 346 and 409 respectively. From figures (7.43) to (7.45) the peak load for cases 10 to 12 is eighty percent of the yielding load. Case 10 exhibits a slippage of 0.95 mm at the beginning, 0.22 mm in the middle and 0.1 mm at the end of the bend. In case 11, slip varies from 0.83 mm at location 283 to 0.17 mm at location 346 to 0.04 mm at location 409. Case 12 slips at locations 283, 346 and 409 are 0.93 mm, 0.06 mm and 0.08 mm respectively. From figures (7.46) and (7.47) the peak load for cases 13 and 14 is forty four percent of the yielding load. From figure (7.48) the peak load for case 15 is forty seven percent of the yielding load. In case 13, there is a slippage of 0.89 mm at the beginning, 0.18 mm in the middle and 0.11 mm at the end of the bend region. In case 14, slippages at the beginning, middle, and end of bend are 0.8 mm, 0.15 mm and 0.09 mm respectively. In case 15, slips at locations 283, 346 and 409 are 0.8 mm, 0.13 mm and 0.05 mm respectively.

From figures (7.49) and (7.50) the peak load achieved for cases 16 and 17 is eighty one percent of the yielding load. From figure (7.51) the peak load for case 18 is ninety percent of the yielding load. Case 16 has slip values of 2 mm, 0.2 mm and 0.09 mm at the beginning, middle and end of the bend. Case 17, has a slippage of 1.68 mm at location 283, 0.13 mm at location 346 and 0.07 mm at location 409. The amounts of slip at the beginning, middle and end of the bend for case 18 are 1.66 mm, 0.04 mm and 0.03 mm respectively. From figure (7.52) the peak load for case 19 is approximately the yielding load. Case 19, shows slip values of 0.03 mm, 0.02 mm and 0.01 mm for locations 283, 346 and 409 respectively.

7.7. Comparison with Code and Conclusions

In this section an evaluation of CSA-A23.3 code provisions with respect to capacity of hooked bars is presented. In figure (7.60), two 90 degree standard hooks are schematically shown. Every hook is composed of a straight part, a bent part and a tail. Hooks in figure (7.60) are illustrated with the bend radii of r and $2r$. Based on the code, the hook development length does not depend on the bend radius and, therefore, is the same for the two hooks illustrated in figure (7.60). The equation of A23.3 for hook development length using 400 MPa steel is as follows:

$$l_{dh} = \frac{100 d_b}{\sqrt{f'_c}} \tag{7.1}$$

Here, d_b and f'_c denote bar diameter and strength of concrete respectively. The value of l_{dh} for 30 MPa concrete and 30M bars equals 546 mm. Equation (7.1) implies that the increase in the bend region capacity is proportional to the bend radius increase. In other words, a radius of bend increased by r will result in an increased capacity of the bend region equal to the capacity of a straight bar with length r. Thus, the contribution of the bent region with the radius of $2r$ compared to the one with the radius of r is larger by a value of $\left(\frac{r}{l_d} \times f_y\right)$ with l_d being the straight development length and f_y the yielding stress of reinforcement. This conclusion is based on the straight development length equation in A23.3 which implies that the stress in reinforcement is proportional to the length of the bar. In other words, if the straight development length is reduced by say fifty percent the stress in the bar is also reduced by fifty percent. The code equation with regard to straight length development is presented as follows:

$$l_d = 1.15 \frac{k_1 k_2 k_3 k_4}{d_{cs} + K_{tr}} \frac{f_y}{\sqrt{f'_c}} A_b \tag{7.2}$$

Where, $k_1, k_2, k_3, k_4, K_{tr}, A_b$ and d_{cs} present water accumulation coefficient, coating coefficient, density coefficient, bar size coefficient, stirrup coefficient, area of bar cross-section and the distance from closest concrete surface to the

center of the bar or two thirds of center to center distance of bars whichever is smaller. In this work, coefficients k_1 to k_4 are taken equal to 1.0 because there is no water accumulation considered in analysis, there is no coating on bars, only normal density concrete is considered and bar sizes are large. Stirrup coefficient is zero here since there are no stirrups in these models. Here, the parameter d_{cs} equals $2d_b$.

The code approach to hooked bars neglects the effect of normal stresses on the bent region and, therefore, a larger increase in the capacity of this region is predicted. To verify this prediction the analyses in the preceding section were carried out. Table (7.4) is derived according to the results from analysis.

From the analysis results and the table 7.4, it becomes clear that the capacity of bend region increases due to an increase in the bend radius and this increase is 2.35 to 3.18 times more than what the code predicts. Therefore, the application of a hook with a radius twice the minimum is conservative in all cases. Furthermore, usage of a hook with 45M bar and minimum bend radius is un-conservative and is not recommended. On the other hand a 45M bar bent with a radius twice the minimum results in a conservative hook and hence it is recommended to use this radius of bend for 45M bar.

For 30M bars the code based bend capacity for minimum and twice minimum bend radii are 231.22 MPa and 271.72 MPa respectively. This implies that the improvement due to the increase in bend radius is 40.5 MPa. However, the finite element based bend capacities for minimum and twice minimum bend radii are 225 MPa and 320 MPa respectively. It means the improvement due to bend capacity is 95 MPa which is 2.35 times larger than the code based prediction of improvement.

For 35M bars the code based bend capacity for minimum and twice minimum bend radii are 228.9 MPa and 272.4 MPa. Therefore, the code based improvement

corresponding to the increase in the bend radius is 43.5 MPa. However, the bend capacities for minimum and twice minimum bend radii based on finite element analysis are approximately 200 MPa and 325 MPa. It means the finite element based improvement due to the bend radius increase is 125 MPa which is 2.87 time larger than the code based prediction.

For 45M bars the bend region capacities for minimum and twice minimum bend radii according to the code are 250.42 MPa and 304.42 MPa. This implies that the increase in the bend capacity due to the bend radius increase is 54 MPa. However, according to finite element analysis the bend capacity for 45M bar and minimum bend radius for tail lengths of $12d_b$, $8d_b$ and $4d_b$ are 188 MPa, 176 MPa and 176 MPa respectively. From finite element analysis, the bend region capacities for 45M bars bent with twice minimum radius and tail lengths of $12d_b$, $8d_b$ and $4d_b$ are 360 MPa, 324 MPa and 324 MPa. Thus, the improvement in capacity corresponding to the bend radius increase for tail lengths of $12d_b$, $8d_b$ and $4d_b$ based on finite element analysis are 172 MPa, 148 MPa and 148 MPa respectively. These values show that for 45M bars the improvement due to bend radius increase according to finite element analysis for tail lengths of $12d_b$, $8d_b$ and $4d_b$ are 3.18, 2.74 and 2.74 times larger than those predicted by the code respectively.

Concerning the minimum bend radius, Table (7.4) shows that finite element results and code predictions for the bend region capacity are close for all cases except the ones involving 45M bars. In other words, the code predicted capacities for 45M bars bent with the minimum radius is much more than what the finite element analysis predicts and hence they are not conservative. On the other hand, provisions of code for 35M and 30M bar are adequate but can be improved by using a radius of bend equal to twice the minimum bend radius. In addition, according to the results of analysis there is not much difference in capacity between tail lengths of $4d_b$, $8d_b$ and $12d_b$. In Table (7.4), the bend region

capacities are calculated by subtraction of the straight region capacities from f_y. The straight region capacities are obtained from equation (7.2). This approach is presented in the following relationship:

$$C_{bend} = f_y - \frac{l_{dh} - r - d_b}{l_d} f_y \tag{7.3}$$

Where, C_{bend} is the bend region capacity in MPa. To further validate this approach, the case of 30M bar with full code based hook development length has been studied in case 19 of this chapter. This analysis shows that using equation (7.2) gives a good approximation for the computation of straight region capacity since with the addition of the bonded straight part required by the code the capacity of the hooked bar becomes almost equal to the yield stress. As a conclusion, in order to have a conservative design the following equation is recommended to be used to determine the bend radius:

$$r = \begin{cases} r_{\min} & d_b \le 35 \\ \frac{r_{\min}}{10}(d_b - 25) & 35 \le d_b \le 45 \end{cases} \tag{7.4}$$

Here, $r_{\min}$ is the minimum bend radius. Equation (7.4) gives a conservative hook design. However, there may be other more economical options that need to be further investigated as a future research topic. The capacity of the models did not change much with different tail lengths. However, tail lengths shorter than twelve times the bar diameter are not recommended. This is because there is a possibility for a short tail to pop out of the joint region due to a small amount of concrete cover at the back of the hook.

Case	Bar Diameter (mm)	f'_c (MPa)	Bend Radius (mm)	Tail Length	Bonded Straight Length
1	35	30	125*	$4d_b$	0
2	35	30	125*	$8d_b$	0
3	35	30	125*	$12d_b$	0
4	35	30	250	$4d_b$	0
5	35	30	250	$8d_b$	0
6	35	30	250	$12d_b$	0
7	30	30	100*	$4d_b$	0
8	30	30	100*	$8d_b$	0
9	30	30	100*	$12d_b$	0
10	30	30	200	$4d_b$	0
11	30	30	200	$8d_b$	0
12	30	30	200	$12d_b$	0
13	45	30	200*	$4d_b$	0
14	45	30	200*	$8d_b$	0
15	45	30	200*	$12d_b$	0
16	45	30	400	$4d_b$	0
17	45	30	400	$8d_b$	0
18	45	30	400	$12d_b$	0
19	30	30	100*	$12d_b$	$l_{dh} - r - d_b$

* Minimum Bend Radii

Table (7.1) – Cases to be Studied

Case	Width (mm)	Height (mm)	Length (mm)	Tail Length (mm)	Unbonded Length (mm)
1	212.5	648	680	140	520
2	212.5	648	680	280	520
3	212.5	648	680	420	520
4	212.5	773	805	140	520
5	212.5	773	805	280	520
6	212.5	773	805	420	520
7	200	558	590	120	460
8	200	558	590	240	460
9	200	558	590	360	460
10	200	658	690	120	460
11	200	658	690	240	460
12	200	658	690	360	460
13	237.5	853	885	180	640
14	237.5	853	885	360	640
15	237.5	853	885	540	640
16	237.5	1053	1085	180	640
17	237.5	1053	1085	360	640
18	237.5	1053	1085	540	640
19	200	558	646	360	0

Table (7.2) – Mesh Dimensions

Case	Slip at Peak at 283 (mm)	Slip at Peak at 346 (mm)	Slip at Peak at 409 (mm)
1	0.75	0.19	0.09
2	0.75	0.17	0.09
3	0.7	0.17	0.1
4	0.9	0.24	0.015
5	0.9	0.14	0.02
6	0.9	0.108	0.015
7	0.67	0.24	0.08
8	0.68	0.16	0.09
9	0.7	0.15	0.09
10	0.95	0.22	0.1
11	0.83	0.17	0.04
12	0.93	0.06	0.08
13	0.89	0.18	0.11
14	0.8	0.15	0.09
15	0.8	0.13	0.05
16	2	0.2	0.09
17	1.68	0.13	0.07
18	1.66	0.04	0.03
19	0.03	0.02	0.01

Table (7.3) – Slip at Different Bend Locations

Bar Size (mm)	Tail Length	Bend Radius (mm)	Bend Capacity From Code (Mpa)	Bend Capacity from FE (Mpa)	Improvement Based on Code (Mpa)	Improvement Based on FE (Mpa)	Comments on Code Based on Capacity
30	$12d_b$	100	231.22	225	0	0	Adequate
30	$8d_b$	100	231.22	225	0	0	Adequate
30	$4d_b$	100	231.22	225	0	0	Adequate
30	$12d_b$	200	271.72	320	40.5	95	Conservative
30	$8d_b$	200	271.72	320	40.5	95	Conservative
30	$4d_b$	200	271.72	320	40.5	95	Conservative
35	$12d_b$	125	228.90	200	0	0	Adequate
35	$8d_b$	125	228.90	200	0	0	Adequate
35	$4d_b$	125	228.90	200	0	0	Adequate
35	$12d_b$	250	272.40	325	43.5	125	Conservative
35	$8d_b$	250	272.40	325	43.5	125	Conservative
35	$4d_b$	250	272.40	325	43.5	125	Conservative
45	$12d_b$	200	250.42	188	0	0	Unconservative
45	$8d_b$	200	250.42	176	0	0	Unconservative
45	$4d_b$	200	250.42	176	0	0	Unconservative
45	$12d_b$	400	304.42	360	54	172	Conservative
45	$8d_b$	400	304.42	324	54	148	Conservative
45	$4d_b$	400	304.42	324	54	148	Conservative

Table (7.4) – Summary of Results and Conclusions

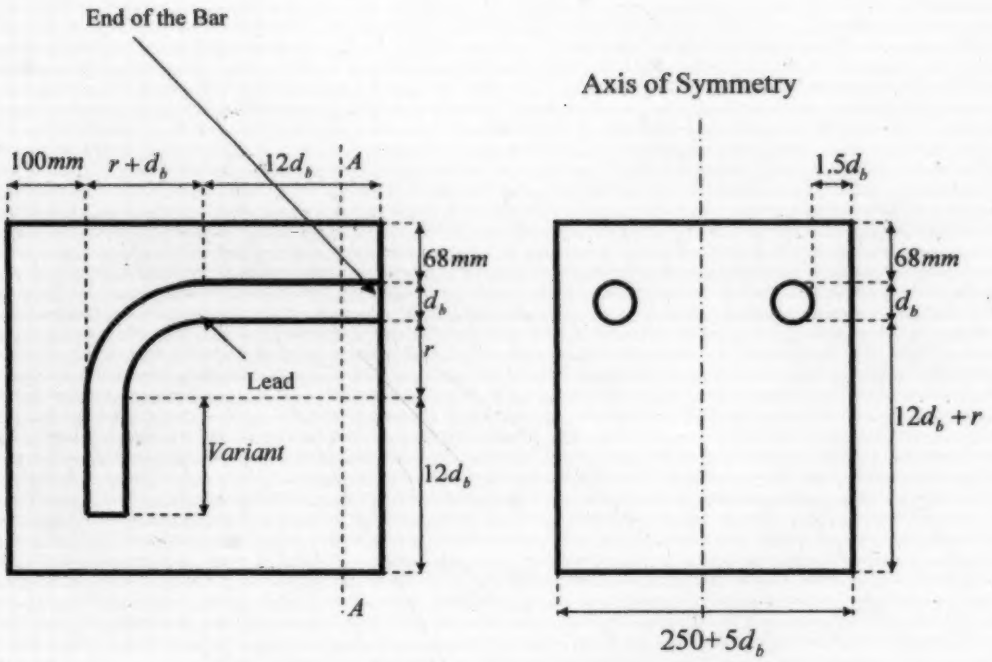

Figure (7.1) – Schematic Drawing of Models Studied

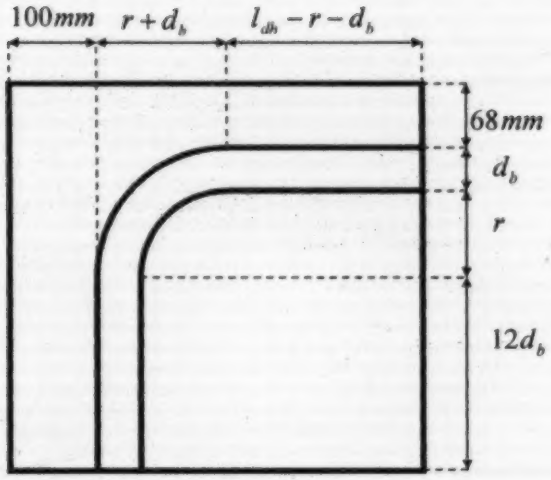

Figure (7.2) – Schematic Drawing of the Model with Full Hook Development Length

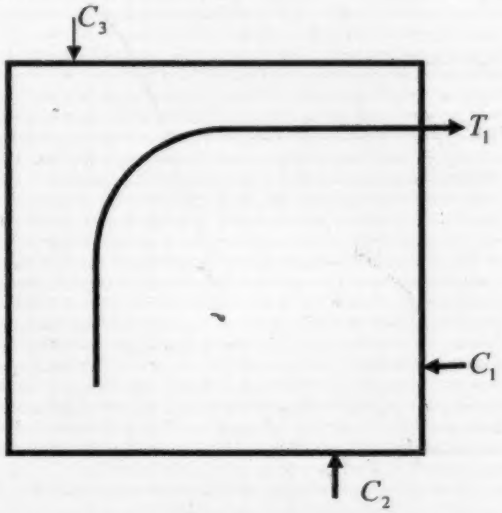

Figure (7.3) – Schematic Drawing of the Loads

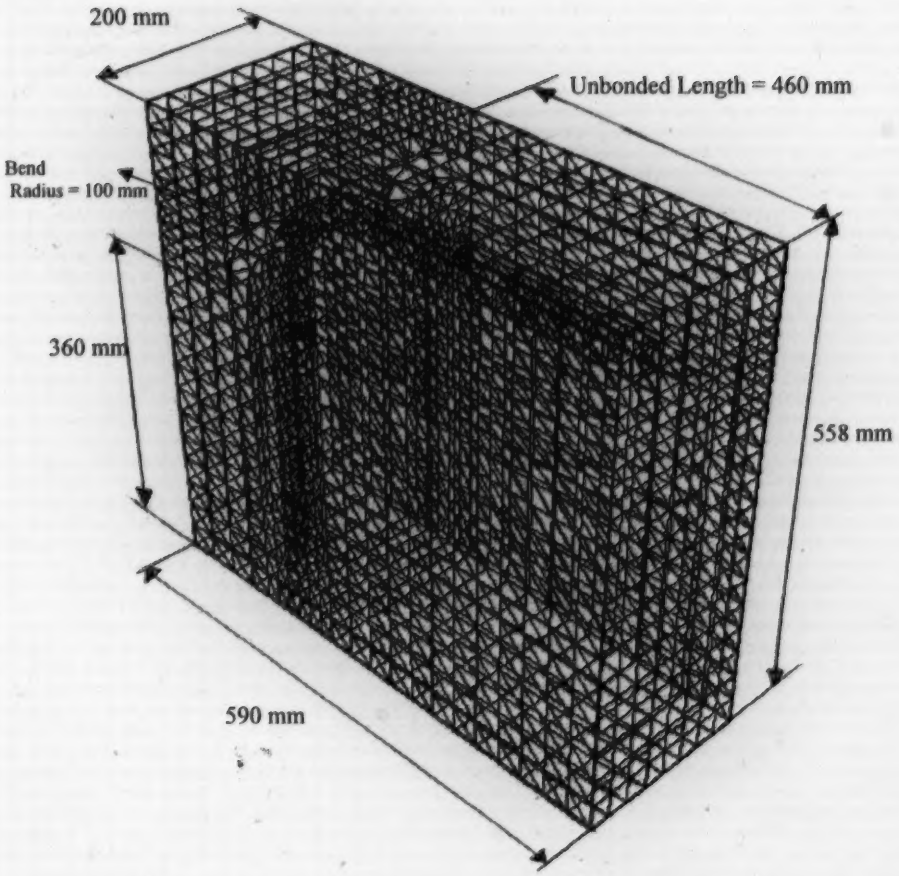

Figure (7.4) - FE Mesh for 30M bar with 100 mm bend radius and 12 d_b tail

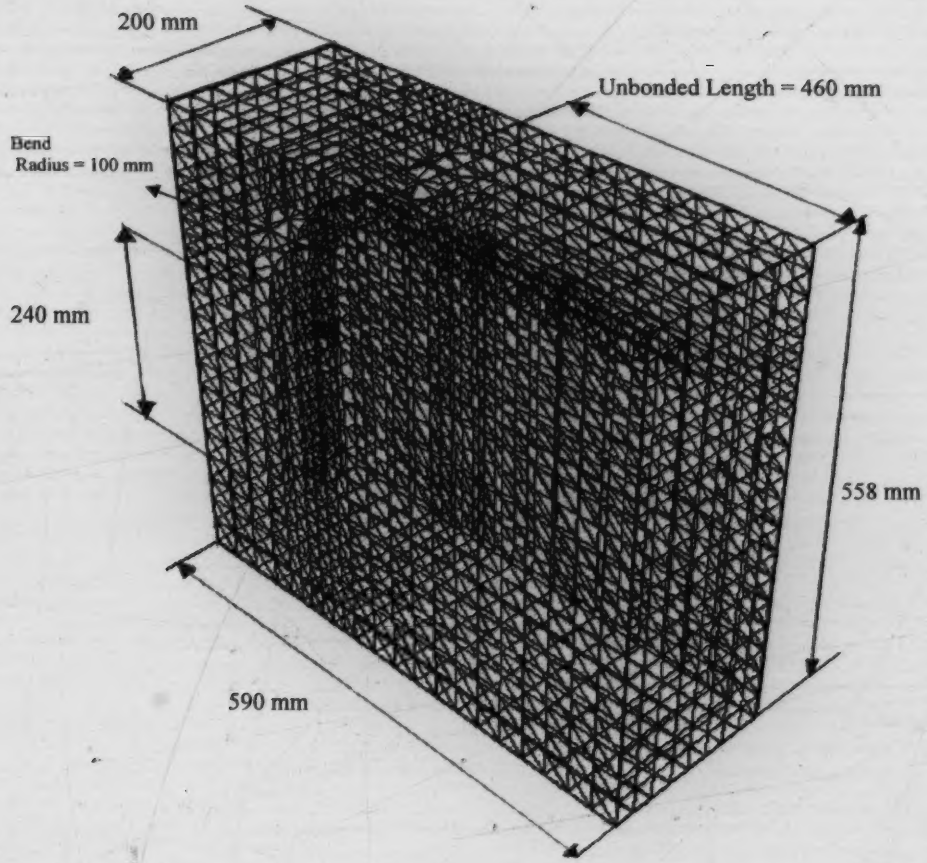

Figure (7.5) - FE Mesh for 30M bar with 100 mm bend radius and 8 d_b tail

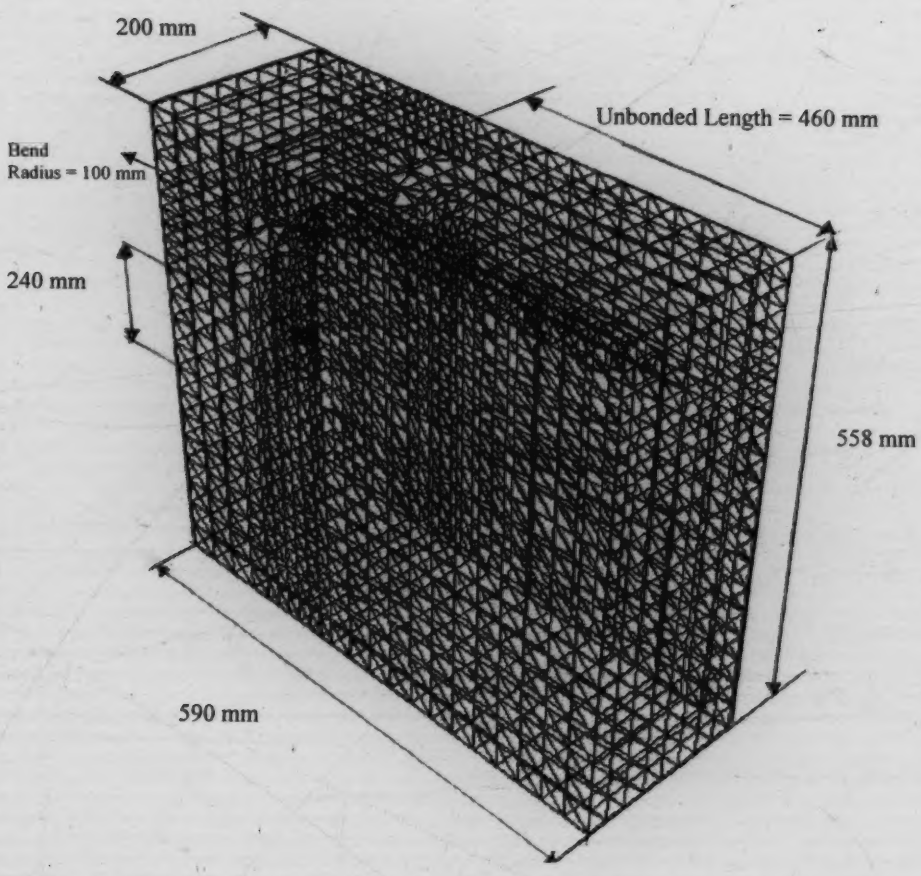

Figure (7.6) - FE Mesh for 30M bar with 100 mm bend radius and 4 d_b tail

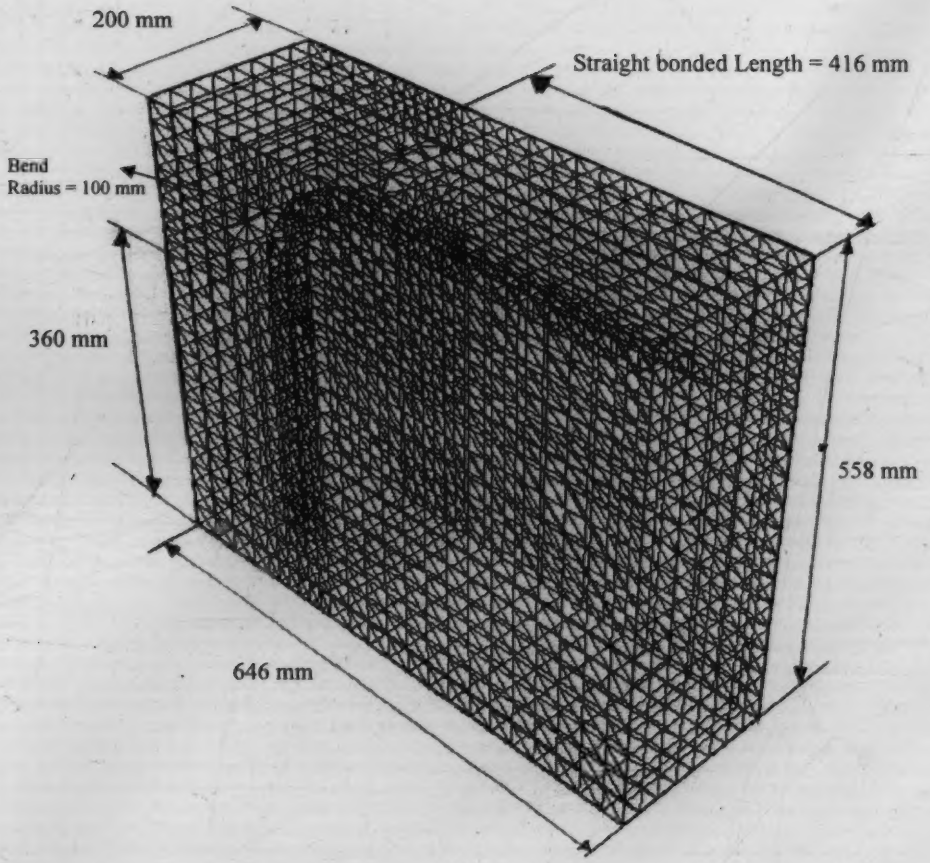

Figure (7.7) - FE Mesh for 30M bar with 100 mm bend radius,12 d_b tail and straight bonded length of l_d

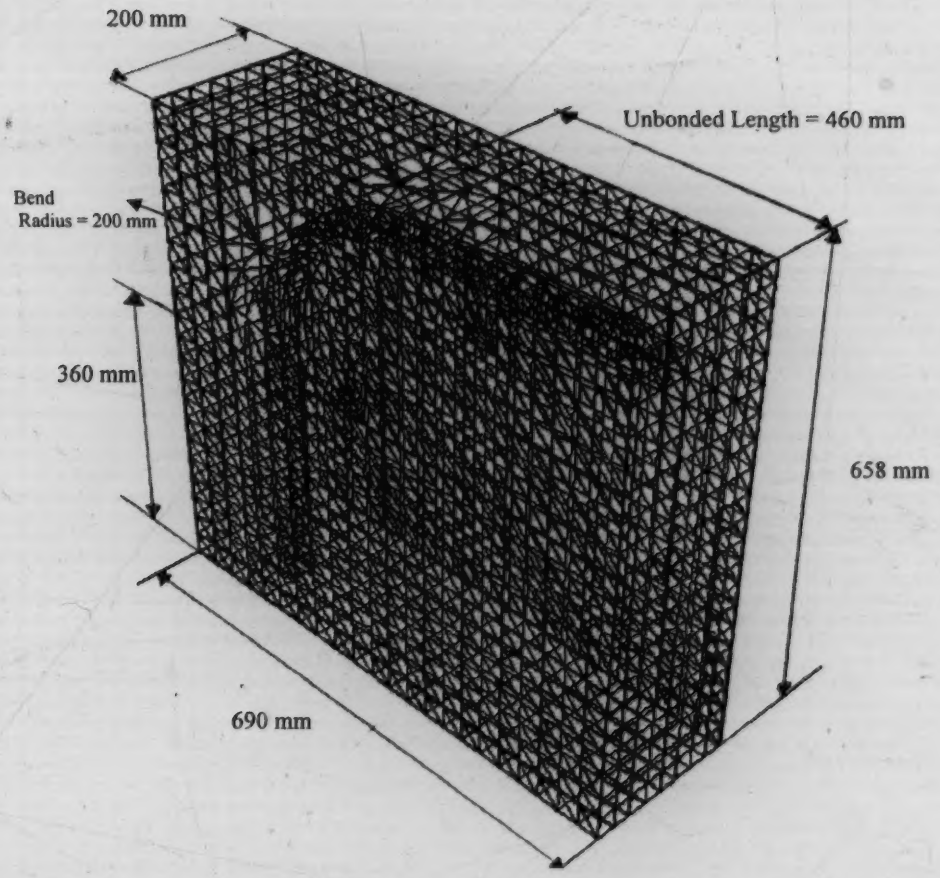

Figure (7.8) - FE Mesh for 30M bar with 200 mm bend radius and $12\,d_b$ tail

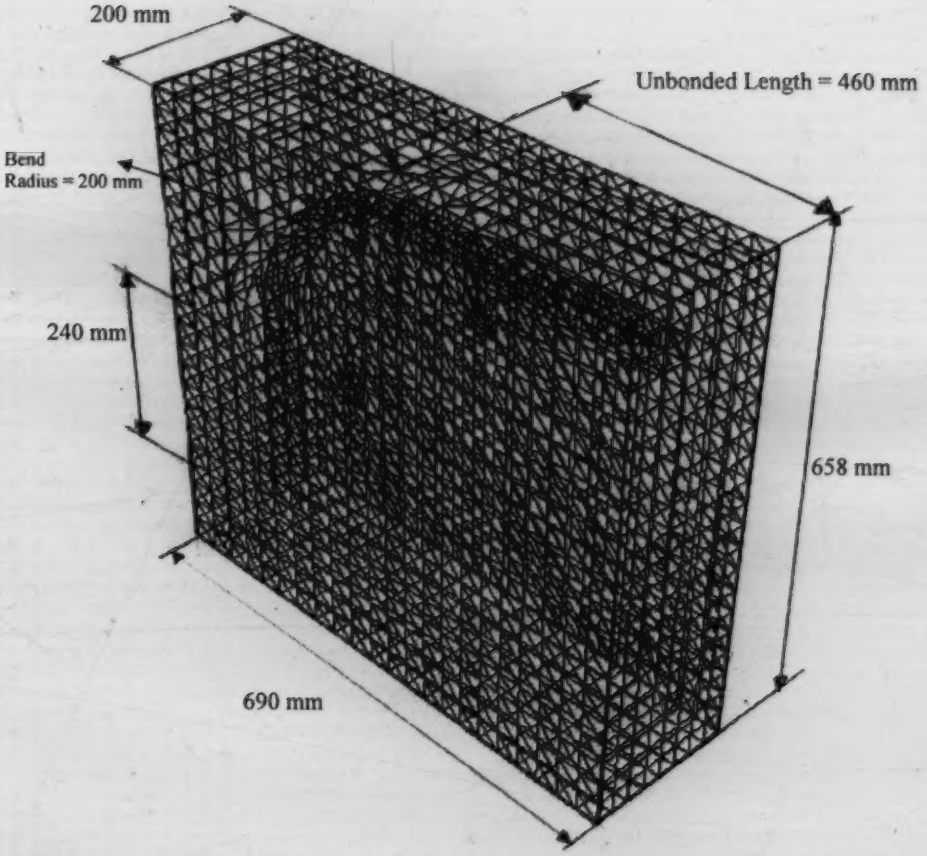

Figure (7.9) - FE Mesh for 30M bar with 200 mm bend radius and 8 d_b tail

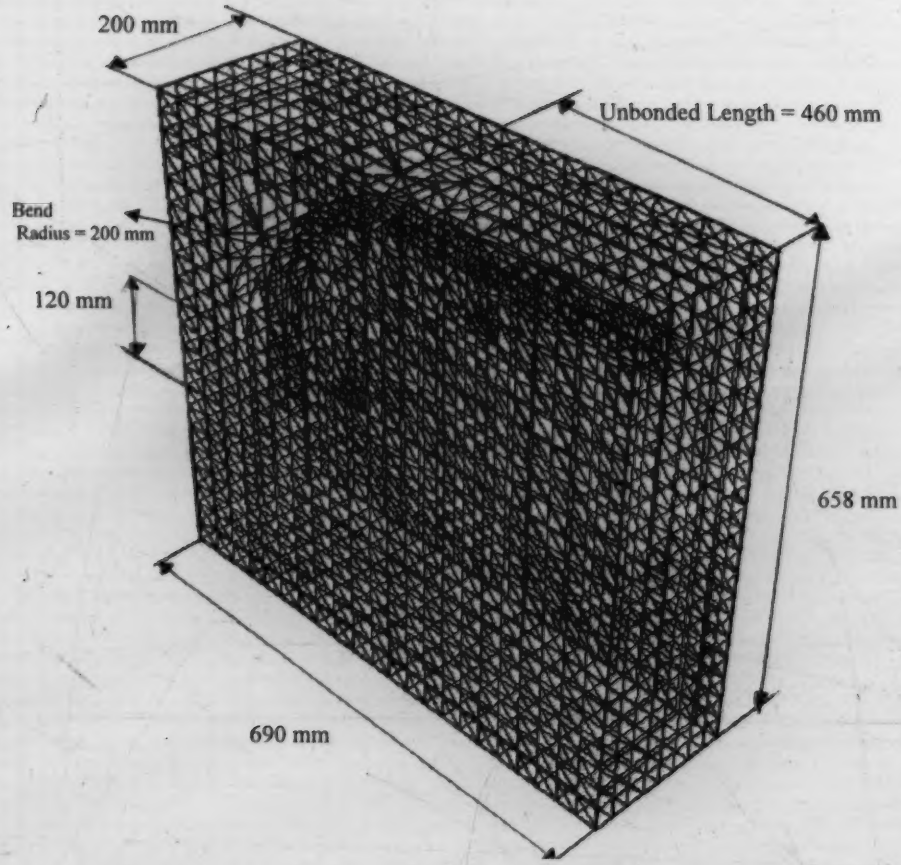

Figure (7.10) - FE Mesh for 30M bar with 200 mm bend radius and 4 d_b tail

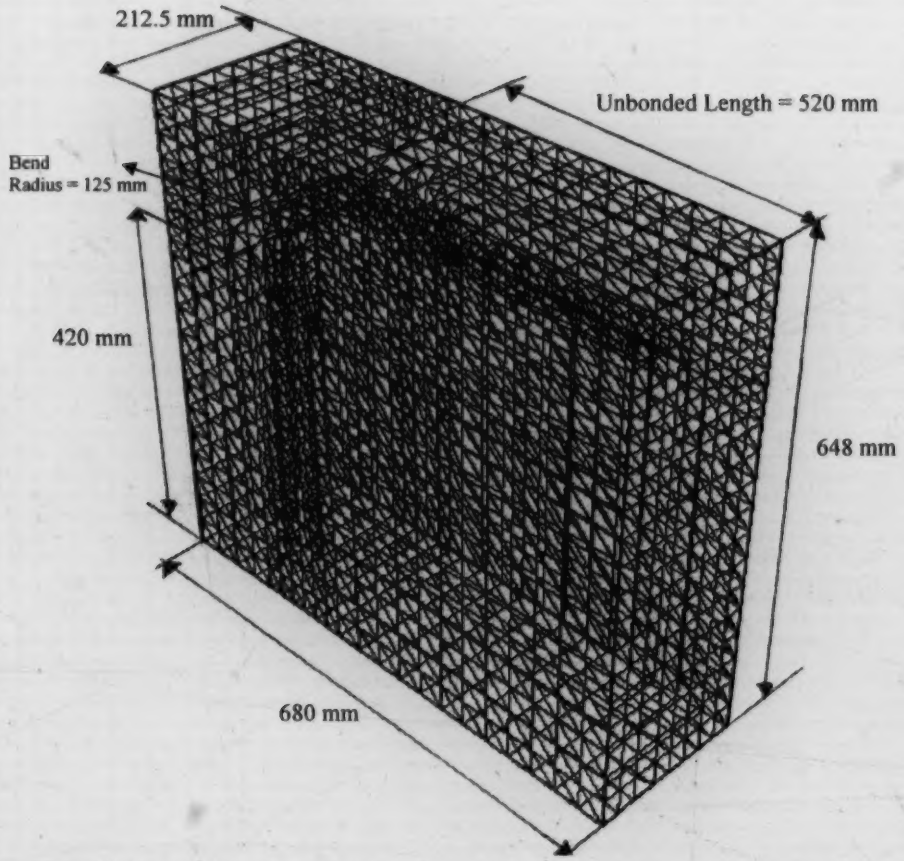

Figure (7.11) - FE Mesh for 35M bar with 125 mm bend radius and 12 d_b tail

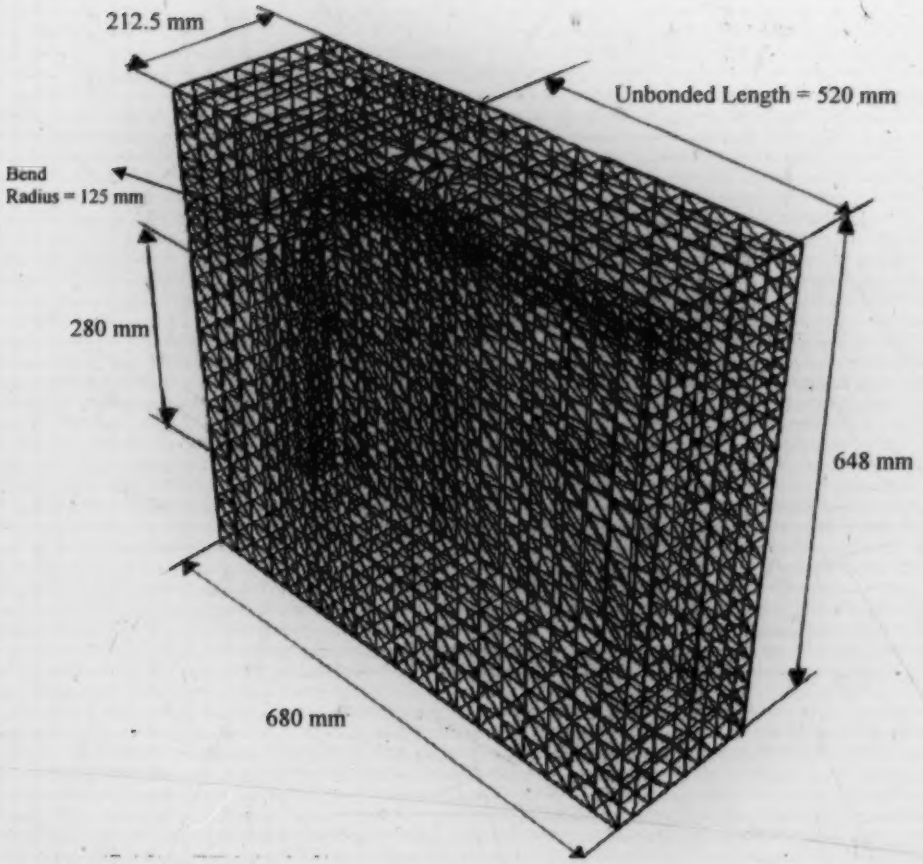

Figure (7.12) - FE Mesh for 35M bar with 125 mm bend radius and 8 d_b tail

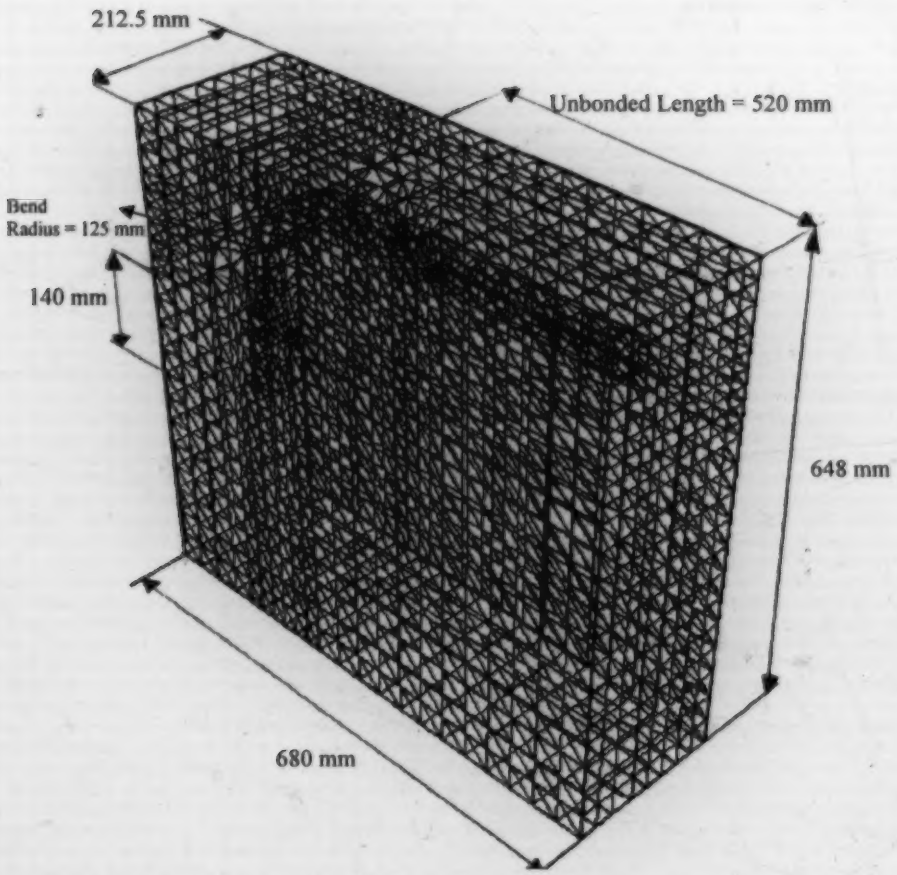

Figure (7.13) - FE Mesh for 35M bar with 125 mm bend radius and 4 d_b tail

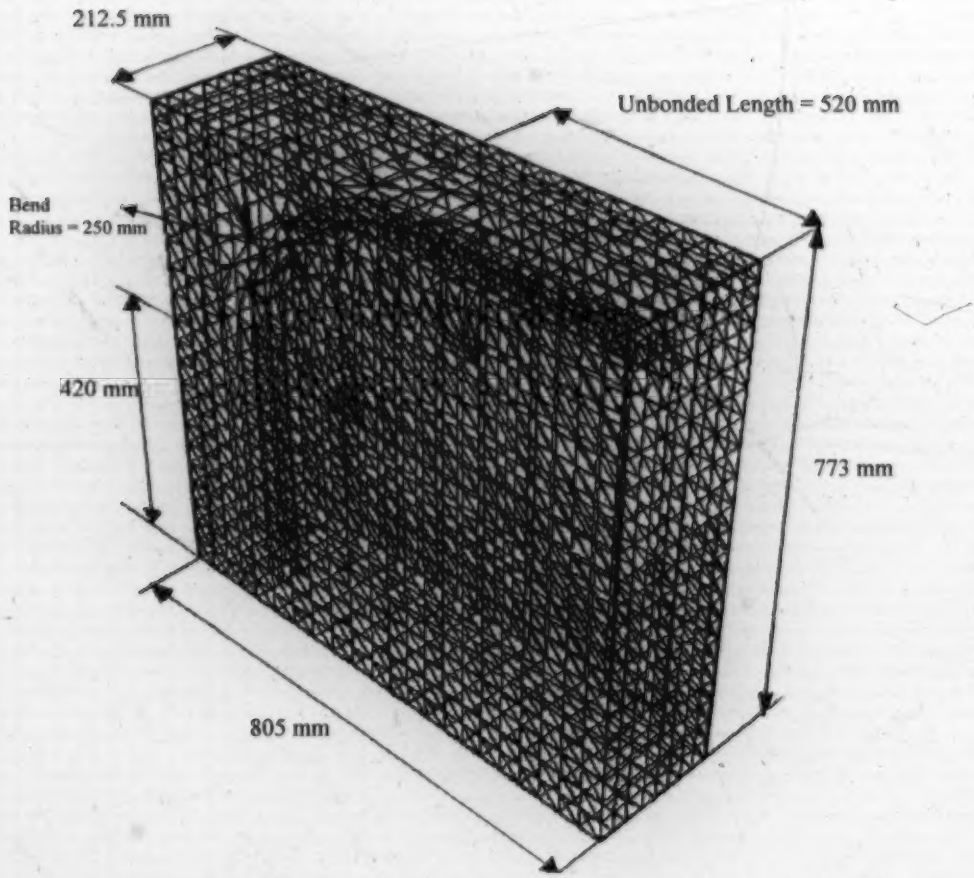

Figure (7.14) - FE Mesh for 35M bar with 250 mm bend radius and 12 d_b tail

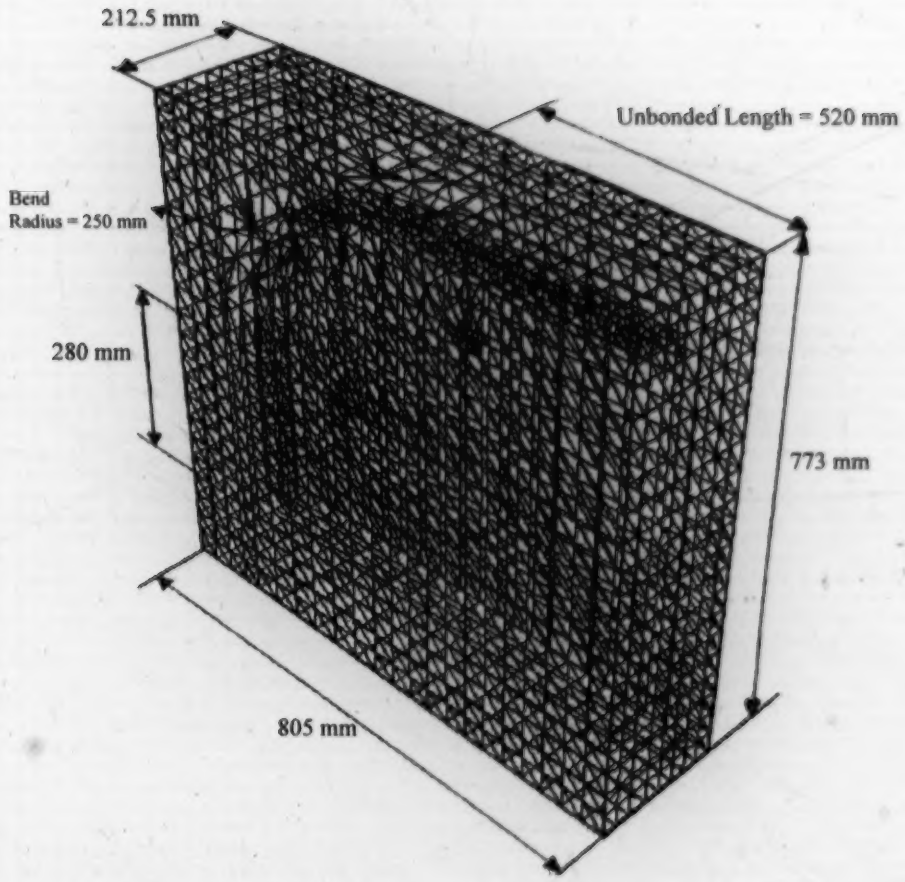

Figure (7.15) - FE Mesh for 35M bar with 250 mm bend radius and 8 d_b tail

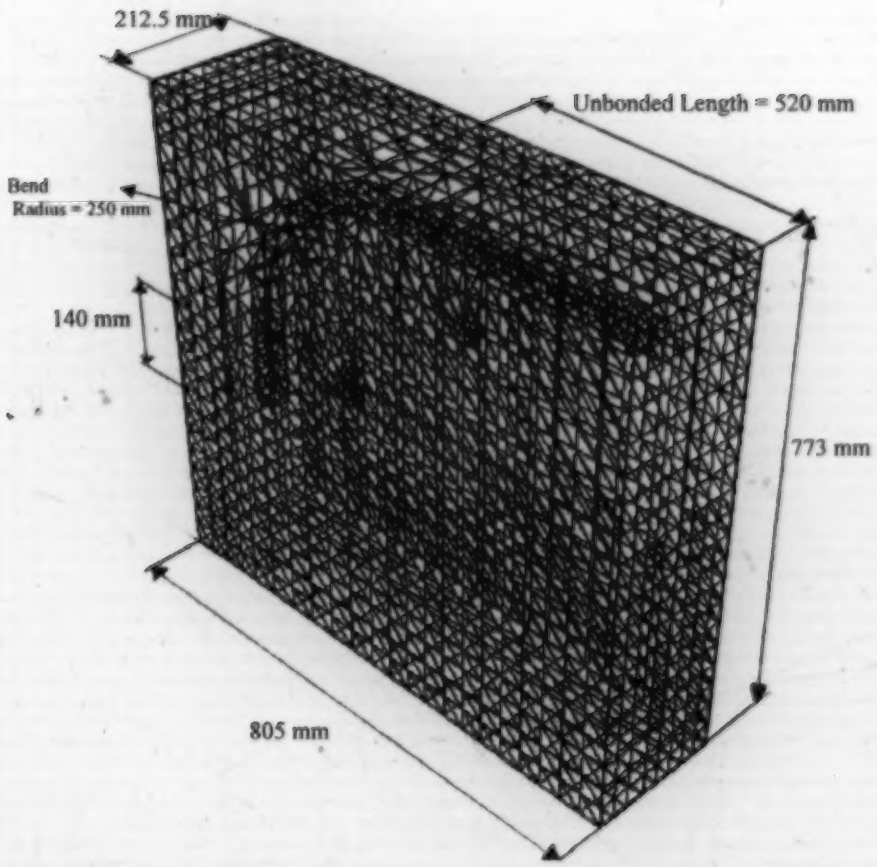

Figure (7.16) - FE Mesh for 35M bar with 250 mm bend radius and 4 d_b tail

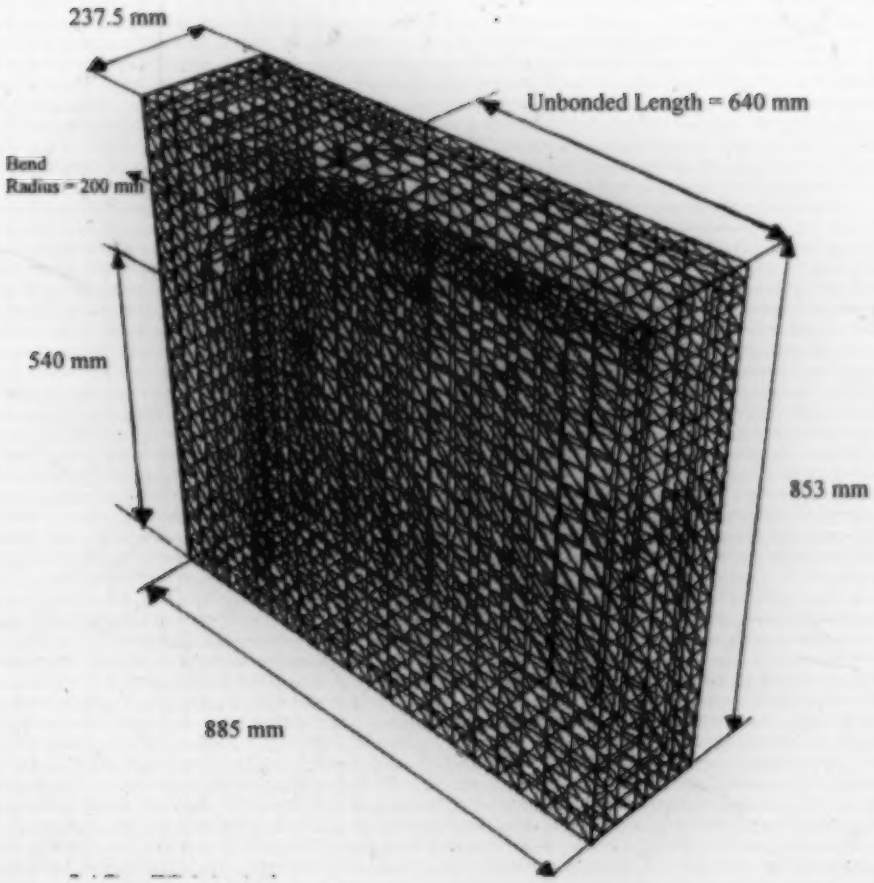

Figure (7.17) - FE Mesh for 45M bar with 200 mm bend radius and 12 d_b tail

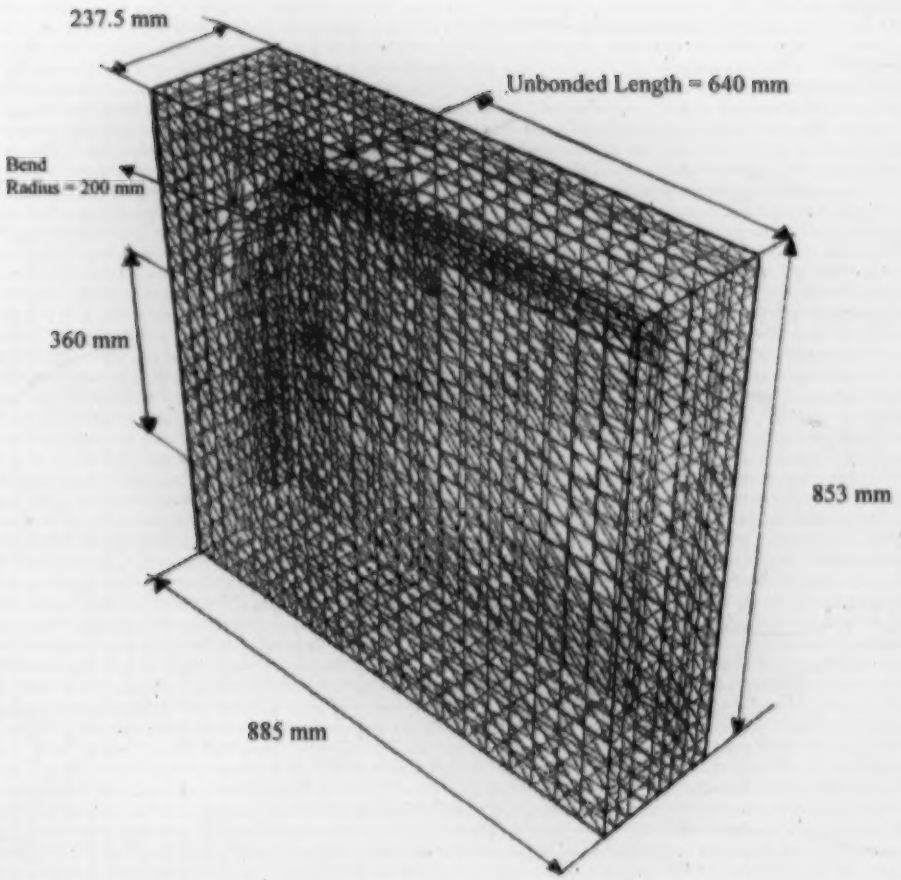

Figure (7.18) - FE Mesh for 45M bar with 200 mm bend radius and 8 d_b tail

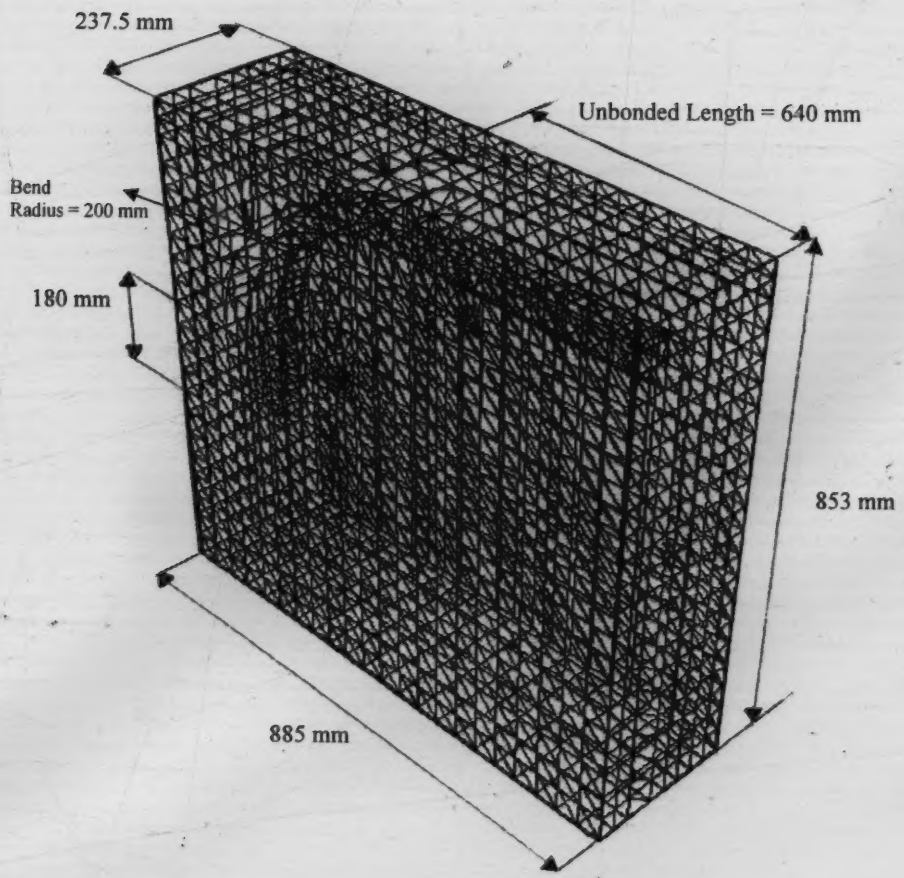

Figure (7.19) - FE Mesh for 45M bar with 200 mm bend radius and 4 d_b tail

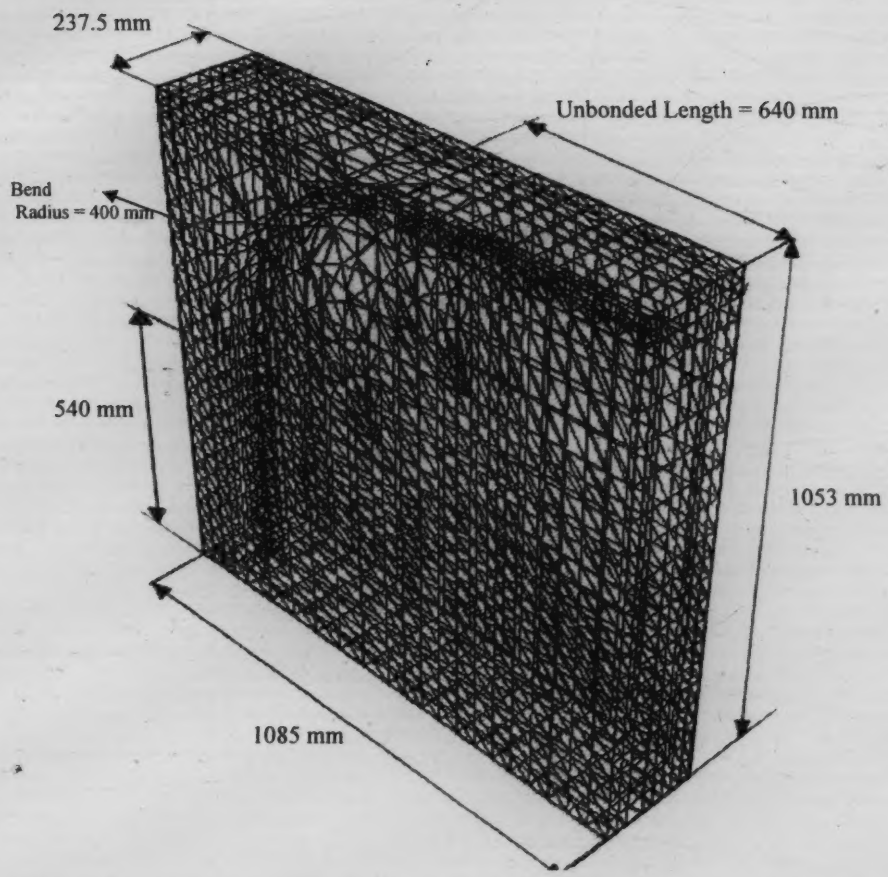

Figure (7.20) - FE Mesh for 45M bar with 400 mm bend radius and 12 d_b tail

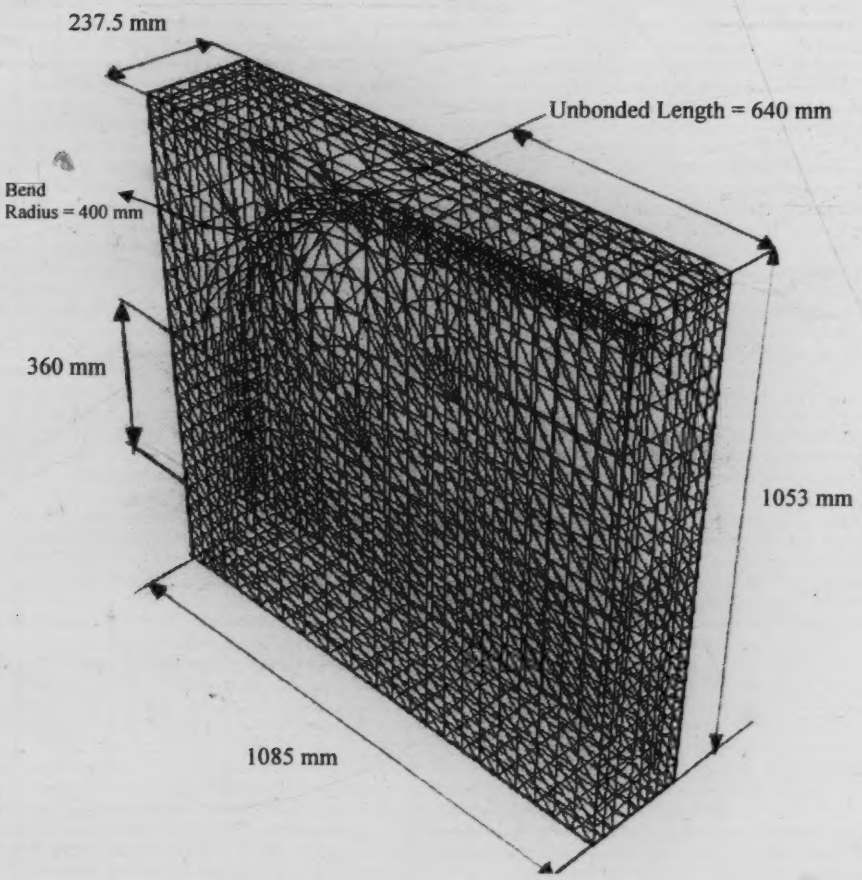

Figure (7.21) - FE Mesh for 45M bar with 400 mm bend radius and 8 d_b tail

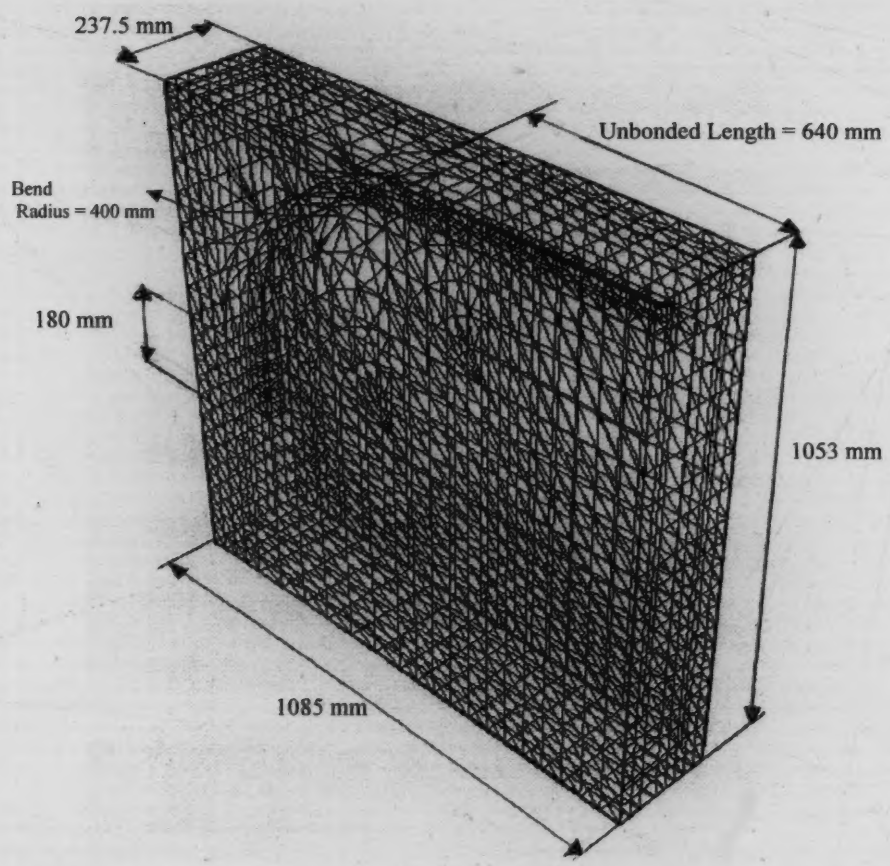

Figure (7.22) - FE Mesh for 45M bar with 400 mm bend radius and 4 d_b tail

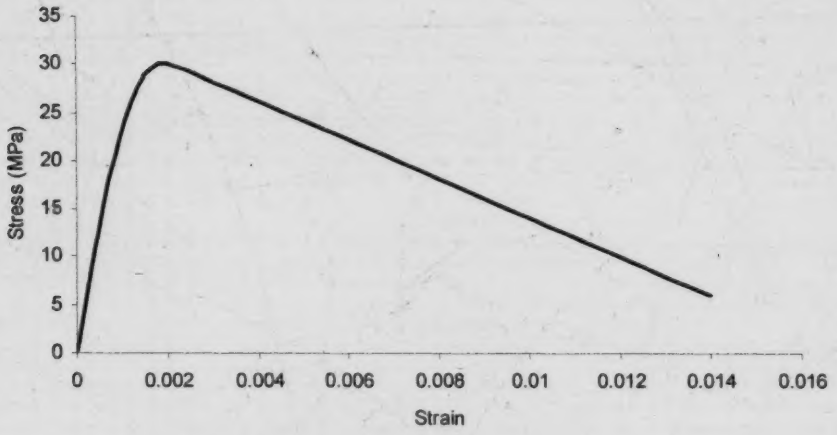

Figure (7.23) – Compression Curve

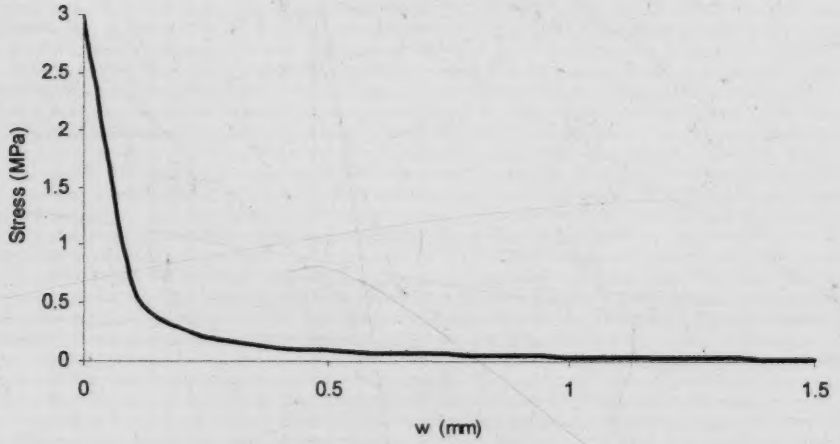

Figure (7.24) – Tension Softening Curve

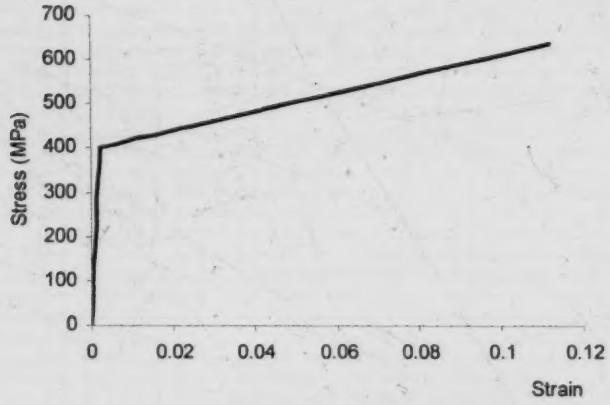

Figure (7.25) – Steel Stress-Strain Diagram

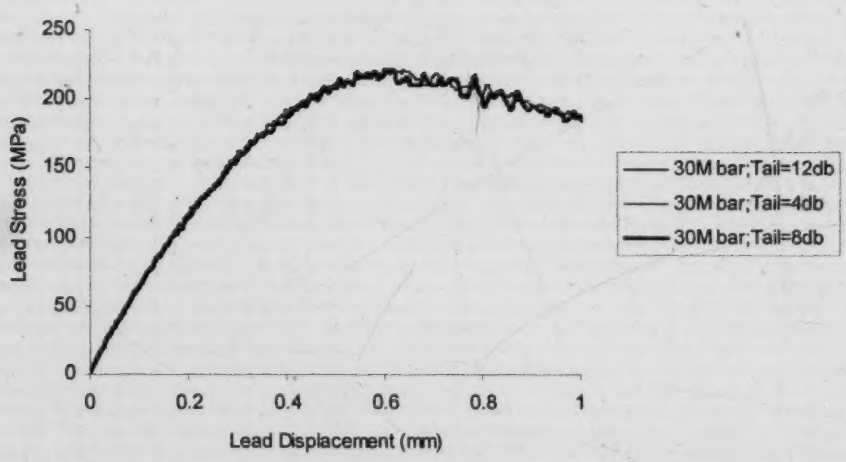

Figure (7.26) – Load-displacement for 30M bar and minimum bend radius

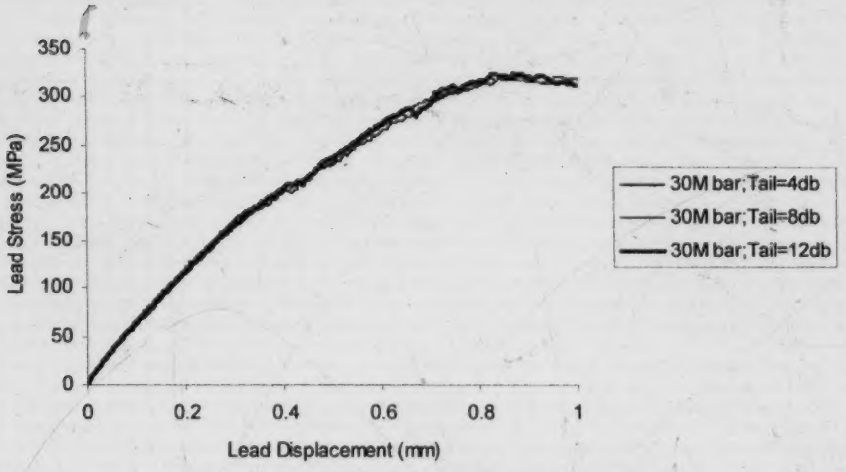

Figure (7.27) – Load-displacement for 30M bar and twice minimum bend radius

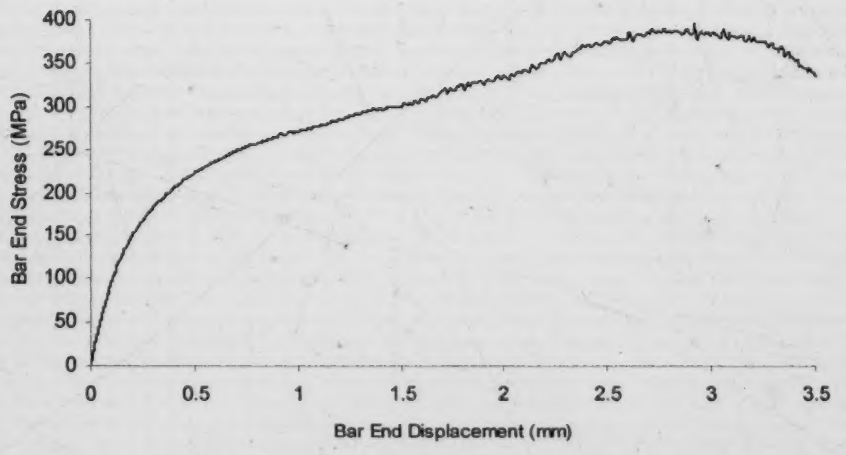

Figure (7.28) – Load-displacement for 30M bar, minimum bend radius and straight development length of l_d

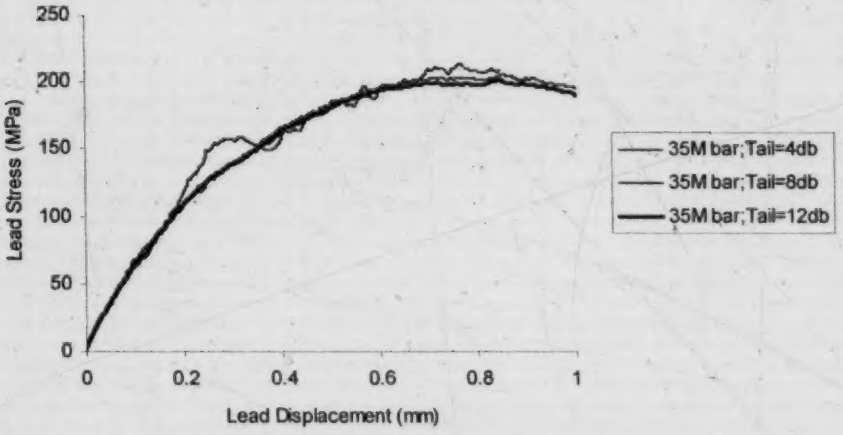

Figure (7.29) – Load-displacement for 35M bar and minimum bend radius

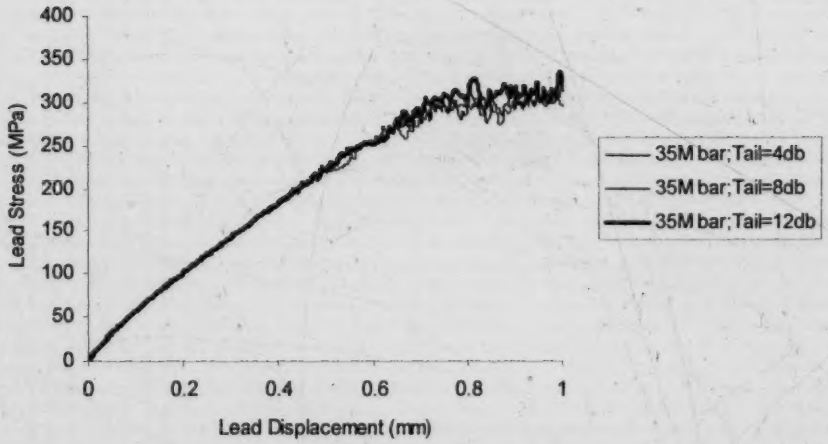

Figure (7.30) – Load-displacement for 35M bar and twice minimum bend radius

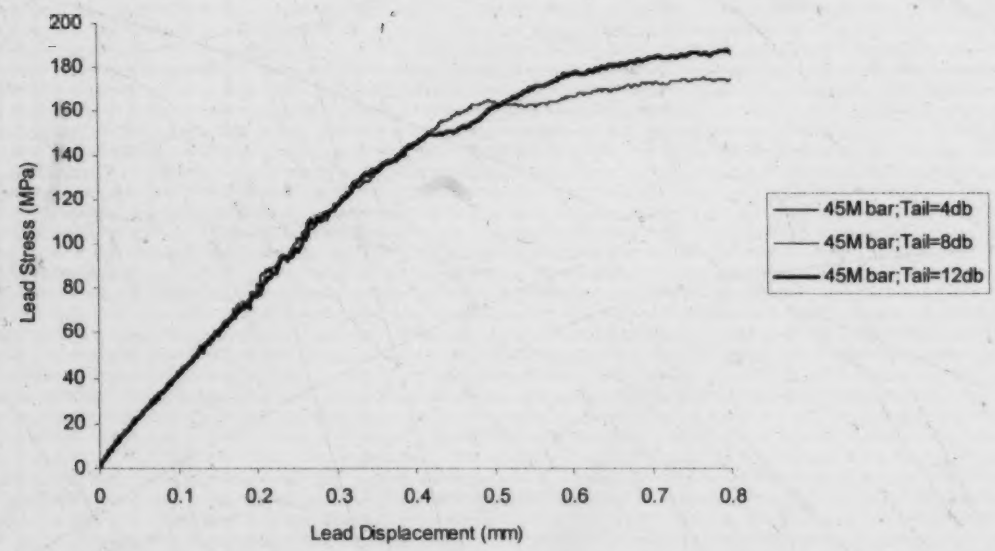

Figure (7.31) – Load-displacement for 45M bar and minimum bend radius

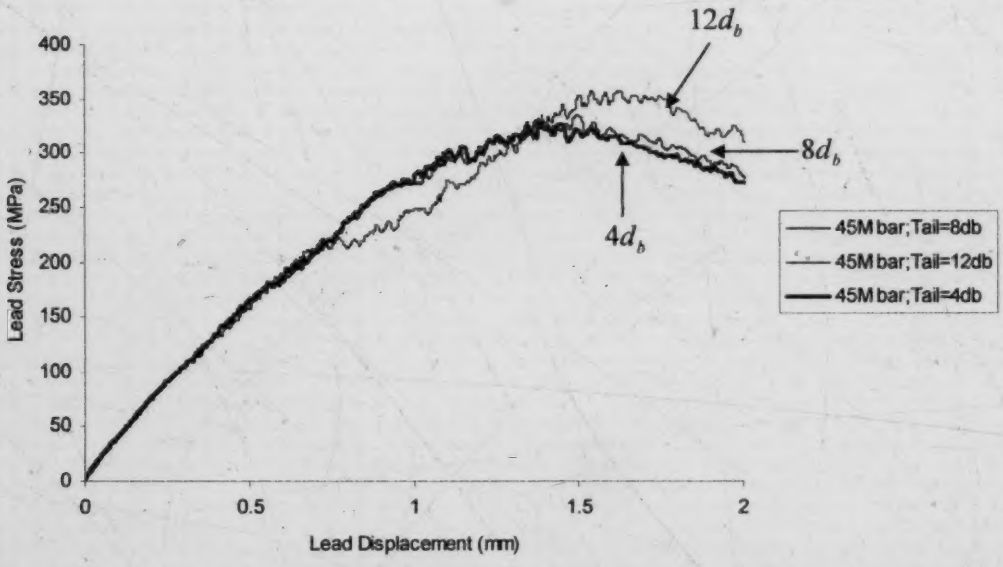

Figure (7.32) – Load-displacement for 45M bar and twice minimum bend radius

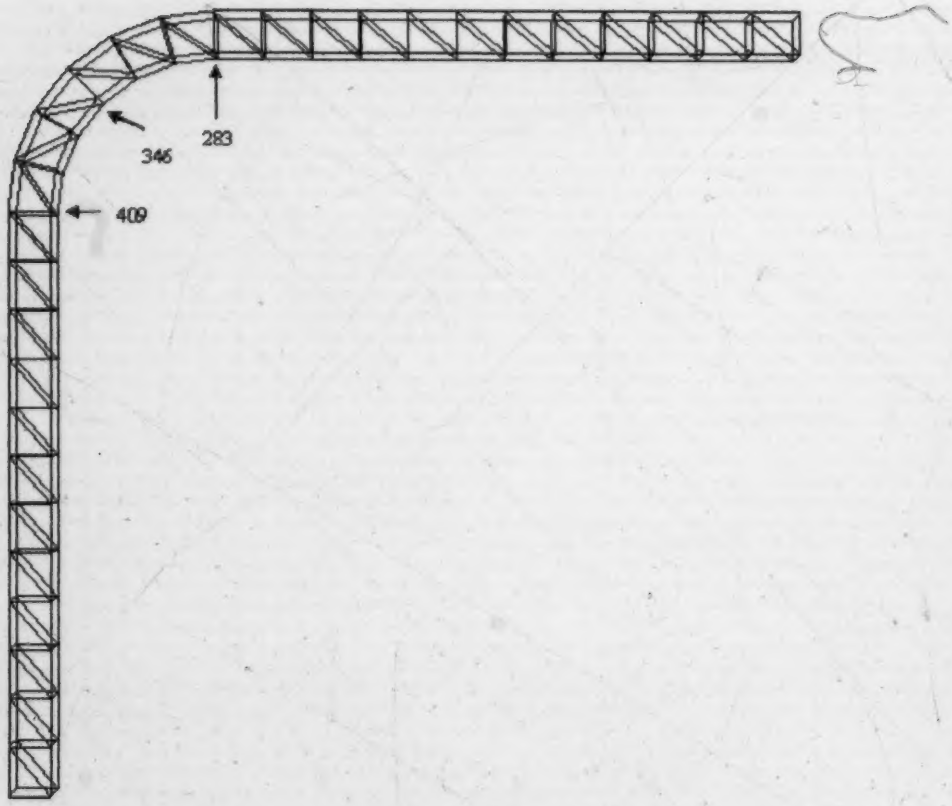

Figure (7.33) – Different Locations on the Bar

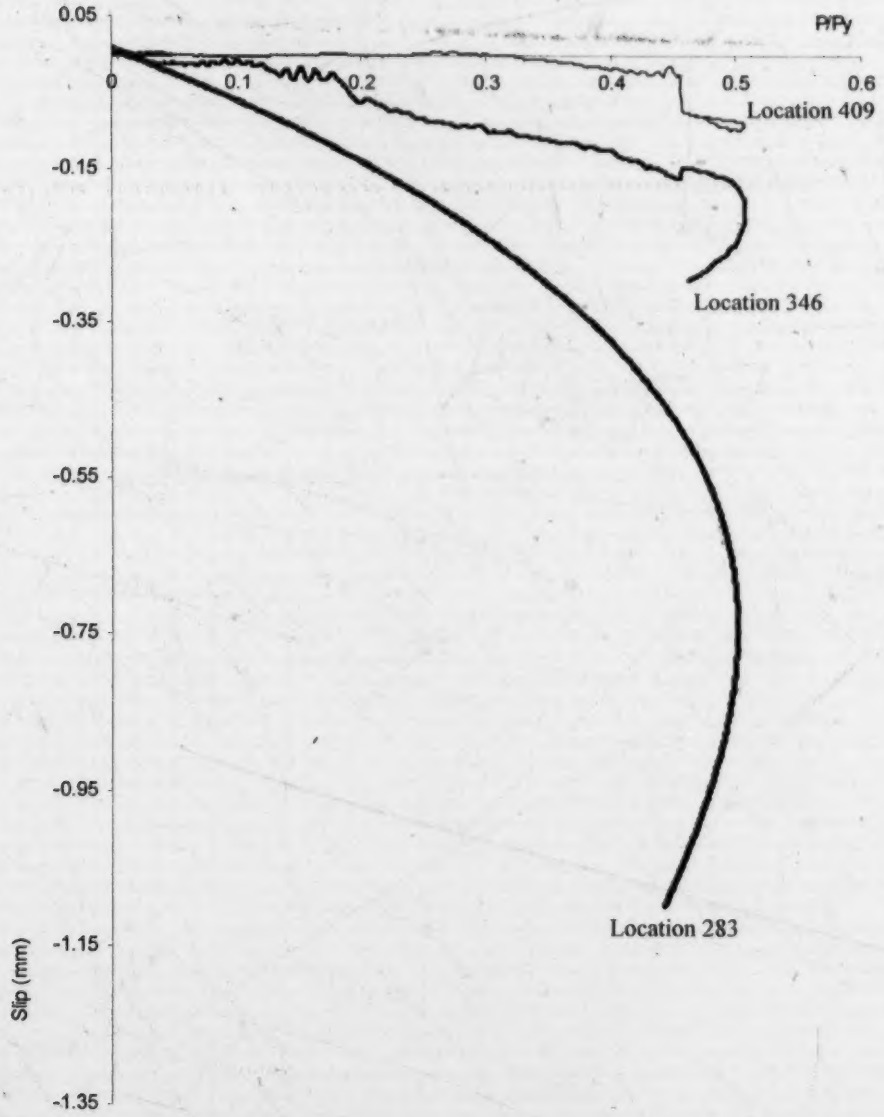

Figure (7.34) – Slip at Different Locations on the Bend for Case 1

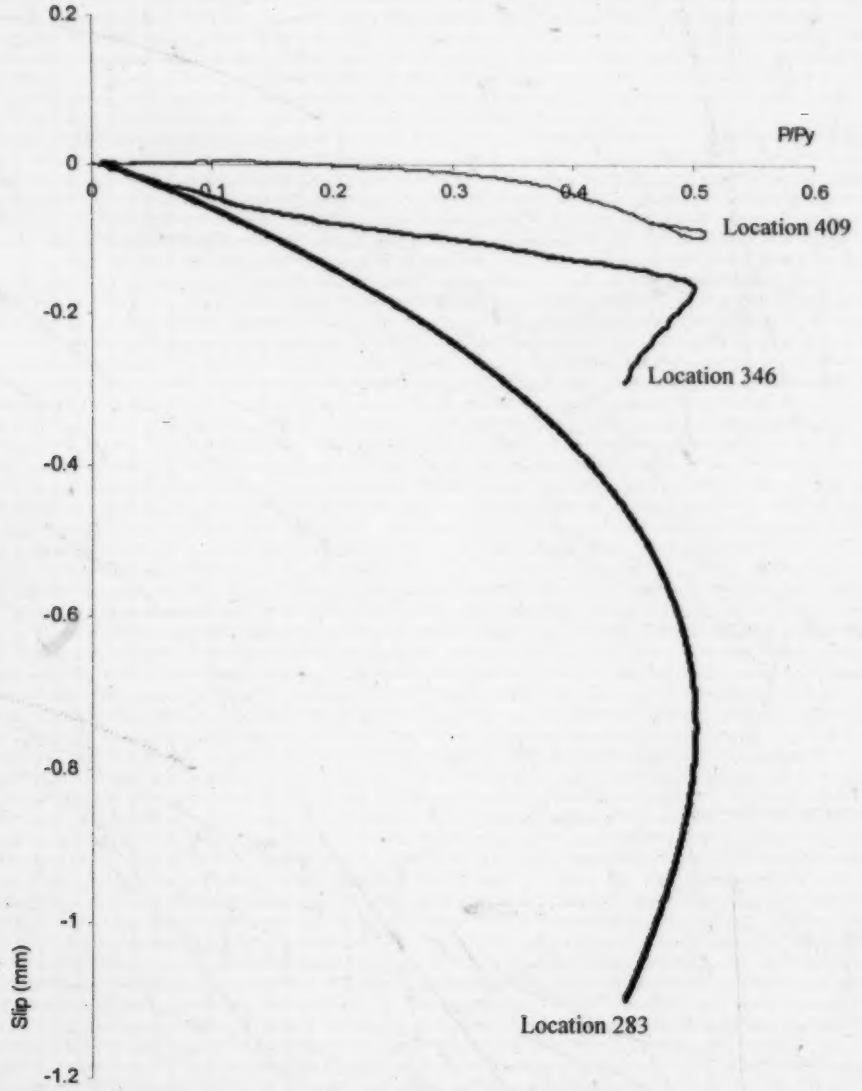

Figure (7.35) – Slip at Different Locations on the Bend for Case 2

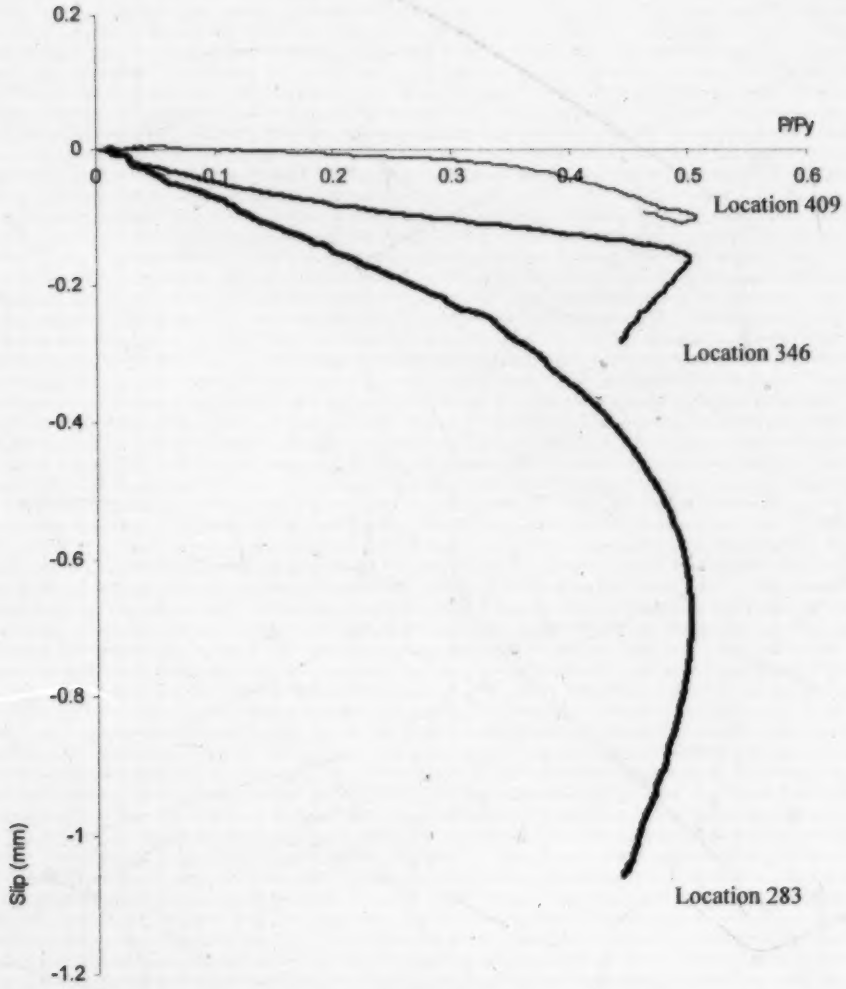

Figure (7.36) – Slip at Different Locations on the Bend for Case 3

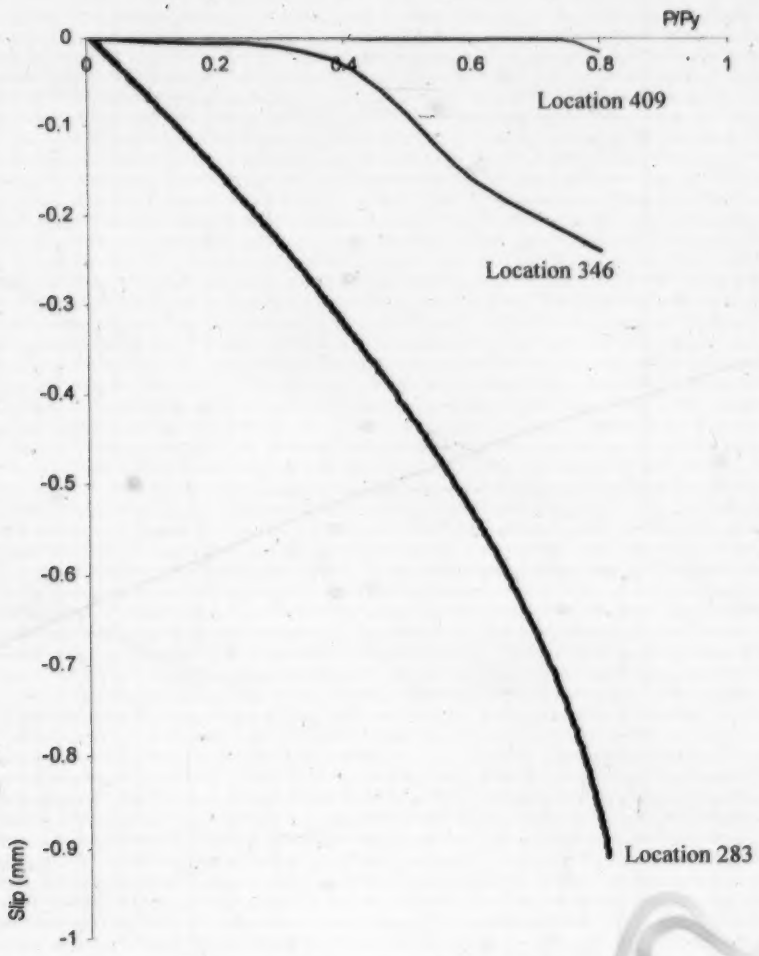

Figure (7.37) – Slip at Different Locations on the Bend for Case 4

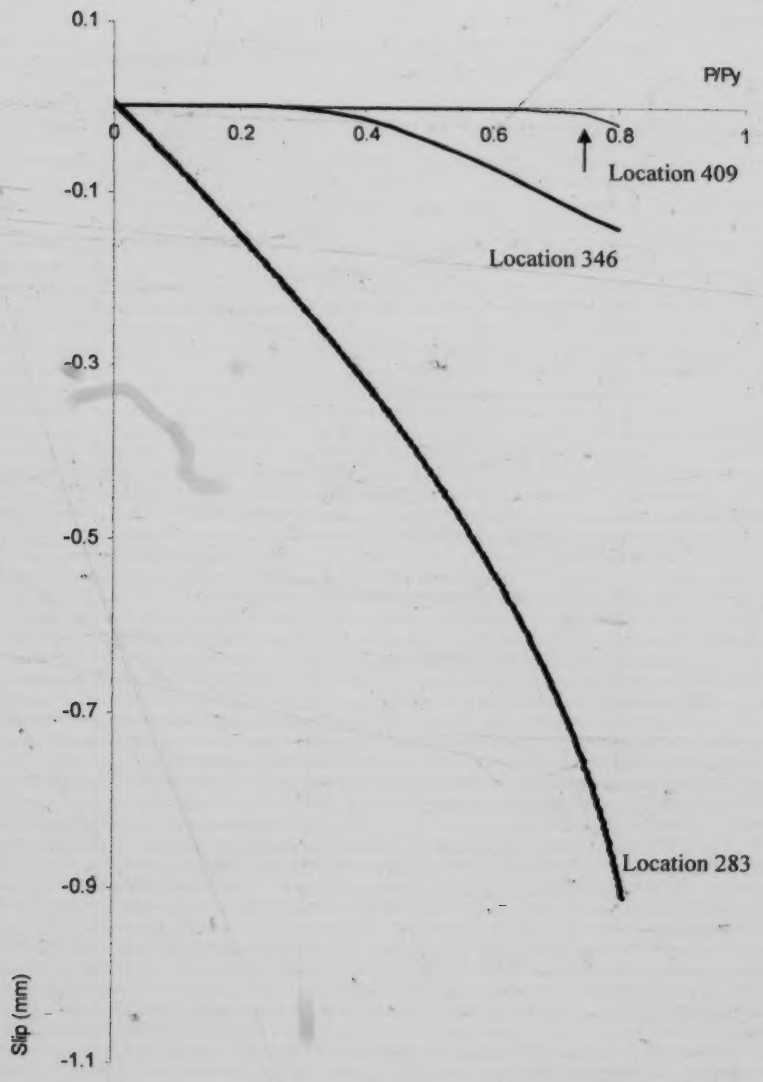

Figure (7.38) – Slip at Different Locations on the Bend for Case 5

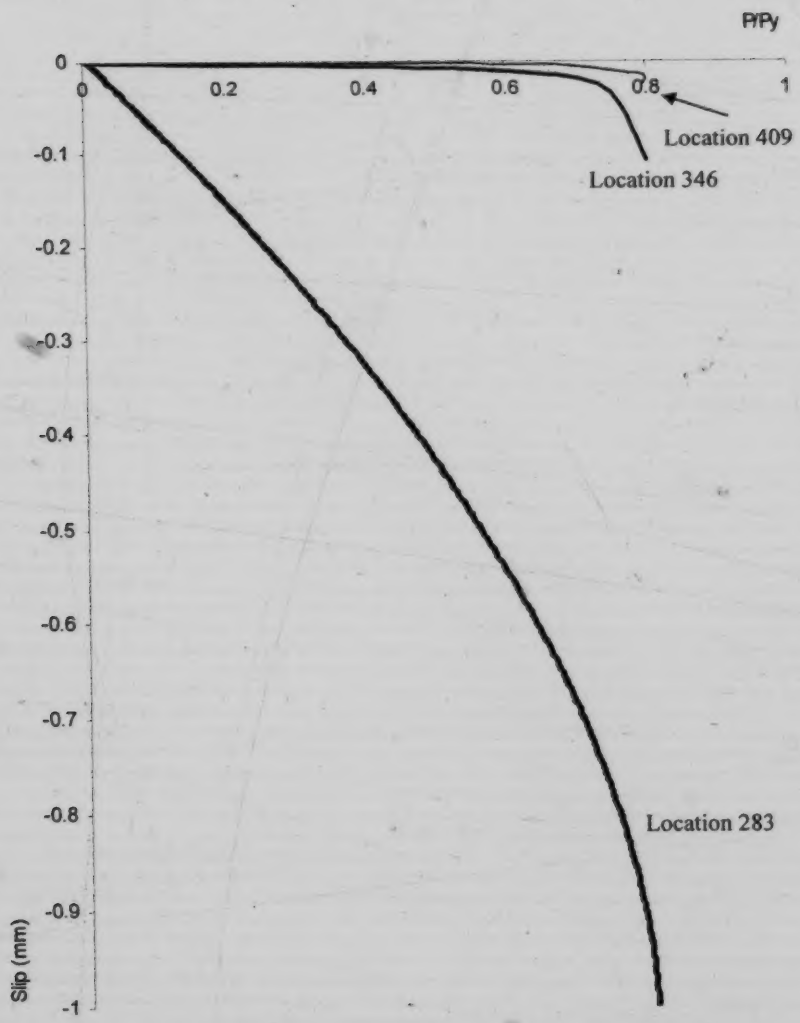

Figure (7.39) – Slip at Different Locations on the Bend for Case 6

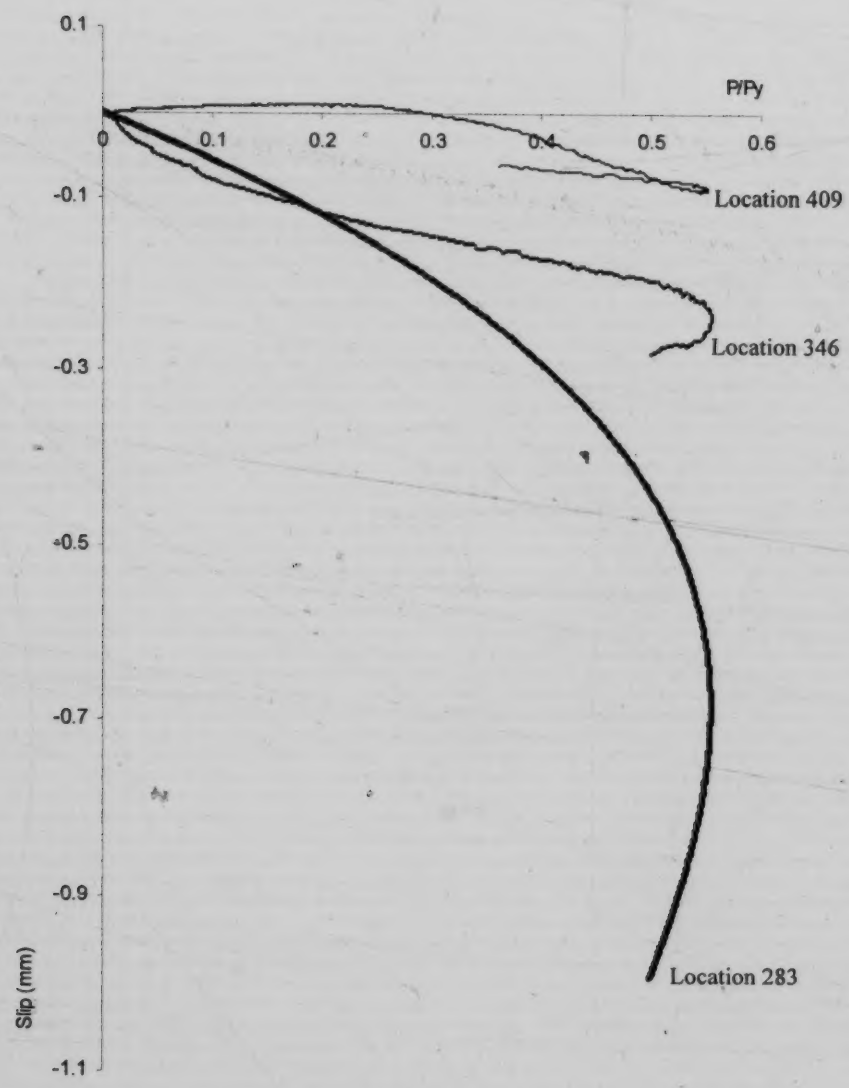

Figure (7.40) – Slip at Different Locations on the Bend for Case 7

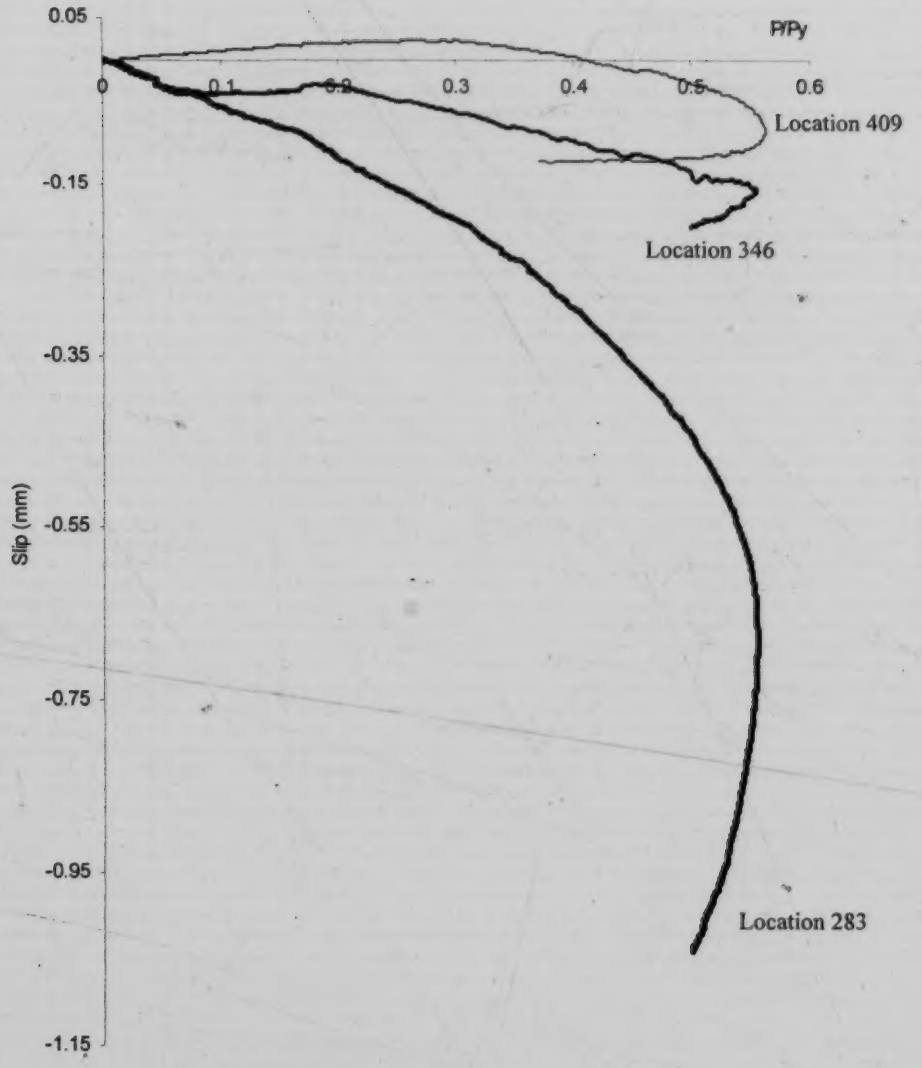

Figure (7.41) – Slip at Different Locations on the Bend for Case 8

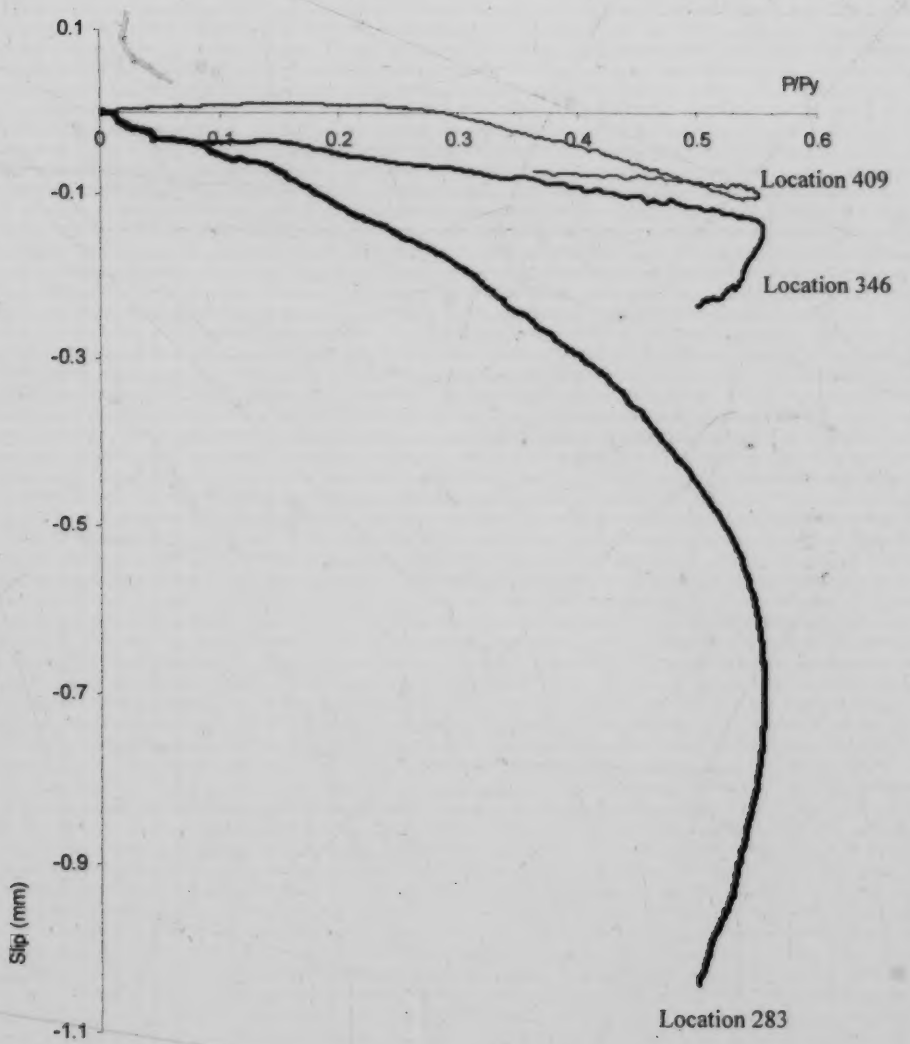

Figure (7.42) – Slip at Different Locations on the Bend for Case 9

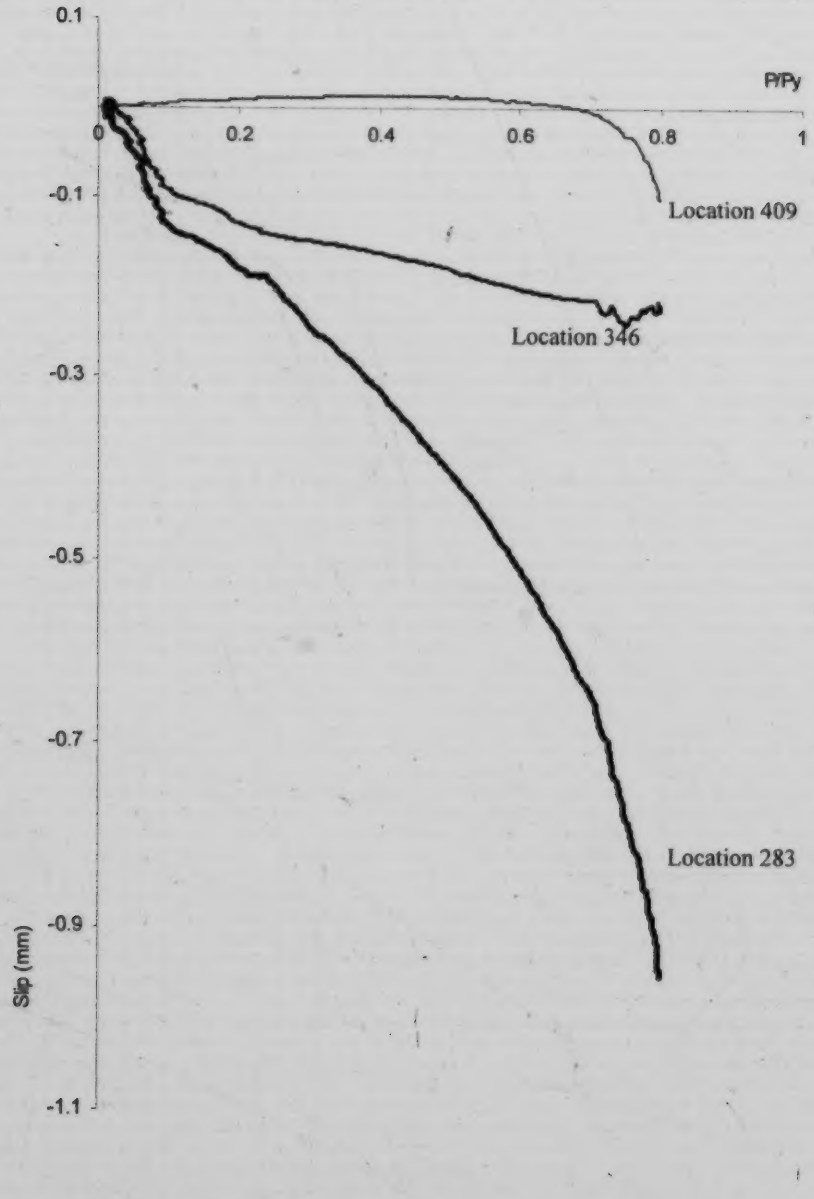

Figure (7.43) – Slip at Different Locations on the Bend for Case 10

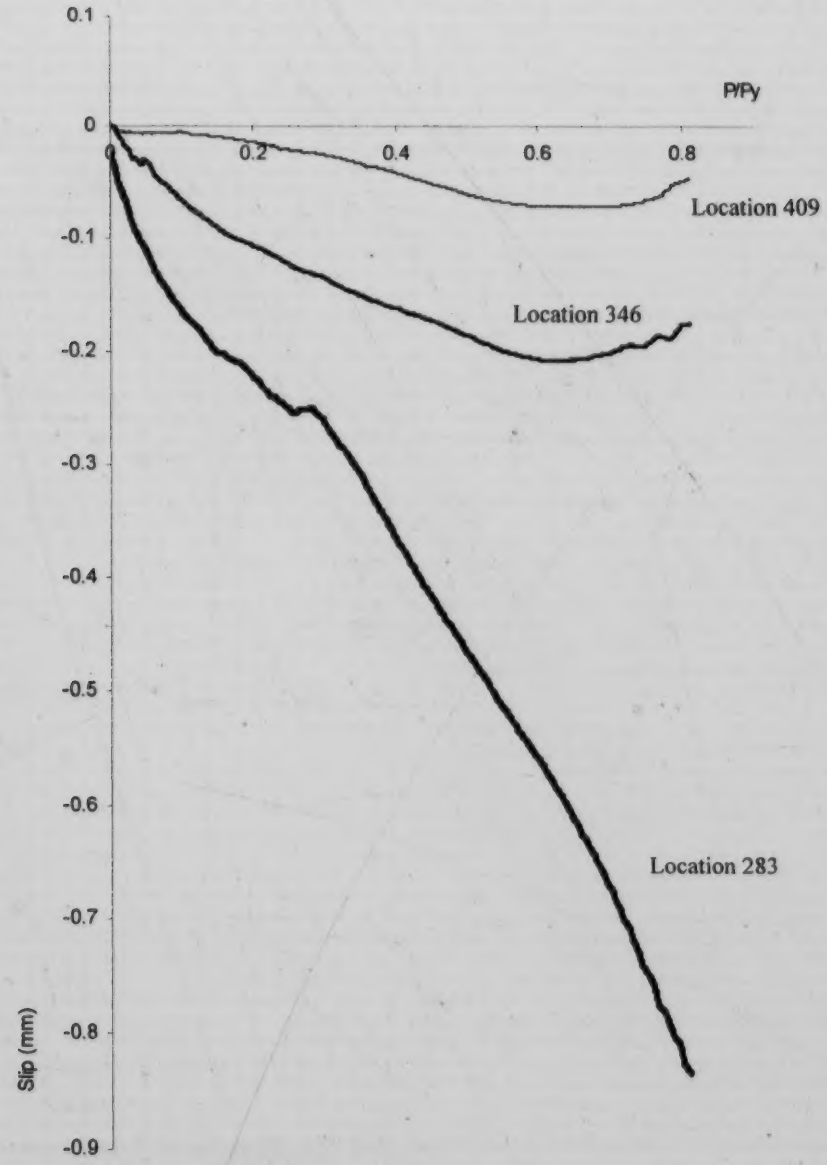

Figure (7.44) – Slip at Different Locations on the Bend for Case 11

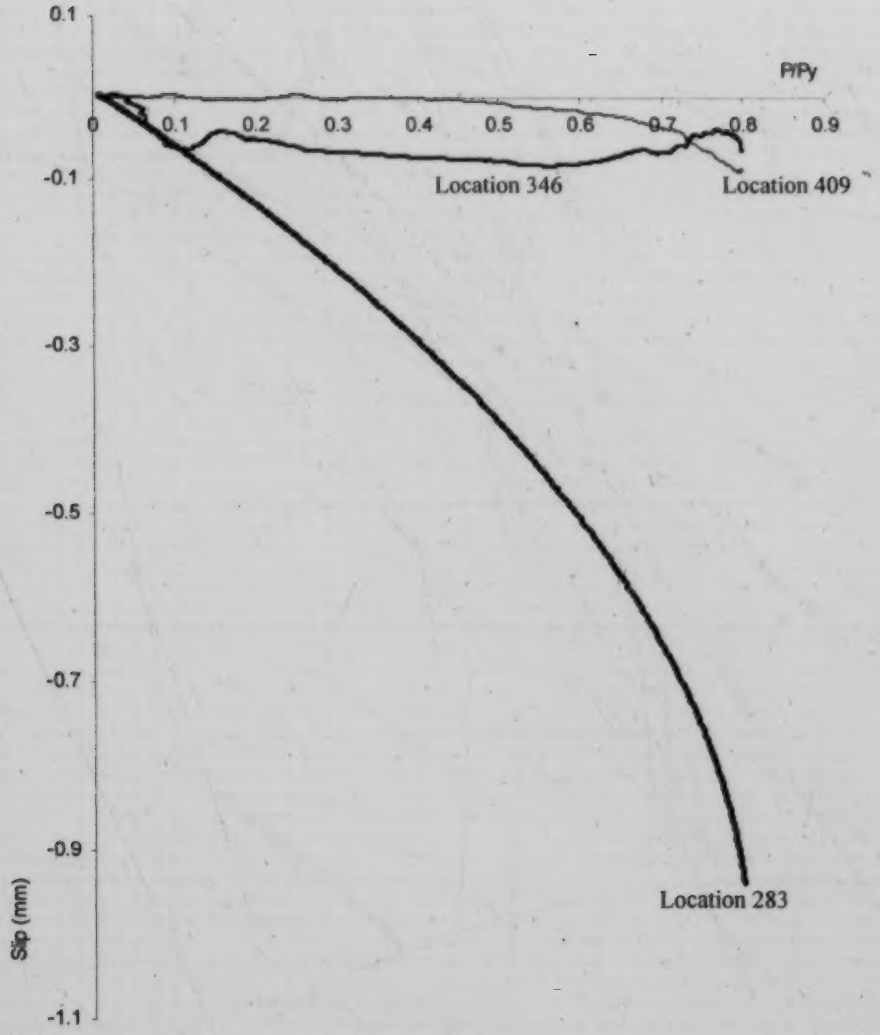

Figure (7.45) – Slip at Different Locations on the Bend for Case 12

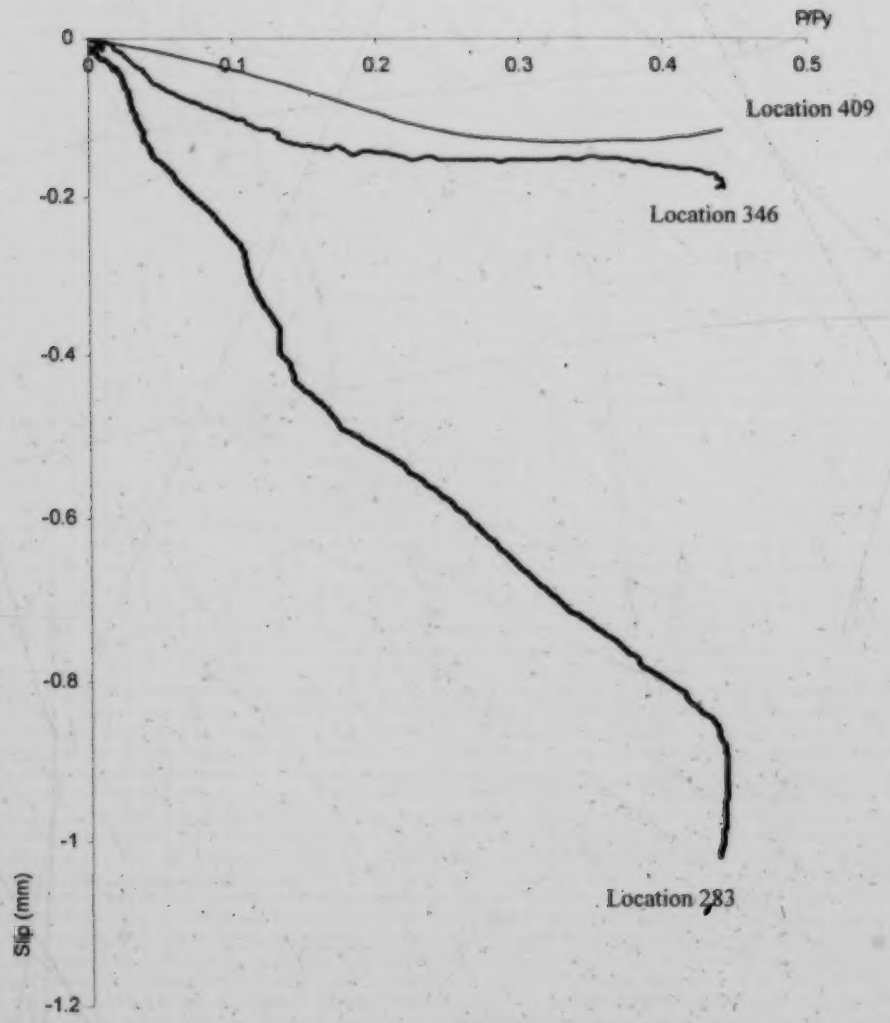

Figure (7.46) – Slip at Different Locations on the Bend for Case 13

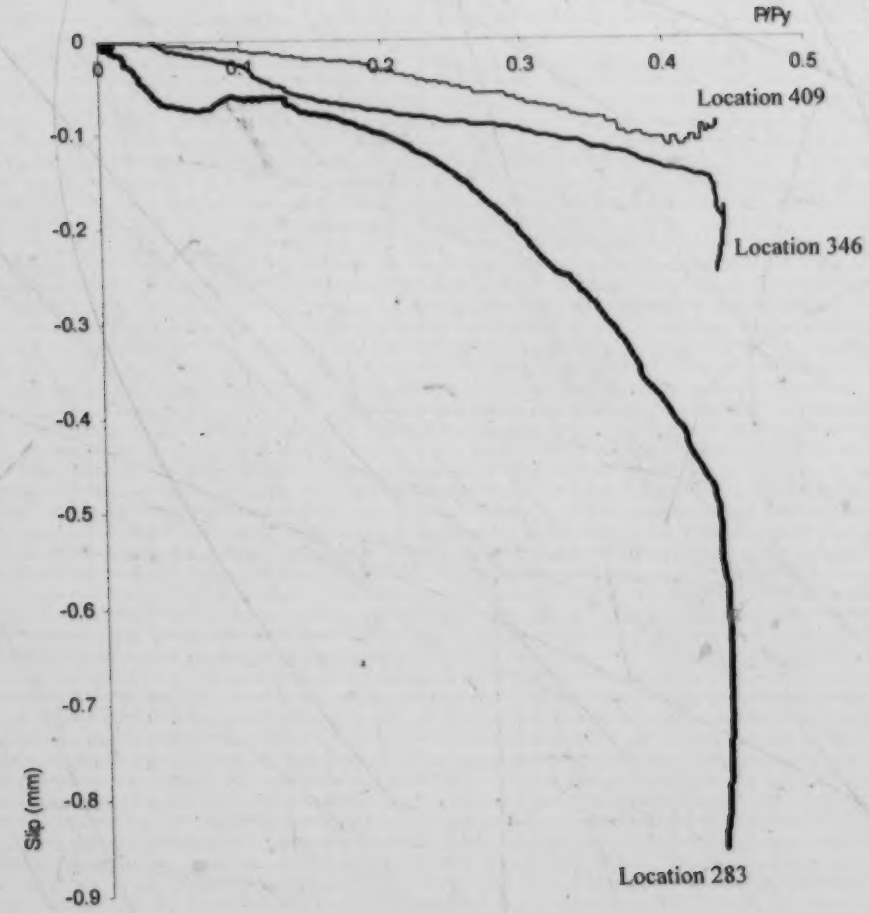

Figure (7.47) – Slip at Different Locations on the Bend for Case 14

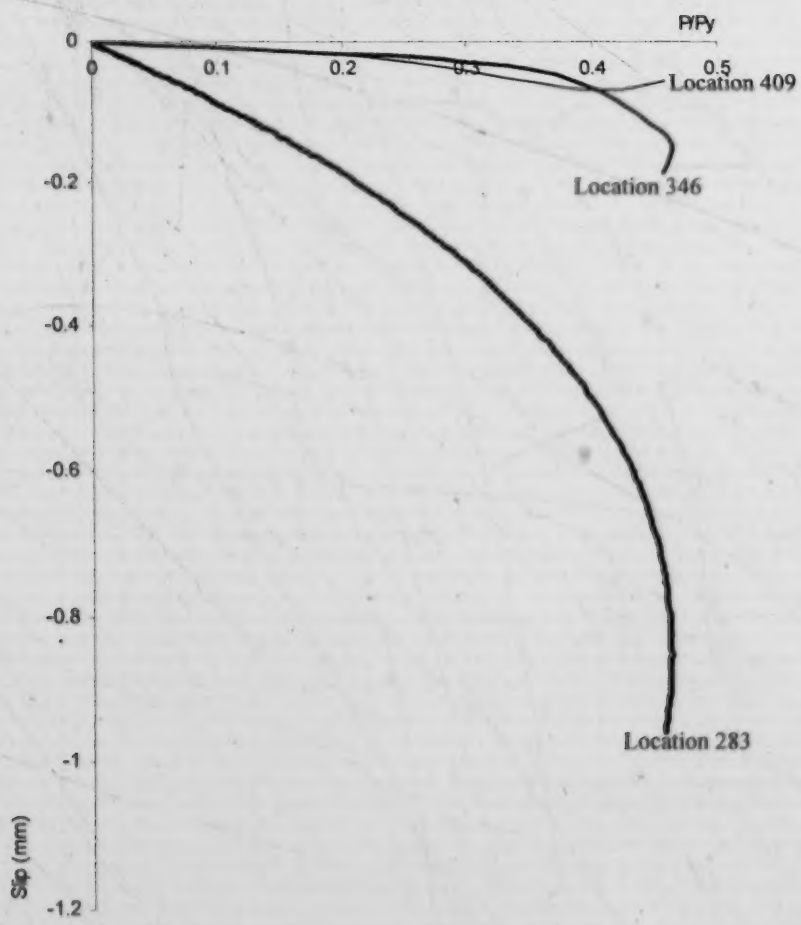

Figure (7.48) – Slip at Different Locations on the Bend for Case 15

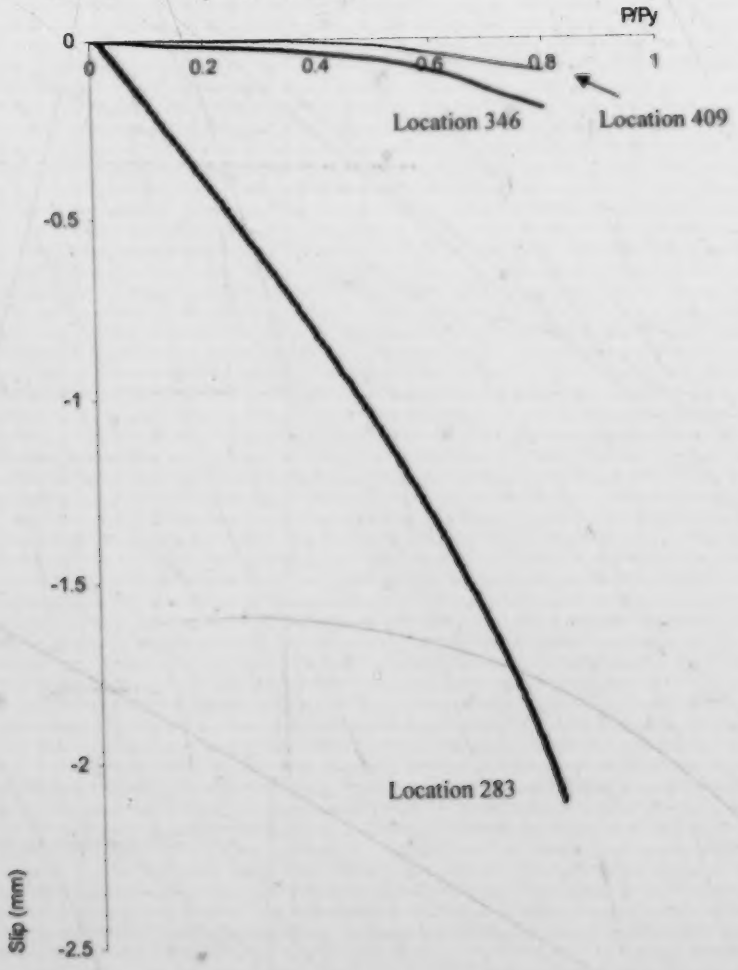

Figure (7.49) – Slip at Different Locations on the Bend for Case 16

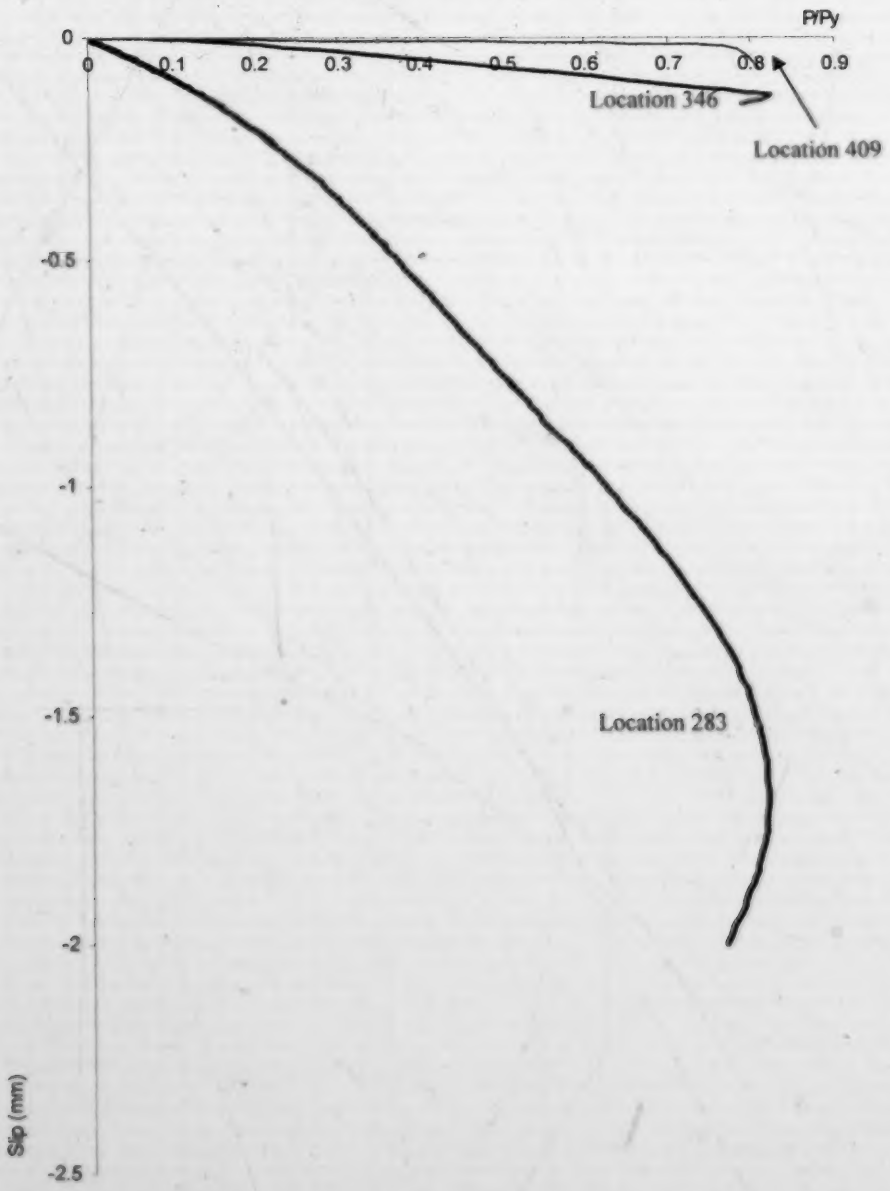

Figure (7.50) – Slip at Different Locations on the Bend for Case 17

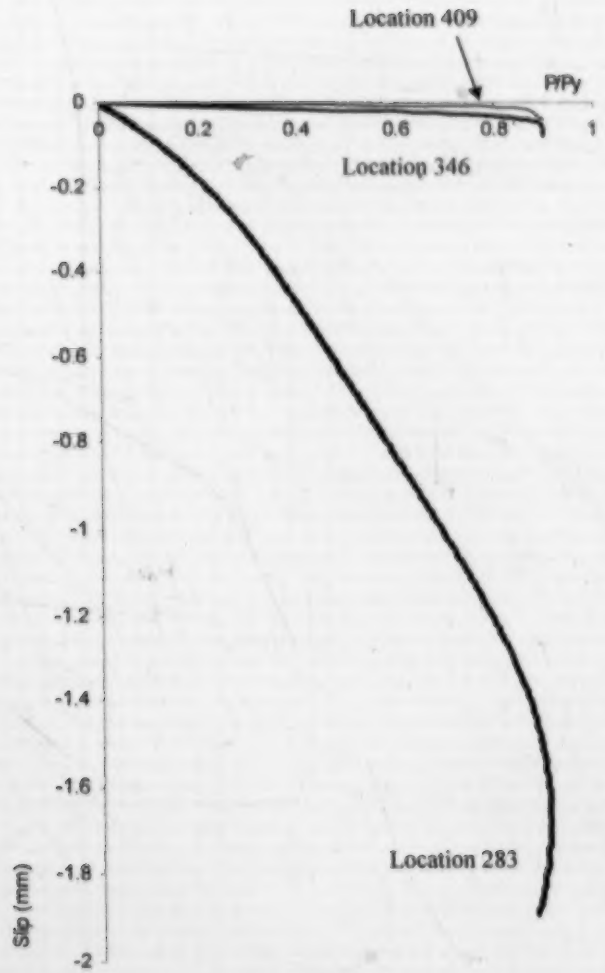

Figure (7.51) – Slip at Different Locations on the Bend for Case 18

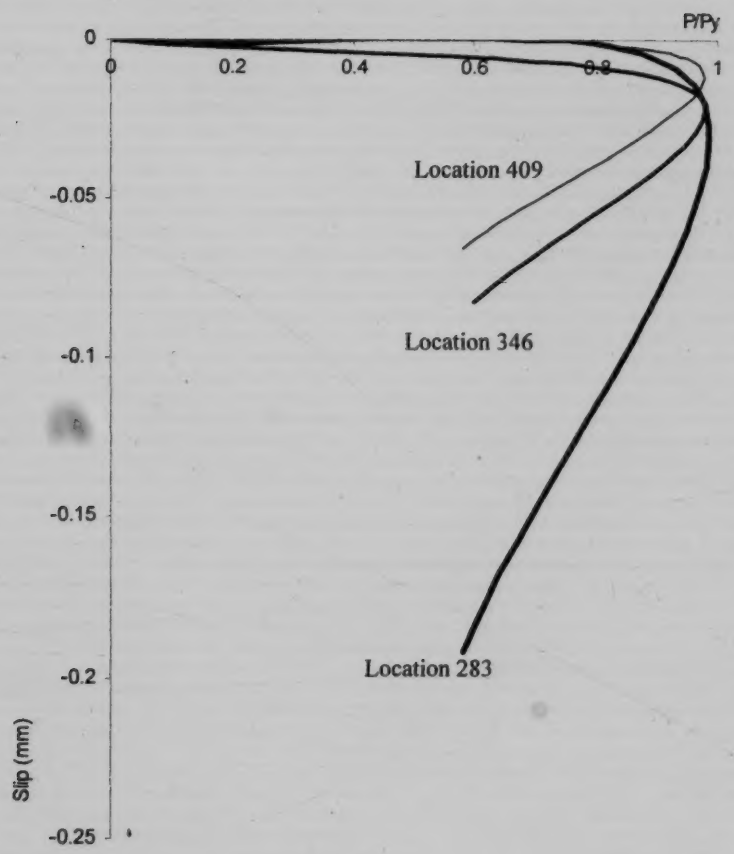

Figure (7.52) – Slip at Different Locations on the Bend for Case 19

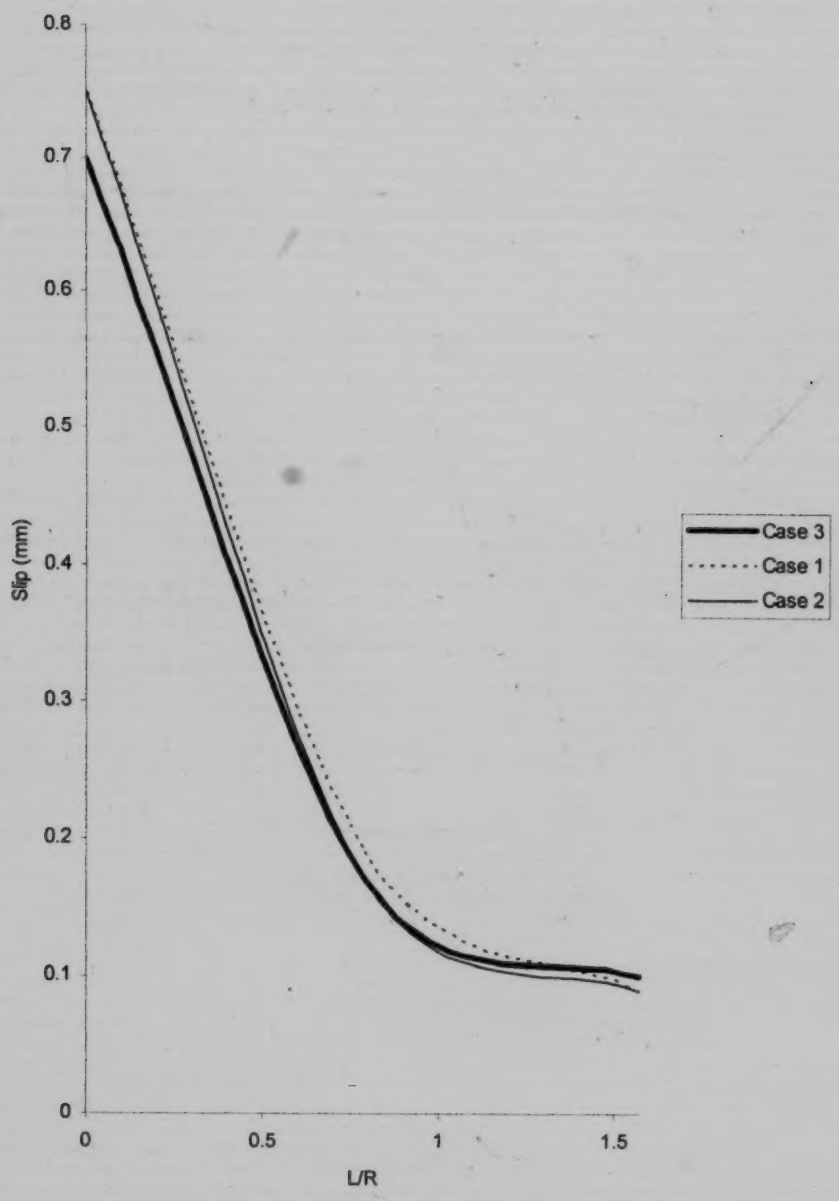

Figure (7.53) – Slip Trend on the Bend at Peak Load for Cases 1 to 3 with $4\,d_b$ to $12\,d_b$ of Tail Length Respectively

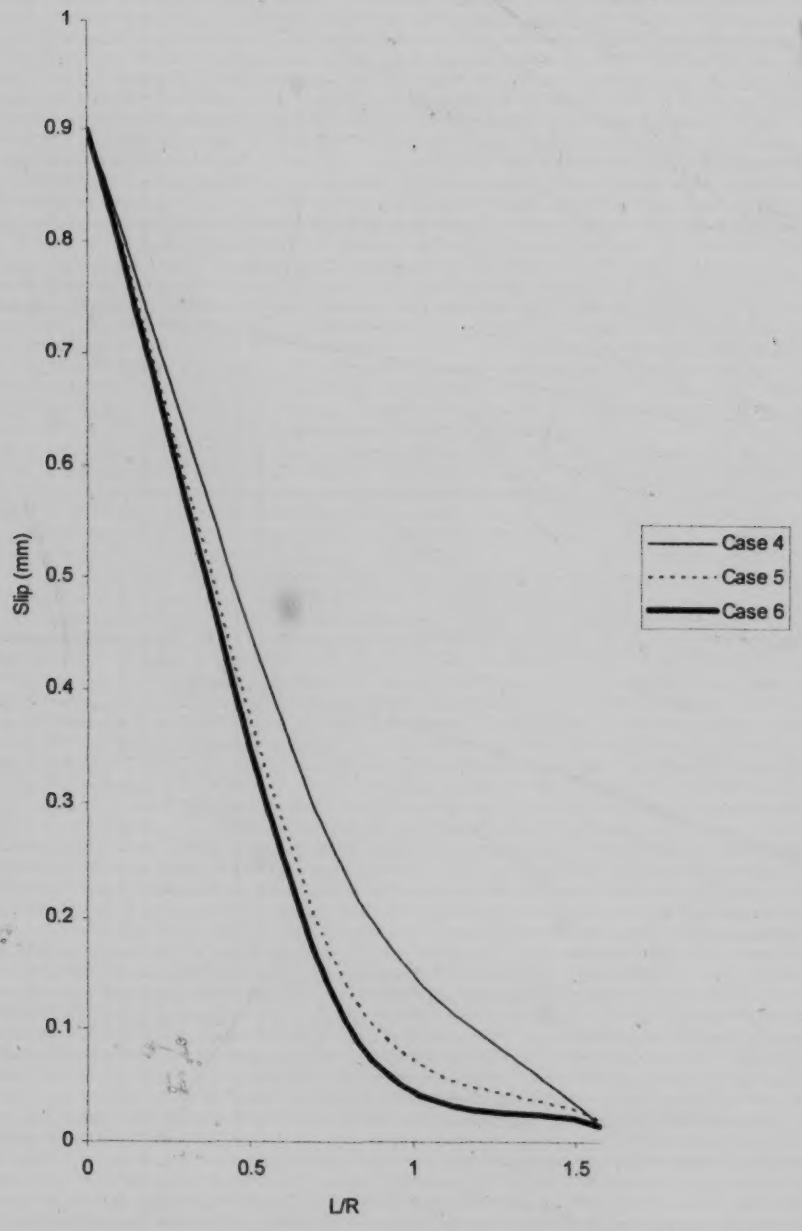

Figure (7.54) – Slip Trend on the Bend at Peak Load for Cases 4 to 6 with $4\,d_b$ to $12\,d_b$ of Tail Length Respectively

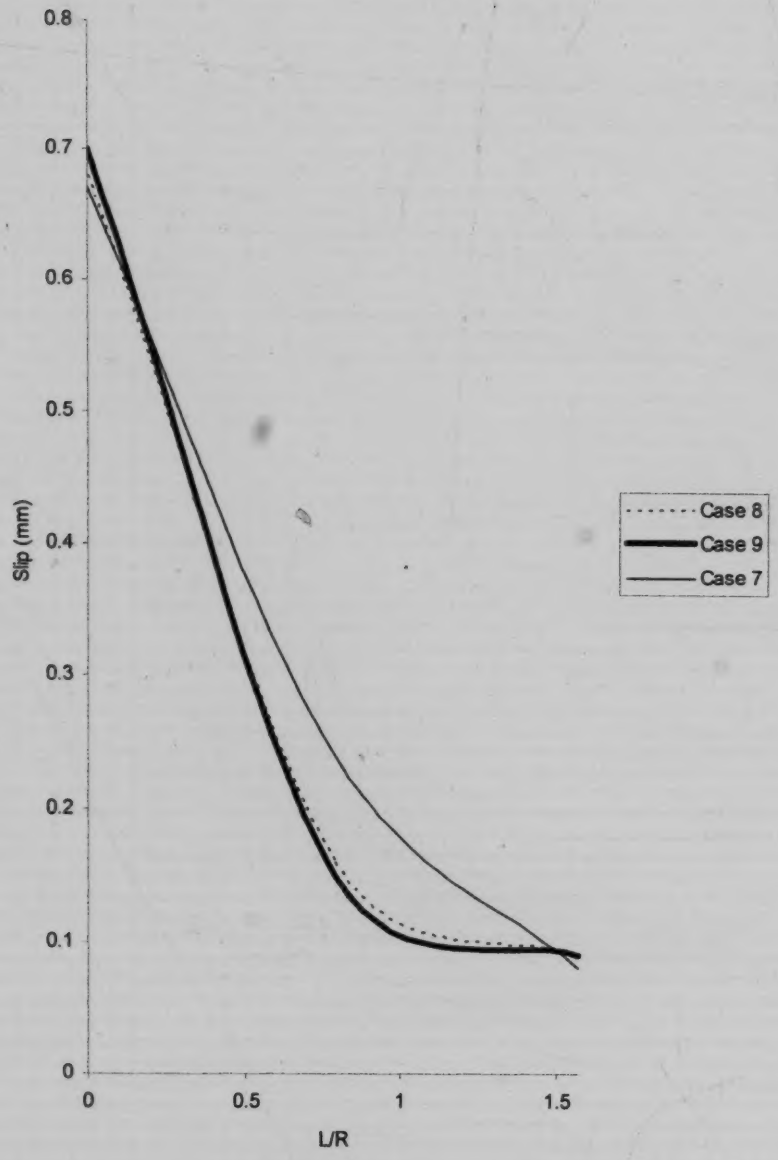

Figure (7.55) – Slip Trend on the Bend at Peak Load for Cases 7 to 9 with $4\,d_b$ to $12\,d_b$ of Tail Length Respectively

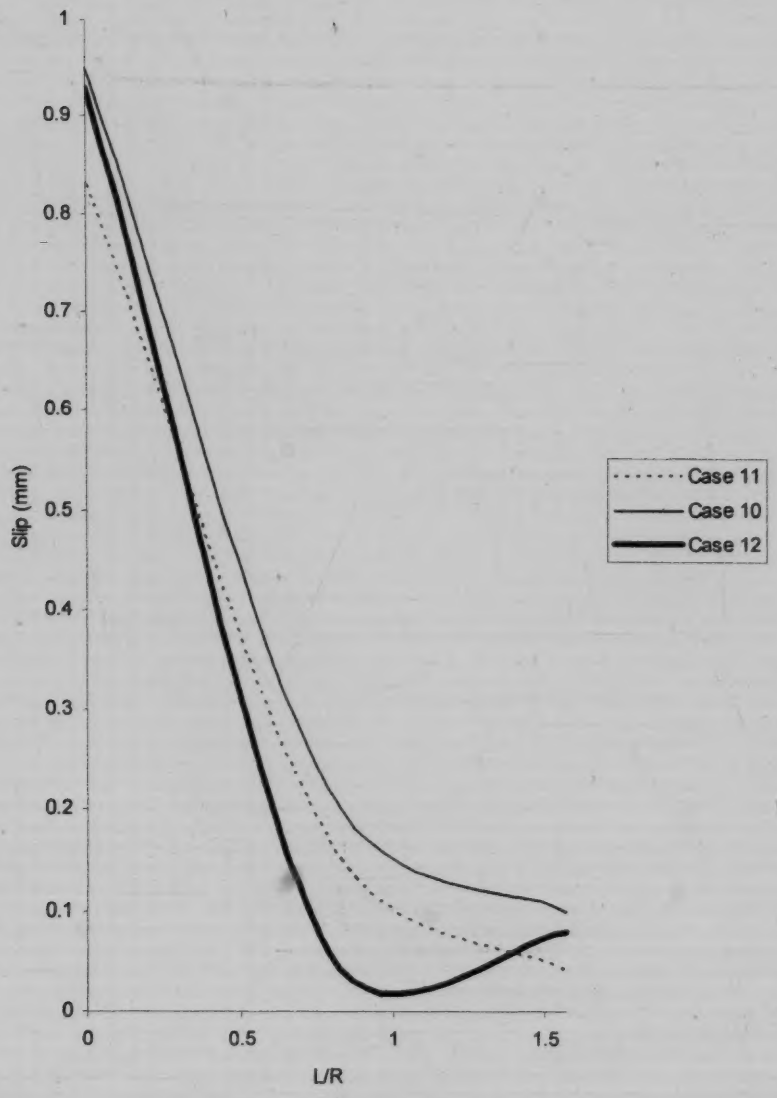

Figure (7.56) – Slip Trend on the Bend at Peak Load for Cases 10 to 12 with $4\,d_b$ to $12\,d_b$ of Tail Length Respectively

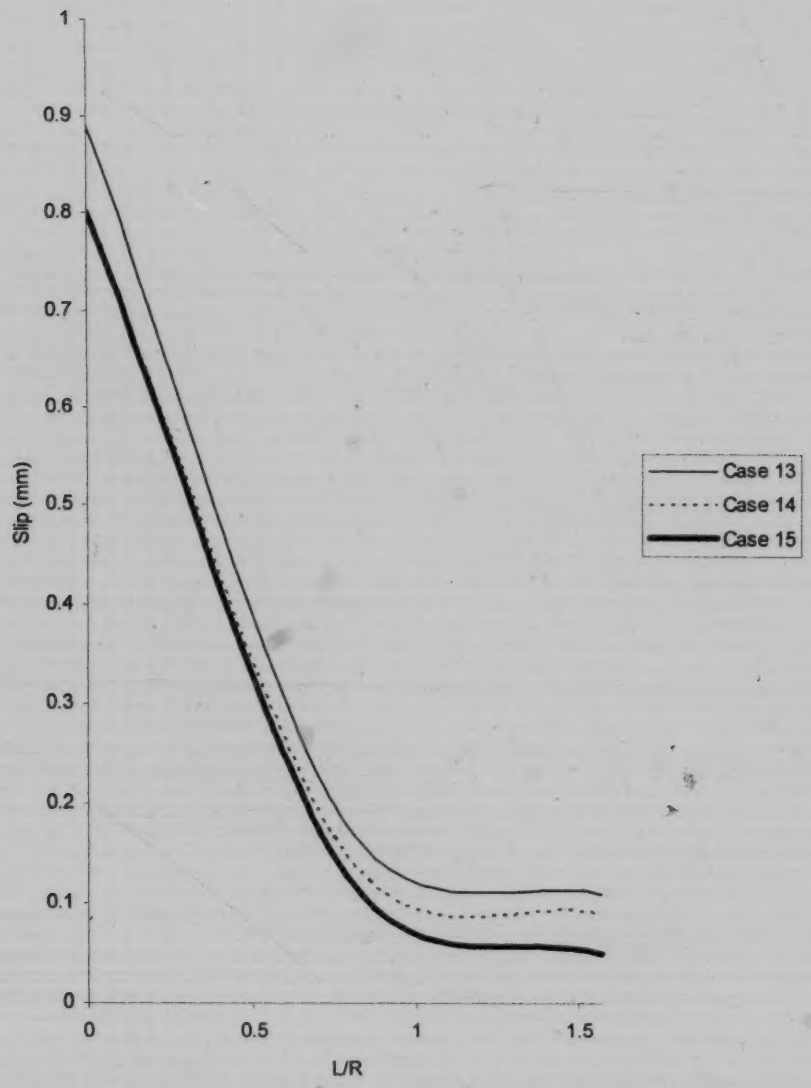

Figure (7.57) – Slip Trend on the Bend at Peak Load for Cases 13 to 15 with $4\,d_b$ to $12\,d_b$ of Tail Length Respectively

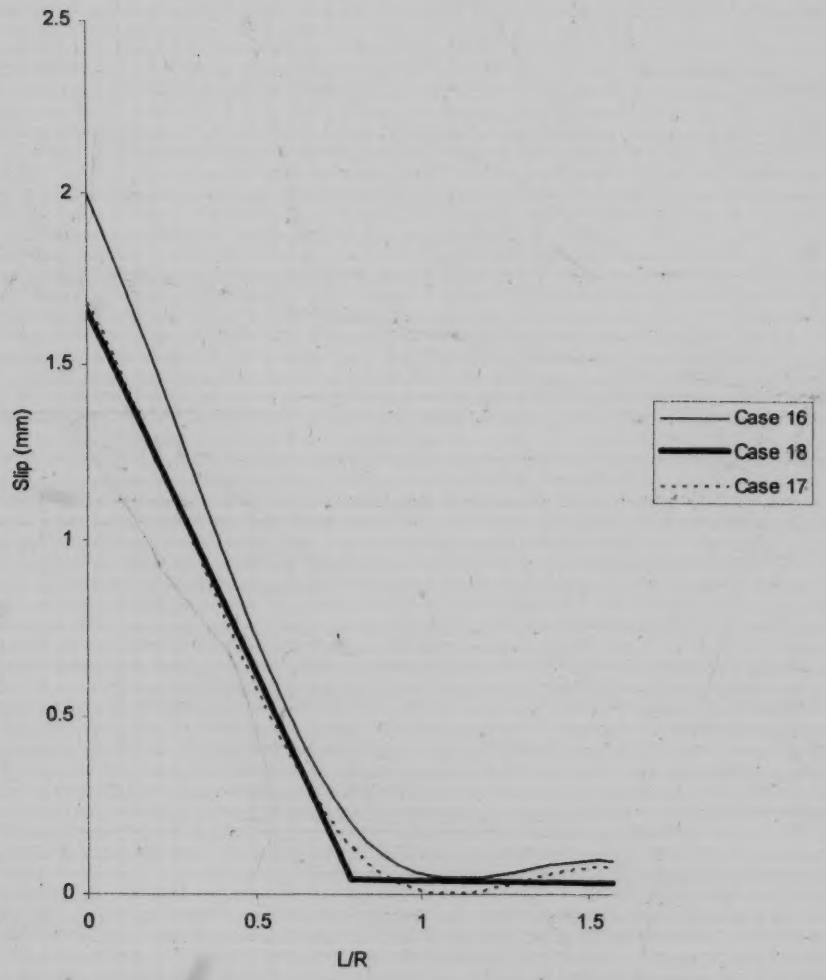

Figure (7.58) – Slip Trend on the Bend at Peak Load for Cases 16 to 18 with $4\,d_b$ to $12\,d_b$ of Tail Length Respectively

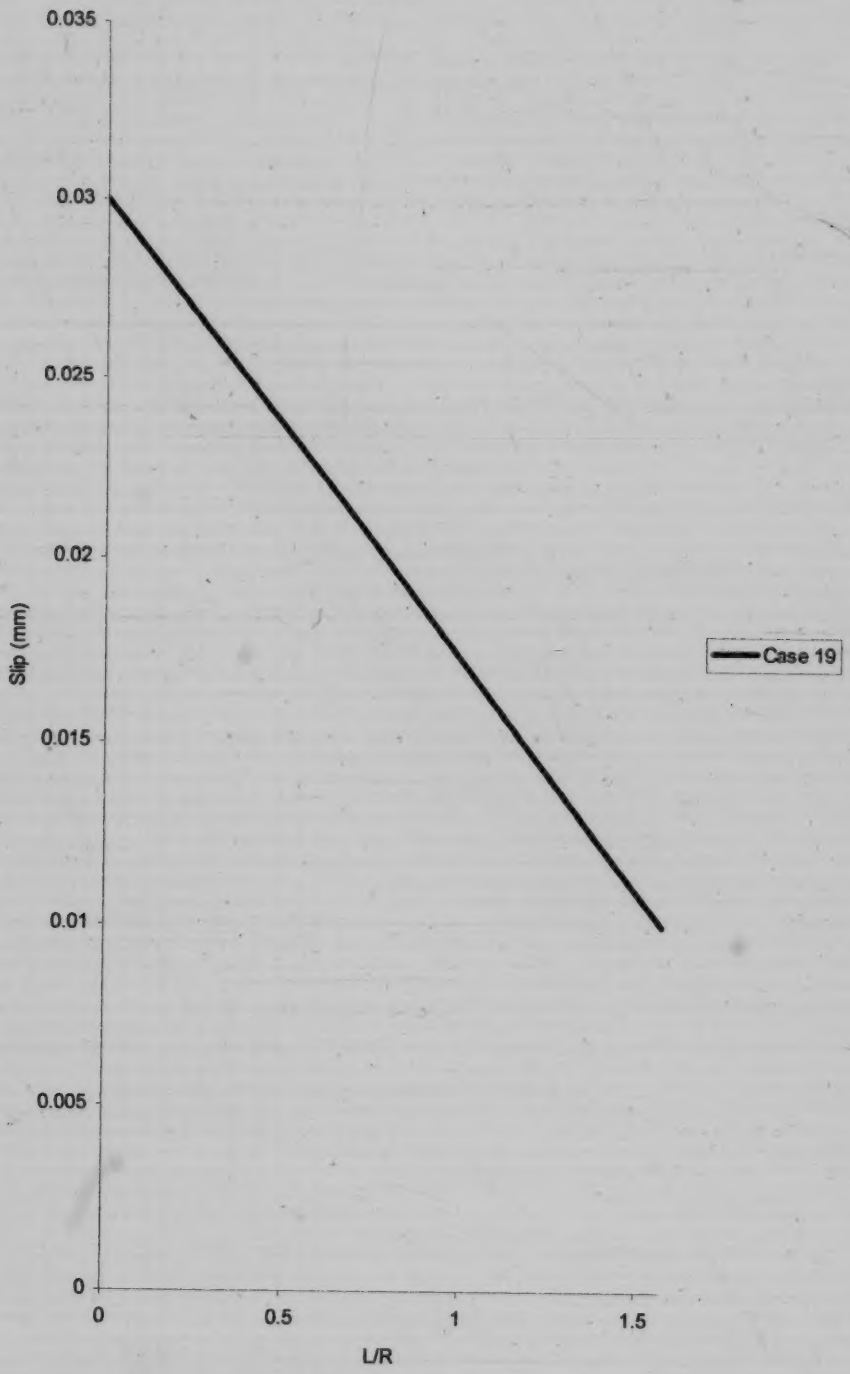

Figure (7.59) – Slip Trend on the Bend at Peak Load for Cases 19

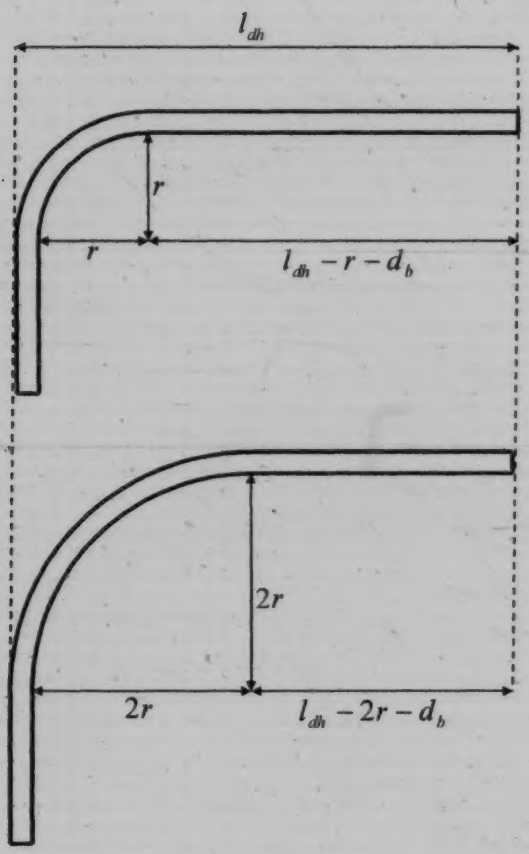

Figure (7.60) – Standard hook with minimum and twice radii of bend

8. Conclusion

8.1. Summary

A test specimen of a joint has been designed, fabricated, and tested under a negative moment produced from loading vertically with MTS-6000 machine. The specimen was designed with strut and tie model, which is an adequate tool to design disturbed regions such as beam-column joints. This specimen contained large diameter bent bars. Three layers of 35M bars were used as main tension steel. The main tension steel was bent at the corner with a radius of 5.0 inches and at the steel end with the same radius to make two 180 degree hooks near the end of specimen. Two layers of 20M bars were used as compression steel. Stirrups with 15 mm diameter were placed at 100 mm center to center. Two 19 mm thick steel plates were installed at the ends of specimen to distribute the compressive force of MTS-6000 on the two end cross-sections of specimen. This arrangement prevents crushing of concrete at the two ends of specimen. Material properties were 35 MPa concrete and 400 MPa steel.

For the purpose of instrumentation, LVDT's were installed from the top to ground and from the corner to ground to measure the vertical deflection. Strain gauges were placed on the 35M reinforcing bars from the beginning of the bend to the face of the joint.

In order to simulate the abovementioned specimen, a finite element analysis has been carried out using three dimensional brick and three dimensional wedge elements for concrete and steel. Stirrups and compression bars were modeled with three dimensional truss elements embedded into concrete elements. End steel plates were modeled with flat rigid elements. The method of damaged plasticity was used to model the concrete material properties. Damaged plasticity of the concrete includes compression and tension softening phenomena. The yield surface and plastic potential function used in damaged plasticity are Lubliner

(1989) and Drucker-Prager (1951). Saenz (Chen, 1982) and Li et al. (2002) curves have been used to model compression and tension behaviors of concrete respectively. Explicit bond modeling was necessary to accurately analyze the specimen.

Three dimensional Cartesian elements were used to model the steel-concrete bond interface. For simplification of mesh generation an equivalent rectangular cross-section was used for main tension bars. This equivalent cross-section has the same area and moment of inertia as the real circular cross-section but its perimeter is different. Therefore, the association of bond forces to the nodes of steel and concrete elements on the interface should be done according to the real perimeter. This method ensures the same stresses will be produced in the equivalent cross-section as the real bar cross-section with the same amount of bond stress applied on them.

According to literature bond is composed of three components: chemical adhesion between concrete and steel surfaces, friction between steel and concrete surfaces and keying of concrete deformations against steel ribs. Failure mechanism of bond is by shearing off the concrete keys against steel surface or by splitting which is a much more abrupt phenomenon. The proposed bond-slip model for un-tied and perfectly tied concrete assumes tri-linear and bilinear forms respectively. This model evaluates the bond stress in terms of slip and the maximum bond capacity which can be confined or unconfined. The unconfined bond capacity can be obtained from equations in the literature. The confined bond capacity can be obtained from an expression proposed in chapter 4, which is a function of the unconfined bond capacity and the ratio of the normal pressure over compressive strength of concrete. This expresion has been obtained by a large number of trial analyses of the specimen described in chapter 3. A comparison of this expression with the past researchers test results show that it is close to test results from Malvar (1992) and Untrauer (1968).

This model accounts for strength of concrete, cover, bar size, level of confinement, stirrups and splitting of concrete. In this model bond is a function of slip and the level of confinement. With increasing level of confinement the bond capacity increases. For unconfined concrete the mode of failure is splitting which can be simulated by the proposed bond model. The splitting of concrete is modeled through a descending branch in the bond-slip relationship. The ultimate slip beyond which the bond value is zero increases with increased confining pressure and the descending branches of bond-slip diagrams at high confining pressures tend to become parallel. For fully confined concrete, splitting does not happen and thus a flat branch is considered after the ascending branch.

The analysis procedure was ABAQUS explicit analysis in quasi static form. This type of analysis uses a large number of time steps and is a fast method since it does not solve a simultaneous system of equations. This type of analysis is the most appropriate for reinforced concrete because of the inherent discontinuous nature of reinforced concrete structures. Compared to other methods of analysis such as Newton-Raphson explicit dynamic analysis is more efficient in terms of convergence. To further accelerate the procedure method of variable mass scaling was used.

This bond model was automated to provide a surface constitutive model that does not need an iterative procedure. The concept of non-perfect lateral reinforcement has been considered using an analogy to seismic design. For this purpose, a reinforcement ratio is adopted as a means to measure whether or not the reinforcement is perfect. This ratio is a function of the volumetric ratio of lateral reinforcement to the concrete core confined by it and the yielding strength of steel and the compressive strength of concrete. If this ratio is equal or larger than 1.0, perfect lateral confinement is deemed. If this ratio is zero no confinement is provided, and for the values of the lateral reinforcement ratio between zero and 1.0 a non-perfect condition is assumed. The descending branch of the bond-slip model is dependent on the lateral reinforcement ratio and for perfect confinement

is flat whereas for no confinement it is a steep descending branch. However, for non-perfect confinement the descending branch is between the two extremes.

For the purpose of verification of the proposed bond-slip model fourteen different cases were studied out of which thirteen models were simulations of test specimens in the literature. Based on the results of simulations the proposed bond model is in good agreement with previous researchers' test results and it also renders results which are close to the test results explained in chapter 3. A comparison of the proposed finite element approach with Lowes et al. (2004) finite element model shows that the present bond-slip model is able to model the unconfined condition although Lowes et al. model was not capable of doing so. In addition, the present approach was proven to be able to efficiently simulate confined concrete conditions. The proposed model can predict the shear failure of concrete since this failure is a material type of failure and when the shear stresses at the interface reach the critical values shearing starts to happen in concrete elements.

For the purpose of parametric study 90 degree hooks with large bar diameters were studied. These bar sizes are the most critical in development since they have large cross-sections which demand more bond forces accumulated to yield the bar cross-section. The parameters of interest were bend radius and tail length. These parameters were studied to find out their effect on the bend region capacity. There are recommendations in the code commentary which specify minimum bend radii for different bar sizes. These recommendation are based on practical considerations since it is not possible to bend a bar with a radius smaller than minimum in the workshop. However, these values are not the best concerning the bend region capacity and it is possible to bend a bar with a radius larger than minimum.

High strength concrete and large covers were avoided to target those situations where there is no obvious mistake in design according to code but undesirable

failure happens. A total of nineteen different joint like pullout models were studied. The reason a joint configuration was chosen was to avoid impractical configurations in terms of extremely large concrete covers and to make the model as close to reality as it can be without making it too complex. The dimensions of the models are chosen in way that there is no need to use stirrups in the joint region. Stirrups are avoided because they increase the hook capacity and make it difficult to draw a conclusion about which configuration is originally un-conservative. The straight development lengths in these models were zero except one case where full hook development length was considered. The reason the straight part was un-bonded was to prevent interference of straight length bond effect on capacity of the bend region. In other words, pure bend region capacities were to be studied. The proposed automatic bond-slip model was used to carryout the analysis. According to analysis results with increased bend radius there is increased capacity in the bend region and the tail length is not very influential regarding capacity. In addition, for 45M bars it was found that application of minimum bend radius is not conservative and it is recommended to use a radius twice minimum in hooks with this bar size. However, it is not recommended to use a short tail length since in some occasions in practice there may not be sufficient amount of cover on extension to prevent the tail from popping out.

8.2. Conclusions

The steel-concrete interface follows a specific bond behavior. The bond capacity changes from location to location along a bent bar because of the different corresponding confinement levels. For curved bars the inside face of steel is confined while the outside face exhibits unconfined behavior. When there is no confining reinforcement, the mode of failure is splitting. Conversely when there is perfect confinement the mode of failure is shearing of concrete. For non-perfect confinement the mode of failure is a combination of the above modes which have been modeled in this research. Although some past finite element approaches were able to model confined concrete conditions but they were not able to effectively simulate the bond-slip behavior in the un-tied concrete. In addition,

past finite element models did not consider the non-perfect confinement concept. These deficiencies are not observed in the proposed model. The capacity of hooks increases if the radius of bend is increased. This increase is 2.35 to 3.18 times larger than what the code implies. The Canadian code provisions for hook development length are adequate for most cases except for 45M bars for which a bend radius twice the minimum radius is proposed to give a conservative hook.

8.3. Suggestions for Future Researchers

Since the code does not differentiate between 90 and 180 degree hooks it is suggested that the same type of parametric study be done for 180 degree hooks. In addition, a parametric study can be done on the performance of nonstandard hooks with 45 and 135 degree of bend angle. Investigating the effect of stirrups and the level of improvement due to different levels of reinforcement using the present bond model is another suggestion.

References

ACI Manual of Concrete Practice, Part 3, 2005.

Bathe, K.J, Finite Element Procedures, Prentice Hall, Englewood Cliffs, NJ, 1996.

Belytschko, T., Ong, J. S. J., Liu, W. K., Kennedy, J. M., "Hourglass Control in Linear and Nonlinear Problems", Computer Methods in Applied Mechanics and Engineering, 43, (1984), 251-276.

Benson, D. J, "Computational Methods in Lagrangian and Eulerian Hydrocodes", Computer Methods in Applied Mechanics and Engineering, Vol.99, PP.235-394, North Holland, 1992.

Brant, J. L., Houde, J., Gerstle, K. H., "Direct Measurement of Slip Between Steel and Concrete", ACI Structural Journal, November-December 1986.

Chen, W. F, Plasticity in Reinforced Concrete, McGraw-Hill, New York, 1982.

Drucker, D.C., "A More Fundamental Approach to Plastic Stress-Strain Relations, Proceedings of first U.S. National Congress on Applied Mechanics, Chicago, 1951, PP. 4817-491.

Eligehausen, R., Popov, E. P, and Bertero, V. V, Local Bond Stress-Slip Relationships of Deformed Bars Under Generalized Excitations, Report No. UCB/EERC-83/23, Earthquake Engineering Research Center, University of California, Berkeley, 1983.

Feldman, L. R., Bartlett, M., "Bond Strength Variability in Pullout Specimens with Plain Reinforcement", ACI Structural Journal, November-December 2005.

Gambarova, P. G, Rosati, G. P,"Bond and Splitting in Bar Pull-Out: Behavioral Laws and Concrete Cover Role", Magazine of Concrete Research, Vol. 49, No.179, PP. 99-110, June 1997.

Gambarova, P. G, Rosati, G. P. and Schumm, C. E, "Bond and Splitting: A Vexing Question", ACI Special Journal, SP 180-2, PP. 23-43, 1998.

Hibbit, Karlsson & Surensen, Inc., (HKS), ABAQUS/Explicit User's Manual, Version 6.3, Hibbit, Karlsson & Surensen Inc., Pawtucket, Rhode Island, 2005

Hillerborg, A., M. Modeer, and P. E. Petersson, "Analysis of Crack Formation and Crack Growth in Concrete by Means of Fracture Mechanics and Finite Elements,"Cement and Concrete Research, vol. 6, pp. 773–782, 1976.

Hofstetter, G., Mang, H. A, Computational Mechanics of Reinforced Concrete Structures, Vieweg & Sohn Verlagsgesellschaft mbH, Braunschweig/Wiesbaden, 1995.

Keüser, M., Mehlhorn, G., "Finite Element Models for Bond Problems", Journal of Structural Engineering, 113, 1987, 2160-2173.

Lee, J., and G. L. Fenves, "Plastic-Damage Model for Cyclic Loading of ConcreteStructures,"Journal of Engineering Mechanics, vol. 124, no. 8, pp. 892–900, 1998.

Li, Q, Duan, Y and Wang, G, "Behaviour of Large Concrete Specimens in Uniaxial Tension", Magazine of Concrete Research, 54 (5), PP. 385-391, 2002.

Link, R. A., Elwi, A. E., Scanlon, A., "Biaxial Tension Stiffening Due to Generally Oriented Reinforcing Layers", Journal of Engineering Mechanics, Vol. 115, No. 8, August 1989.

Lormanometee, S., Bond Strength of Deformed Reinforcing Bar Under Lateral Pressure, University of Texas at Austin, January 1974.

Lowes, L. N, Moehle, J. P. and Govindjee, S, "Concrete-Steel Bond Model for Use in Finite Element Modeling of Reinforced Concrete Structures" ACI Structural Journal, Vol. 101, No.4, PP. 501-511, July-August 2004.

Lubliner, J., J. Oliver, S. Oller, and E. Oñate, "A Plastic-Damage Model for Concrete," International Journal of Solids and Structures, vol. 25, pp. 299–329, 1989.

Malvar, L. J,"Bond of Reinforcement Under Controlled Confinement", ACI Materials Journal, November-December 1992.

Marques, J. L. G., Jirsa, J., O.,"A study of Hooked Bar Anchorages in Beam-Column Joints", ACI Structural Journal, May 1975.

Mehlohrn, G., "Some developments for finite element Analysis of Reinforced Concrete Structures", Proceedings of the Second International Conference on Computer Aided Analysis and Design of Concrete Structures, Pineridge Press, Swansea, 1990, 1319-1336.

Miguel, P. F., Jawad, M. A., Fernandez, M. A., "A discrete-Crack Model for the Analysis of Concrete Structures", Proceedings of the Second International Conference on Computer Aided Analysis and Design of Concrete Structures, Pineridge Press, Swansea, 1990, 847-908.

Minor, J., Jirsa, J., "Behavior of Bent Bar Anchoragees", ACI Structural Journal, April 1975.

Ngo, D, Scordelis, A. C, "Finite Element Analysis of Reinforced Concrete Beams", ACI Journal, PP. 152-163, March 1967.

Nilson, A. H,"Internal Measurement of Bond Slip", ACI Journal, July 1972.

Nilson, A. H,"Nonlinear Analysis of Reinforced Concrete by the Finite Element

Method", ACI Journal, September 1968.

Schmidt-Thrö, G., Stökl, S. and Kupfer, H., 'Verankerung der Bewehrung am Endauflager bei Einachsiger Querpressung' (Anchorage of Reinforcement at an End Bearing with Uniaxial Lateral Pressure'), (Lehrstuhl für Massivbau, Institut für Baiungenieurwesen III, Technische Universität, München, Mai 1986).

Tepfers, R, "Cracking of Concrete Cover Along Anchored Deformed Reinforcing Bars", Magazine of Concrete Research, Vol.31, No.106, PP.3-12, March 1979.

Untrauer, R. E, Henry, R. L,"Influence of Normal Pressure on Bond Strength", ACI Journal, September 1968.